Spectroscopy of Atmospheric Processes using a Terahertz Quantum Cascade Laser

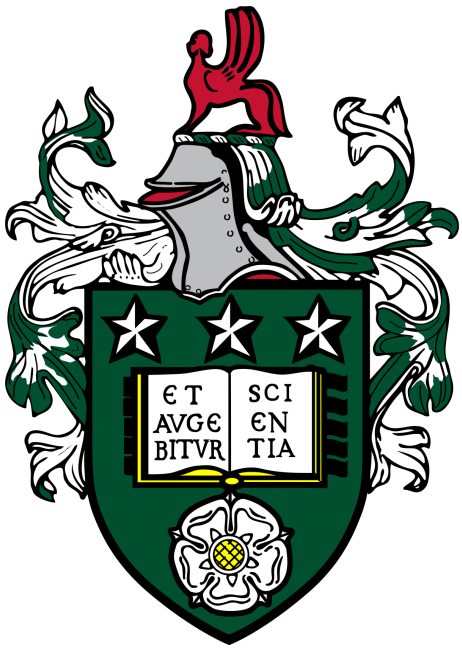

Eleanor Nuttall

Submitted in accordance with the requirements for the degree of
Doctor of Philosophy

University of Leeds
School of Electrical and Electronic Engineering
January 2023

Declaration

The candidate confirms that the work submitted is her own and that appropriate credit has been given where reference has been made to the work of others. This copy has been supplied on the understanding that it is copyright material and that no quotation from this work may be published without proper acknowledgement.

All quantum-cascade lasers (QCLs) described in Chapter 3 were designed and fabricated by Yinjun Han, with help from Lianhe Li and Mohammed Salih in the cleanroom. The QCLs were integrated into the metallic waveguide blocks by RAL Space.

The measurement in Figure 3.9, as well as the polarisation measurements presented in Section 3.2.6.2 were done with the supervision of Michael Horbury. The script used to calculate the leakage factor, isotropic power attenuation and ellipticity of the source was developed by Alex Valavanis.

In Chapter 4, the self-mixing (SM) set-up was built prior to the start date of this thesis by Alex Valavanis and Yingjun Han. The SM gas spectra were measured, in part, under the supervision of Yingjun Han. The work presented in Figure 4.16 was taken and analysed solely by Yingjun Han. The script used to output the transmission spectrums was a collaboration between myself and Li Xinyan.

In Chapter 5, the building of the Fourier Transform Infrared (FTIR) spectrometer, as well as recording the QCL emission spectra was done under the supervision of Michael Horbury.

To Niall and Zara. How lucky I am.

Acknowledgements

Firstly, I would like to thank my supervisor, Dr Alex Valavanis, not only for this opportunity, but also for the support and guidance you have given me along the way. You made the transition into a new discipline a whole lot easier. Similarly, thank you to my co-supervisors, Dr Julia Lehman and Dr Dan Stone. A (somewhat) multi-disciplinary PhD was a struggle at times. You both were a happy reminder of my chemistry roots.

A special thank you to Dr Andrew Burnett, who first introduced me into the weird and wonderful world of THz during my master's degree. Your enthusiasm inspired me to carry on with research, and I am not just speaking for myself when I say you are one of the kindest people to have graced the THz lab.

Thank you to Dr Yingjun Han, whose patience during the first few months into my PhD was award winning. Your calm nature made all those hiccups in the lab not feel so bad. To the rest of the THz atmospheric and space research group - Mitch, Nick, and Sanchit, thanks for all your help.

I will forever be grateful to Sue Hobson, my second mum! When things got tough you were always there checking in. My PhD experience was made all the more fun and brighter because of you and the rest of the friends I've made along the way - Rucha, Thomas, Rowan, Connor, Jac, Aniela, Calum, and Hanshuo, for that I thank you all.

Finally, thank you to my friends and family, who still don't know what I do, but nevertheless tried their best to act interested whenever I brought up my research. For sitting through the countless practices of conference presentations I subjected you to, I owe you a few pints.

Abstract

Results from the National Aeronautics and Space Administration (NASA), Cosmic Background Explorer, Diffuse Infrared Background Experiment [1], and examinations of the spectral energy distributions of galaxies [2] provides evidence that up to 98 % of photons emitted after the big bang are observable in the far-infrared (FIR)/Terahertz (THz) region [3]. As a result of this, there has been an increasing amount of interest in and research into the THz frequency range in the last few decades. This has lead to rapid development in manufacturing efficient and compact THz sources and detectors that can better help our understanding of the chemical workings of our galaxy.

Through laboratory measurements, we can not only obtain the spectrum of a molecule, but we can also look at the kinetics and different reaction pathways of a range of molecular and atomic species in a controlled way. We are able to mimic the conditions typically found in our atmosphere and from this, gather more realistic and detailed data for atmospheric models.

The aim of this project was to develop instrumentation for the purpose of gas sensing in the THz region, with a particular focus on it being used for atmospheric and climate change studies. This project involved designing and building a THz quantum cascade laser (QCL) gas spectroscopy system that can achieve high enough sensitivity to allow for trace gas detection with potential future satellite applications. This required multiple experimental systems to be developed as various different spectroscopic methods were tried and tested to optimise the system to the best of its ability. It is hoped that the research in this project will contribute to the successful progression towards the first portable compact sensitive spectrometer with a THz QCL.

In this thesis, the development of a THz gas spectrometer that utilised self-mixing (SM) interferometry and later on, Michelson interferometry is presented. Both systems employed a multimode block integrated THz QCL and were successful in measuring the QCL emission spectrum between 3–4 THz. In addition, the singular species D_2O and CH_3OH were measured, as well as the first mixture of gaseous

species with a THz QCL using SM interferometry.

Also presented in this work is the detailed characterisation of three QCLs, two at 3.4-THz and one at 4.7-THz. These QCLs were integrated into a copper block in order to improve the beam quality for atmospheric and space research purposes. The measurements in this thesis provided a thorough insight into the operating conditions and beam pattern of the QCLs, and generated key findings that will aid in future developments in employing this integration technique.

Publications

The work in this thesis has been presented in the following journal paper and conference proceedings:

Peer-reviewed journal papers

• **E. Nuttall**, Y. Han, D. Pardo, S.S. Kondawar, N. Brewster, M. Salih, L.H. Li, M.D. Horbury, A.G. Davies, E.H. Linfield, H. Wang, P. Dean, B.N. Ellison and A. Valavanis. 'Waveguide integration of a >4.7-THz quantum-cascade laser,' in *Electronic Letters*, vol.59, no.2, p.12703, 2023.

Conference Proceedings

• A. Valavanis, Y. Han, **E. Nuttall**, E. Zafar, D. Pardo, O. Auriacombe, T. Rawlings, N. Daghestani, E.H. Linfield, A.G. Davies, 'Development of Terahertz Quantum-Cascade Lasers for Satellite-Borne Measurement of Key Gas Species,' in *Conference on Lasers and Electro-Optics (CLEO)*, 2019.

• Y. Han, J. Partington, R. Chhantyal-Pun, **E. Nuttall**, M. Henry, O. Auriacombe, T. Rawlings, L.H. Li, J. Keeley, M. Oldfield, N. Brewster, R. Dong, A.G. Davies, B.N. Ellison, E.H. Linfield, A. Valavanis, 'Broadband terahertz gas spectroscopy through multimode self-mixing in a quantum cascade laser,' in *SPIE Optical Engineering + Applications: Terahertz Emitters, Receivers, and Applications*, 2019.

• **E. Nuttall**, Y. Han, M.D. Horbury, N. Brewster, M. Oldfield, L.H. Li, A.G. Davies, E.H. Linfield, B.N. Ellison, P. Dean, D. Stone, J.H. Lehman, A. Valavanis, 'Spectral analysis of a gas-phase reaction using self-mixing in a terahertz quantum cascade laser,' in *45th International Conference on Infrared, Millimeter and Terahertz Waves (IRMMW-THz)*, 2020.

• **E. Nuttall**, Y.J. Han, D. Pardo, M.D. Horbury, S.S. Kondawar, N.K. North, I. Kundu, O. Auriacombe, T. Rawlings, N. Brewster, M. Oldfield, M. Salih, L.H. Li,

E. Zafar, A.G. Davies, E.H. Linfield, E. Saenz, H. Wang, B.N. Ellison, A. Valavanis, 'Waveguide integrated terahertz quantum-cascade laser systems,' in *46th International Conference on Infrared, Millimeter and Terahertz Waves (IRMMW-THz)*, 2021.

• A. Dunn, Z. Zhang, M.D. Horbury, **E. Nuttall**, Y. Han, M. Salih, L.H. Li, E. Saleh, R. Harris, N. Daghestani, D. Pardo, B. Ellison, A. Burnett, H. Gleeson, A. Valavanis, 'Development of Advanced Terahertz Optics Using Liquid Crystals,' in *46th International Conference on Infrared, Millimeter and Terahertz Waves (IRMMW-THz)*, 2021.

• A. Dunn, Z. Zhang, M.D. Horbury, **E. Nuttall**, Y. Han, M. Salih, L.H. Li, A. Bond, E. Saleh, R. Harris, N. Daghestani, D. Pardo, B. Ellison, A. Burnett, H. Gleeson, A. Valavanis, 'Liquid-Crystal-Based Optics for use at THz-QCL Frequencies,' in *9th International Optical Terahertz Science and Technology*, 2022.

• A. Dunn, Z. Zhang, M.D. Horbury, **E. Nuttall**, Y. Han, M. Salih, L.H. Li, A. Bond, E. Saleh, R. Harris, N. Daghestani, D. Pardo, B. Ellison, A. Burnett, H. Gleeson, A. Valavanis, 'Extracting Material Properties from a Liquid Crystal Cell Using Terahertz Spectroscopy,' in *47th International Conference on Infrared, Millimeter and Terahertz Waves (IRMMW-THz)*, 2022.

List of Figures

1.1 The electromagnetic spectrum 4
1.2 An illustration of the Beer-Lambert law. 5
1.3 Multipass gas cell designs. 6
1.4 Beam pattern with spherical mirrors and astigmatic mirrors. 7
1.5 Schematic diagram of spin-orbit coupling. 9
1.6 THz images of a tumour. 11
1.7 THz absorption line for key gaseous species in the Earth's atmosphere. 12
1.8 Schematic illustration of the KEYSTONE satellite. 14

2.1 Schematic illustration of three different interactions between light and electrons. 16
2.2 Three-level laser system. 18
2.3 Four-level laser system. 19
2.4 Harmonics of a standing wave. 19
2.5 Quantum cascade laser. 23
2.6 Active region designs of a quantum cascade laser. 25
2.7 Schematic diagram of a single metal and double metal waveguide. . . 26
2.8 Schematic illustration of a heterodyne spectroscopic system. 28

3.1 Unmounted THz QCL. 31
3.2 Images of the internal structure of a metallic waveguide. 31
3.3 Front and back facet of a block integrated QCL. 32
3.4 Block integrated QCL mounted onto a Janis cryostat. 33
3.5 Schematic diagram of the experimental setup used for QCL characterisation. 34
3.6 Image of a QCL active region with an enlarged microscope picture of the QCL layers. 35

3.7 LIV curves of the unmounted 3.4 THz QCL in continuous-wave (CW) at various temperatures. 35
3.8 LIV curves of Device A in pulsed mode at various temperatures. . . . 36
3.9 FTIR spectrum of Device A at various currents. Measured at a QCL temperature of 10 K. 37
3.10 Frequency of the three main emission modes of Device A as a function of current. 38
3.11 LIV curves of Device B in CW mode at various temperatures. 39
3.12 LIV curves of Device B in pulsed mode at various temperatures. . . . 40
3.13 FTIR spectrum of Device B at various currents. Measured at 10 K. . 41
3.14 Frequency of the three main emission modes of Device B as a function of current. 42
3.15 light intensity-current-voltage (LIV) curves of the 4.7 THz QCL in pulsed mode at various temperatures. 43
3.16 FTIR spectrum of the 4.7 THz QCL at various currents. Measured at a QCL temperature of 10 K. 44
3.17 Frequency of the four main emission modes of the 4.7 THz QCL as a function of current. 45
3.18 Output power of the 4.7 THz QCL as a function of duty cycle. 46
3.19 Peak power of the 4.7 THz QCL recorded in pulsed mode as a function of heat-sink temperature. 46
3.20 Internal temperature of the 4.7 THz QCL as a function of duty cycle. 47
3.21 Output power from the 4.7 THz QCL transmitted through a polarizer. Red line shows a non-linear fit to the data. 49
3.22 Beam profile of Device A at 180 mA at a distance of 40 mm, 50 mm and 75 mm away from the QCL. 53
3.23 Cross-section of the horizontal and vertical intensities of Device A at 50 mm and 75 mm away from the QCL. 54
3.24 Beam profile of Device A at various currents at a distance of 70 mm away from the QCL. Measured at 10 K. 56
3.25 Calculated frequency profiles of the 3.29 THz, 3.36 THz and 3.42 THz modes of Device A. 57
3.26 Beam Profiles of Device A at 120 mA and 140 mA. 58
3.27 Beam profiles of Device B at 360 mA at a distance of 50 mm, 75 mm and 100 mm away from the QCL. 59
3.28 Cross-section of the horizontal and vertical intensities of Device B at 75 mm and 100 mm away from the QCL. 60

3.29 Derivative plots of knife-edge measurements of far-field beam profiles of integrated 4.7 THz QCL, for the front facet (a,b) and back facet (c,d) in the perpendicular plane (left) and parallel plane (right) of the waveguide block. 61

4.1 Schematic diagram of the self-mixing effect. 63
4.2 Calculated waveforms of V_{SM} for different values of the feedback parameter, C. 66
4.3 High resolution images taken using THz QCL self-mixing (SM) interferometry. 67
4.4 Schematic diagram of the experimental SM setup. 69
4.5 Interferogram recorded using the 3.4 THz QCL (Device A). 70
4.6 Example Fast Fourier Transform (FFT) calculated from the interferogram given in Figure 4.5 using the 3.4 THz QCL (Device A) at 140 mA. 71
4.7 Example of a frequency vs current plot for a reference and sample. . . 73
4.8 FFT spectra of a reference and sample (D_2O), highlighting the uncertain data points recorded during the SM experiments. 74
4.9 Frequency vs current plot for CH_3OH at 3 Torr at a frequency of 3.36 THz. 76
4.10 Transmission spectrum of CH_3OH at 3 Torr including all data points at 3.36 THz. 77
4.11 Transmission spectrum of CH_3OH at 3 Torr excluding the uncertain data points at 3.36 THz.. 79
4.12 Reference FFT spectrum taken at 110 mA. 79
4.13 Frequency vs current plot for CH_3OH at 3 Torr at a frequency of 3.42 THz. 80
4.14 Transmission spectrum of CH_3OH at 3 Torr including all data points at 3.42 THz. 81
4.15 Transmission spectrum of CH_3OH at 3 Torr excluding uncertain data points at 3.42 THz. 81
4.16 Transmission spectrum of CH_3OH at 5 Torr. 82
4.17 Frequency vs current plot of reference and pure D_2O at various pressures. 83
4.18 Reference FFT spectrum taken at 200 mA. The 3.42 THz mode is not present. 84
4.19 Transmission spectra of pure D_2O at various pressures including all data points. 86

4.20 Transmission spectra of pure D_2O at various pressures excluding uncertain data points. 87
4.21 Peak area of the 3.3603 THz D_2O gas line as a function of pressure. . 88
4.22 Frequency vs current plot of reference and a D_2O/HDO mixture at 1 Torr. 89
4.23 Transmission spectrum of a D_2O and HDO mixture at 1 Torr including all data points. 90
4.24 Transmission spectrum of a D_2O and HDO mixture at 1 Torr. 90
4.25 Transmission spectrum of a D_2O and HDO mixture at 1 Torr and a QCL temperature of 10 K. Includes all data points from 141 mA to 240 mA. 91
4.26 Transmission spectrum of a D_2O and HDO mixture at 1 Torr excluding the data points where negative transmission has occurred from 141 mA to 240 mA. 92

5.1 Schematic diagram of a Michelson interferometer. 95
5.2 Schematic diagram of the FTIR spectrometer used in this project. . . 96
5.3 QCL emission spectrum recorded at 140 mA with the position triggered from the XPS controller. 97
5.4 QCL emission spectrum recorded at 240 mA with the position triggered from the Data Acquisition (DAQ) board. 98
5.5 QCL emission spectrum recorded at 200 mA with the position triggered from a HeNe laser. 99
5.6 QCL emission spectra recorded at 140 mA over ten minutes. 100
5.7 Comparison of the QCL emission spectrum recorded using a FTIR spectrometer and a SM system at 125 mA. 101
5.8 Reference and sample FFT spectrums taken at various currents using the FTIR spectrometer. 103
5.9 Repeated measurements of reference and sample FFTs at various currents using the FTIR spectrometer. 104
5.10 Output power of the QCL recorded over 75 minutes. 105
5.11 Power fluctuations of the 3.34 THz and 3.36 THz mode of Device A over 100 minutes. 106
5.12 QCL emission spectra recorded at 170 mA at a QCL temperature of 10 K. Each spectrum was measured within a minute of each other. After scan 7, a mode hop occurs. 107
5.13 Output power of the active modes of the QCL pre and post-mode hop. 108
5.14 Measurement of the ambient noise in the laboratory with the air-conditioning unit turned on and off. 109

List of Tables

1.1 THz lines of elemental atoms and ions fine structure transitions. . . . 13

List of Abbreviations

Acronyms

BTC bound-to-continuum

BWO backward wave oscillator

CSL chirped superlattice

CW continuous-wave

DAQ Data Acquisition

DM double-metal

EM electromagnetic

EO electro-optic

FFT Fast Fourier Transform

FIR far-infrared

FSR free spectral range

FTIR Fourier Transform Infrared

FWHM Full-Width at Half-Maximum

GC gas chromatography

GCMS gas chromatography and mass spectrometry

GREAT German REceiver for Astronomy at Terahertz frequencies

GUSTO Galactic/Extra-Galactic Spectroscopic Terahertz Observatory

HEB hot electron bolometer

IF intermediate frequency

IR Infrared

ISM interstellar medium

JPL Jet Propulsion Laboratory

LEF linewidth-enhancement factor

LIF laser-induced fluorescence

LIV light intensity-current-voltage

LO longitudinal optic

LO local oscillator

MBE molecular beam epitaxy

MLS Microwave Limb Sounder

MLT mesosphere lower thermosphere

MS mass spectrometer

NASA National Aeronautics and Space Administration

NMR nuclear magnetic resonance

OAS optical absorption spectroscopy

OF optical feedback

OPD optical path difference

PC photoconductive

PCA photoconductive antenna

PM particulate matter

ppb parts-per-billion

ppm parts-per-million

ppt parts-per-trillion

QCL quantum-cascade laser

QW quantum well

RP resonant phonon

RTD resonant tunneling diode

SI-SP semi-insulating surface plasmon

SM self-mixing

SMA subminiature-A

SNR signal-to-noise ratio

SOFIA Stratospheric Observatory for Infrared Astronomy

STO Stratospheric Terahertz Observatory

TEM transverse electromagnetic

THz Terahertz

ULDB Ultra Long Duration Balloon

UV Ultraviolet

VOC volatile organic compound

Contents

1 Introduction **1**

1.1 Spectroscopy . . . 2

1.1.1 Analytical Chemistry Methods . . . 2

1.2 Absorption Spectroscopy . . . 4

1.2.1 Beer-Lambert Law . . . 5

1.2.2 Cavity-Enhanced Techniques . . . 5

1.2.3 Selection Rules . . . 7

1.3 THz Radiation . . . 9

1.3.1 THz Applications . . . 10

1.4 THz Atmospheric and Space Chemistry . . . 11

1.5 Project aims and thesis structure . . . 14

2 THz Spectroscopy Instrumentation **16**

2.1 Laser Theory . . . 16

2.2 Active THz Sources . . . 20

2.3 THz detection methods . . . 21

2.4 Quantum cascade laser . . . 22

2.4.1 Active region designs . . . 24

2.4.2 Waveguides . . . 25

2.4.3 QCL Performance . . . 27

2.5 Active and Passive Sensing . . . 27

3 THz quantum cascade lasers for gas-phase spectroscopy **29**

3.1 QCL integration . . . 30

3.2 QCL characterisation . . . 32

3.2.1 3.4 THz QCL fabrication . . . 34

3.2.2 Unmounted 3.4 THz QCL characterisation . . . 35

3.2.3 Device A characterisation . . . 36

3.2.4 Device B characterisation . . . 39

3.2.5 4.7-THz QCL fabrication . . . 42

3.2.6 4.7-THz QCL characterisation . . . 43

3.3 Beam Profiling . . . 52

3.3.1 Beam profile of device A . . . 52
3.3.2 Beam profile of Device B . . . 58
3.3.3 Beam profile of 4.7-THz QCL . . . 60
3.4 Conclusion . . . 62

4 Self-mixing interferometry 63
4.1 Self-mixing . . . 63
4.1.1 THz QCL SM applications . . . 67
4.2 Experimental set-up . . . 68
4.3 CH_3OH . . . 76
4.4 D_2O . . . 82
4.4.1 D_2O 1 Torr reaction . . . 88
4.5 Conclusion . . . 92

5 THz FTIR spectroscopy 94
5.1 FTIR spectroscopy . . . 94
5.1.1 Experimental set-up . . . 96
5.2 Sampling methods . . . 97
5.3 Repeatability scans . . . 99
5.4 Preliminary gas measurements . . . 100
5.5 Device A Power measurements . . . 104
5.5.1 Device B Power measurements . . . 106
5.6 Conclusion . . . 109

6 Conclusion and further work 110
6.1 Further Work . . . 111

Chapter 1

Introduction

Perhaps one of the greatest challenges for scientists in the 21st century is to understand the Earth's complex weather and climate system and its response to the unprecedented rise in man-made pollutants and greenhouse gases. Since the pre-industrial era (before 1750), the concentrations of key greenhouse gases: carbon dioxide (CO_2), methane (CH_4), and nitrous oxide (N_2O) have significantly increased by 148 %, 259 % and 123 % respectively [4, 5].

The physical, societal and economic implications that could occur from this rise are much larger than initially thought [5]. Our current knowledge of the numerous feedbacks and linkages between physical (e.g. droughts, wildfires, rising sea-levels, and space weather fluctuations) and chemical atmospheric processes is inadequate, and therefore makes it difficult to quantitatively predict the effect on our climate. Coupled with the variability of the chemical composition of our atmosphere on timescales from diurnal to decadal, high-quality laboratory studies, field observations and theoretical modelling are all necessary for better understanding, forecasting and prevention. More specifically, further research is required on the 'missing links' in our knowledge on lifetimes and reaction pathways of pollutants and their precursors. What are the concentration profiles of these species? How do they change within the different layers of our atmosphere? and how do they contribute to feedback processes? The development of sensitive instrumentation is crucial in order to help answer these questions. The research in this project looks at characterising a THz source and utilising it for spectroscopy to demonstrate their suitability/capabilities for Earth and space research.

1.1 Spectroscopy

The history of spectroscopy can be traced back to 1666, when Sir Isaac Newton used a glass prism to split white light into several separate colours, – a spectrum [6]. Over a century later in 1802, William Wollaston studied the same continuous spectrum from sunlight, and observed a series of irregular dark lines [7]. Joseph Fraunhofer in 1817 conducted further studies into these dark lines. He connected a telescope to the slit and prism to better view the spectrum, and consequently developed the first spectroscope. Using this spectroscope, Fraunhofer was able to measure over 500 dark lines in the solar spectrum [8]. However, the origin of these lines still remained a mystery. Soon after, Sir John Herschel used a spectroscope to analyse coloured flames to determine their elemental origin [9], and in doing so laid the foundation for chemical analysis using spectroscopy. In order to better explain the dark lines that were being observed, Gustav Kirchhoff proposed the theory of absorption and emission lines. He stated that for a substance to absorb light at a specific wavelength, it must also be able to emit light at that same wavelength [10]. Taking the many observations made of spectra, and ideas of quantum theory developed by Max Planck, in 1913 Niels Bohr proposed the theory that electrons must exist in specific energy states. For an electron to transition to a different energy state, the electron must absorb or emit light that has an energy equal to the energy difference between the two states. It is these transitions that can account for the observed spectral lines [11]. Since then, remarkable developments in instrumentation and theories in the field of spectroscopy have been made, advancing our understanding of atomic and molecular behaviour at various wavelengths.

1.1.1 Analytical Chemistry Methods

The instrumentation available for chemical analysis is vast; the examples below serve to demonstrate just some of the techniques that can be used and the principles behind them. The work primarily concerned in this project was to build a spectrometer to work *in situ*, be non-destructive and to have scope to work remotely i.e. is portable. However, a wide range of other techniques exist that in their own capacity are excellent analytical tools.

Identifying biogenic and anthropogenic species in our atmosphere is important to help with accurate predictions in climate and weather modelling. In some areas of atmospheric chemistry such as aerosol chemistry, this identification becomes challenging, since these short- and long-lived species are bound to other particles. To use a technique such as absorption spectroscopy (see Section 1.2) on a multi-component mixture would evidently lead to a very crowded spectrum, making identification

extremely difficult. Instead, chromatography techniques can be used, which first separate the mixture before identification. One of the most popular and well established chromatographic methods is gas chromatography (GC). In GC a multi-component mixture in a mobile phase (a carrier gas) travels through a stationary phase (usually alumina or silica). Separation occurs due to the interaction of the components in the mixture with the stationary phase, with each component having its own retention time depending on how long it takes for it to travel over the stationary phase. For example, a short retention time would mean the component did not interact strongly with the stationary phase. The sample can then be passed into a mass spectrometer (MS), where it is ionised and each component is identified based on their mass-to-charge ratio (m/z). Combined, gas chromatography and mass spectrometry (GCMS) offers high selectivity and sensitivity, with detection limits approaching 0.01 parts-per-trillion (ppt). Unfortunately, its uses are restricted. The sample is destroyed during the experiment, and owing to the bulkiness and complexity of the instrumentation, maintenance is complicated and GCMS cannot be used remotely [12].

The invention of the laser in 1960 by Theodore Maiman [13] revolutionised the way we use spectroscopy and offered numerous solutions in terms of non-destructive testing, rapid response and environmentally friendly analysis. One such technique that offers non-destructive testing is laser-induced fluorescence (LIF) spectroscopy. LIF is based on the electronic excitation of an atom or molecule by laser irradiation. When the electron relaxes back down to the lower energy level, a photon is released via fluorescence. LIF is highly sensitive, however in general, many larger molecules are susceptible to 'non-radiative' transitions i.e. dissociation or quenching rather than fluorescence [14]. An alternate non-destructive technique is nuclear magnetic resonance (NMR) spectroscopy. NMR spectroscopy is a widely used technique by chemists since it gives information on specific nuclei, chemical bonding and local electronic structure. A sample is placed in a magnetic field and exposed to radio waves. Selected nuclei within the sample (most commonly ^{2}H or ^{13}C) begin to resonate at a specific frequency which is then detected. NMR spectroscopy is a very powerful technique, often offering complete chemical analysis, and coupled with Infrared (IR) spectroscopy the structure of unknown molecules can usually be deduced. Although being a non-destructive technique, NMR is notably insensitive, requiring a much larger sample size than GCMS. In addition, NMR has limited field applications [15] and therefore its use is minimal in atmospheric and space research.

Optical absorption spectroscopy (OAS) fulfils the requirement of a spectroscopic technique that works *in situ*, is non-destructive and has remote testing capabilities. It offers fast response with high gas selectivity and sensitivity ranging from parts-

per-million (ppm) to ppt depending on the gaseous species and detection method. As such, OAS is one of the most widely used spectroscopic techniques in atmospheric chemistry research, and encompasses various methods that can be used to measure the kinetics, spectral parameters and composition. In this project, the development of instrumentation was based on the principles of OAS. Given below is a more detailed introduction to OAS, including techniques used at particular wavelengths as well as the specific rules that govern each part of the electromagnetic (EM) spectrum.

1.2 Absorption Spectroscopy

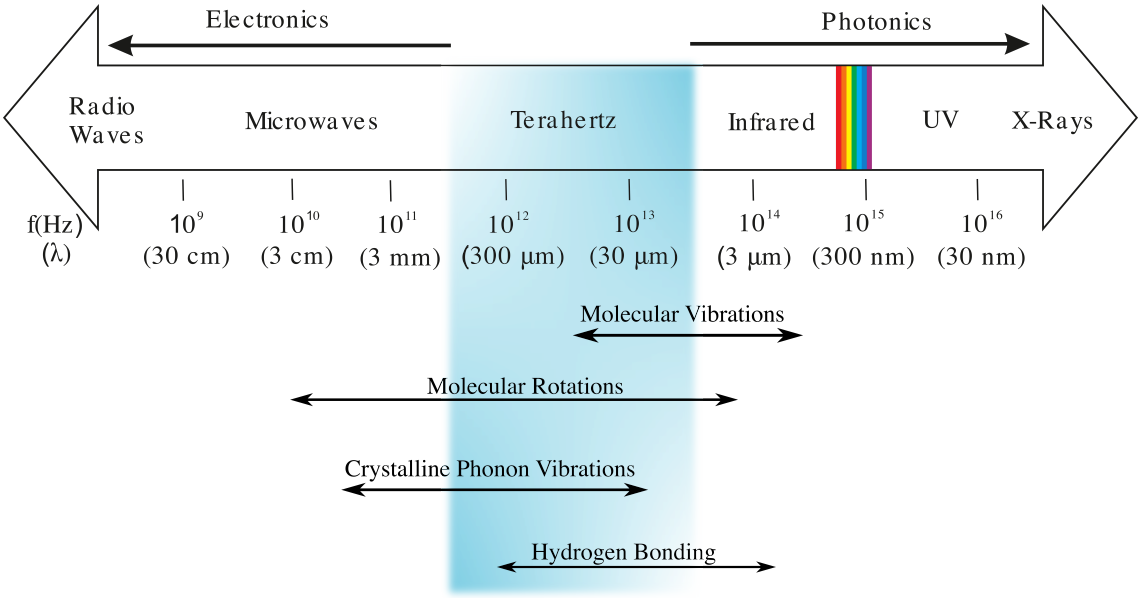

Figure 1.1: The EM spectrum. The THz region is highlighted in blue including interactions that occur at this frequency. Figure adapted from [16].

The spectral lines in molecular spectroscopy arise from the absorption, emission, or scattering (Raman) of light due to a change in energy that occurs from an electronic, vibrational or rotational transition. Which transition occurs depends on the particular wavelength of light being used. The same applies to atomic spectroscopy, however in this case only electronic transitions can occur. Figure 1.1 is an illustration of the EM spectrum, showing the different regions and their corresponding wavelength and frequency. Within the THz frequency range (the region of the EM spectrum that this project is focused on), resides fundamental rotational transitions of molecules, as well as vibrational transitions of larger molecules, and fine-line electronic structure transitions (see Sections 1.2.3.1 and 1.4) of atoms and ions.

1.2.1 Beer-Lambert Law

The absorption of radiation for N attenuating species is described by the Beer-Lambert law,

$$A_{(\nu)} = \ln\left(\frac{I_{0(\nu)}}{I_{(\nu)}}\right) = \sum_{i}^{N} \sigma_i c_i l \tag{1.1}$$

where $A_{(\nu)}$ is absorbance as a function of light frequency ν, $I_{0(\nu)}$ is the initial intensity of light and $I_{(\nu)}$ is the intensity of light after passing through a sample. σ_i is the absorption cross section of the attenuating species i in the sample, c_i is the concentration of the attenuating species i in the sample and l is the path length.

As light passes through a sample cell, it is absorbed by the sample. Absorbance is directly proportional to the concentration of the sample. Therefore, the larger the concentration, the stronger the absorbance, resulting in a decrease in the intensity of the light (shown in Figure 1.2).

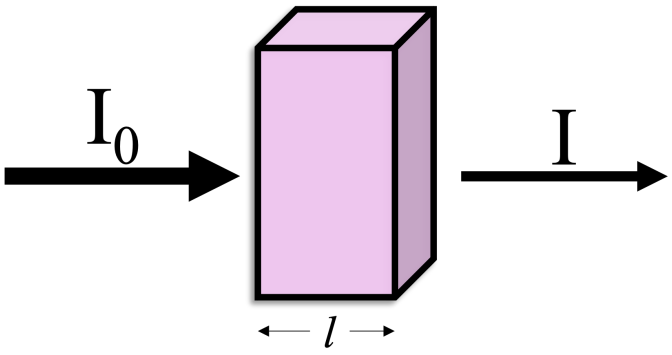

Figure 1.2: An illustration of the Beer-Lambert law.

1.2.2 Cavity-Enhanced Techniques

The detection limit of a system can be improved through the selection of a spectral range with the strongest absorption cross section. Quite often though, the choice is made based on the region of the spectra where the gas being investigated exhibits not only a strong absorption line, but is also free from interference from other gases.

In situ absorption measurements often require enhanced path lengths to measure the low concentration of many gases that appear in our atmosphere. Following the rules set out by the Beer-Lambert law (equation 1.1), adopting a multipass gas cell over a single pass will increase the achievable sensitivity of a spectroscopic system as there are more instances for the light to interact with the gaseous species. It has

been demonstrated in the mid-IR that employing a multipass gas cell can increase your sensitivity from ppm to parts-per-billion (ppb) [17–19].

Commonly used in laboratory studies, where the only feasible option to enhance the path length is to fold the optical path on itself, multipass cells are made up of highly reflective (>99.5 %) concave mirrors. First proposed by White et al. [20], the White cell (Figure 1.3a) is composed of three concave mirrors. The laser beam is focused and defocused repeatedly between the mirrors, and because of this periodic focusing, the diffraction loss is much smaller than that which can occur with an open beam. Herriott et al. [21] offered an alternate simplified multipass cell design that requires only two concave mirrors (Figure 1.3b); However, the basic principles are still the same and by changing the mirror separation, the beam pattern changes, leading to an increase or decrease in path length.

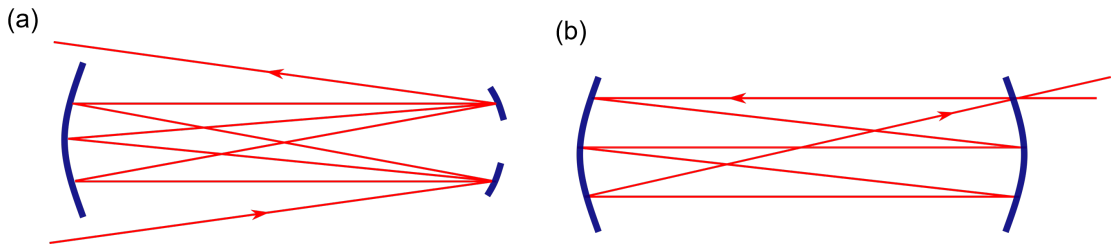

Figure 1.3: Multipass gas cell designs of (a) a White cell, and (b) a Herriott cell.

Whilst the White cell is more complex with the additional mirror, it means a larger beam aperture can be accommodated without the need for larger optics. The Herriott cell is simpler. However, most of the mirror is left unused, since the majority of reflections occur around the same circumference (see Figure 1.4a). Using astigmatic mirrors, i.e. each mirror having a different radius of curvature, is one solution. These mirrors create a Lissajous beam pattern, with the beam using more of the mirror's area (see Figure 1.4b). This ultimately leads to more passes than with the conventional Herriott cell and a longer path length can be achieved [22].

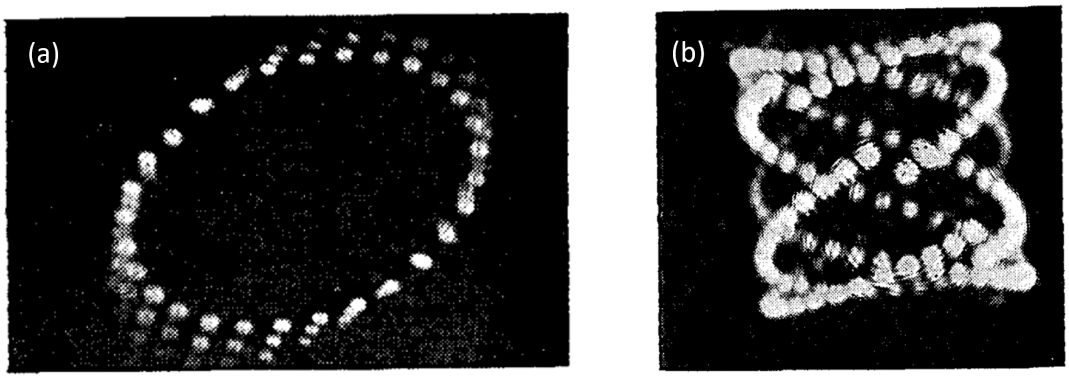

Figure 1.4: Beam pattern with (a) spherical mirrors and (b) astigmatic mirrors. Figures taken from reference [22].

1.2.3 Selection Rules

In spectroscopy, assuming a harmonic approximation, transitions are classified as either 'allowed' or 'forbidden' (highly unlikely), depending on a set of selection rules. Although many 'forbidden', transitions are allowed within the anharmonic approximation, but tend to be of a weaker intensity than allowed transitions.

Selection rules play a crucial role in determining if a transition is allowed or forbidden, and consist of gross selection rules and specific selection rules. Gross selection rules specify the general features that the molecule must have to exhibit spectral lines at a particular wavelength, whereas specific selection rules determine whether a transition is allowed through the change in quantum numbers. Note that the selection rules for absorption and emission spectroscopy differ from those for Raman (scattering) spectroscopy. In this work OAS is employed and so mention of selection rules below applies to absorption or emission spectroscopy only. By understanding the different selection rules, as well as the influence of energy level population, a better understanding of spectral lines and the properties of atoms/molecules can be obtained.

The energy associated with transitions between rotational energy levels lies within the microwave and THz region. The gross selection rule for rotational spectroscopy states that the molecular species must have a permanent electric dipole moment, that is a charge imbalance across the molecule, arising from one atom being more electronegative than the other(s). The specific selection rules for rotational spectroscopy are $\mathbf{\Delta J} = \pm\mathbf{1}, \mathbf{\Delta M}_j = \mathbf{0}, \pm\mathbf{1}$ and for symmetric rotors $\mathbf{\Delta K} = \mathbf{0}$ is required. Where $\mathbf{J}$ is the total angular momentum quantum number (dependent on the rotational and orbital angular momentum), $\mathbf{M}_j$ is the angular momentum around an externally defined axis and $\mathbf{K}$ is the angular momentum around the principal axis.

Absorption of IR radiation is restricted to molecules that have a vibration that distorts the charge distribution in such a way that there is a change in the electric dipole i.e. a stretching motion of a homonuclear molecule does not cause a change in the electric dipole moment and therefore the vibration is IR inactive. The specific selection rules for vibrational spectroscopy for anharmonic potential is $\mathbf{\Delta}\nu = \pm\mathbf{1}, \pm\mathbf{2}, ...$, where ν is the vibrational energy level. The $\nu = \mathbf{0} \leftrightarrow \nu = \mathbf{1}$ transition is the fundamental transition, where as transitions from a larger $\mathbf{\Delta}\nu$ i.e. $\nu = \mathbf{0} \leftrightarrow \nu = \mathbf{2}$ are overtone transitions. Its important to note that fundamental transitions don't always exhibit the largest spectral intensity. The intensity is instead proportional to the population of the initial energy level, as described by the Boltzmann distribution. Transitions from more populated energy levels can exhibit a larger spectral intensity than transitions from less populated energy levels, even if there is a higher energy change. In addition, spectral intensity is also proportional to the square of the transition electric dipole moment, which in turn depends on the degree of distortion that occurs.

Electronic transitions occur in the Ultraviolet (UV) and visible region of the EM spectrum (there are exceptions to this rule i.e. fine-line structure transitions, which are discussed in Section 1.2.3.1), and can provide us with information on the electronic structure of molecules e.g. bonding. The specific selection rules for electronic spectroscopy are $\mathbf{\Delta S} = \mathbf{0}$, $\mathbf{\Delta L} = \mathbf{0}, \pm\mathbf{1}$ and $\mathbf{\Delta J} = \mathbf{0}, \pm\mathbf{1}$, where $\mathbf{S}$ is the spin quantum number, $\mathbf{L}$ is the angular momentum quantum number and $\mathbf{J}$ depends on the rotational,orbital and electron spin angular momentum. For atoms, only electronic transitions occur, and so an atomic electronic spectrum exhibits sharp and clear spectral lines. A molecular electronic spectrum is very different. Molecules may also undergo rotations and vibrations alongside electronic transitions. As a result, spectral lines appear as one continuous absorption band centering around the strongest transition.

1.2.3.1 Fine-structure Transitions

Fine-structure transitions of atoms and ions are 'forbidden' electronic transitions, meaning there is no change in the electronic configuration, and instead radiate through magnetic dipole transitions rather than electric dipole transitions. These transitions occur through the interaction between $\mathbf{S}$ and $\mathbf{L}$ that form $\mathbf{J}$ i.e. $\mathbf{J} = |\mathbf{L} + \mathbf{S}|, |\mathbf{L} - \mathbf{S}|, |\mathbf{L} + \mathbf{S} - 1|$. This is commonly known as spin-orbit coupling (shown in Figure 1.5), and is responsible for the splitting of subshells further into separate energy states.

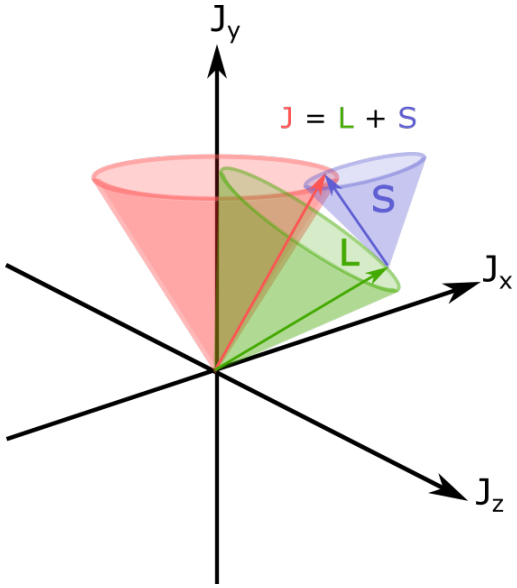

Figure 1.5: Schematic diagram of spin-orbit coupling. Where J is the total angular momentum (red), L is the total orbital angular momentum (green) and S is the total spin angular momentum (blue).

1.3 THz Radiation

Situated between microwave and IR of the EM spectrum (Figure 1.1), THz has scope to measure rotational, vibrational, and fine-line structure transitions, with potential to serve as a powerful technique in the field of atmospheric chemistry. Spanning from 0.1–10 THz, historically, measurements in this region (Frequency $(f) = 0.1\text{–}10\,\text{THz}$, Wavenumber $(\tilde{\nu}) = 3\text{–}300\,\text{cm}^{-1}$, Energy $(E) = 1.2\text{–}41.3\,\text{meV}$, Wavelength $(\lambda) = 10^{-3}\text{–}10^{-4}\,\text{m}$), have been difficult to obtain owing to a lack of suitable instrumentation.

The THz region is at the upper and lower frequency limits of what is achievable using methods employed in the microwave and IR regions, respectively. Within the microwave region electronic devices are typically used, such as bipolar junction transistors, heterojunction bipolar transistors and transferred electron (Gunn) diodes. These electronic devices work on the principle that the time taken for the carriers (electrons) to move in the active region dictates the frequency of the device. At higher frequencies, shorter carrier transit times are required which is difficult to achieve for frequencies above a few hundred GHz.

In the IR region, optical sources such as inter-band diode lasers (principles discussed in Section 2.1), are unsuitable for the THz region owing to its smaller photon energy. Alternate approaches such as THz QCLs (see Section 2.4) are instead required to overcome this limitation. THz sources are discussed further in Section 2.2.

1.3.1 THz Applications

The last few decades have shown an increasing interest in the THz frequency range, which has led to the rapid development in manufacturing efficient and compact THz sources and detectors. Because of this development, there is now a greater emphasis on researching the potential applications of THz radiation. This Section discusses some of the applications that can benefit from the unique properties of THz radiation.

Weaker modes of vibration caused by intermolecular bonds like hydrogen bonds and van der Waals interactions reside in the THz region. THz spectroscopy can therefore yield valuable insight into the tertiary structures of proteins [23] and nucleic acids [24]. This is of particular importance in biochemistry and pharmaceutical research, where the conformation of a molecule determines its molecular properties i.e. solubility and melting point.

With the photon energy of a THz wave between 1.2–12.4 meV (below the ionisation threshold), THz radiation can be used to penetrate through many non-polar materials such as cardboard, plastics, and paper packaging relatively unhindered. By utilising these non-ionising and non-invasive properties, there has been extensive research into using THz for the identification of concealed illicit drugs and weapons [25] and has proven to be a useful alternative to X-rays for security body scanning [26]. In addition, THz is used in imaging the thickness and uniformity of layers of materials. For example, pharmaceutical tablets [27] and automotive paints [28].

Water is highly absorbing in the THz band. Meaning its achievable depth penetration ranges from several hundred micrometres in analysis of fresh biological tissues [29, 30] to tens of metres outdoors in wireless communication applications [31]. This attenuation property can be used to an advantage in the medical sector, where the H_2O content varies between malignant (cancerous) and benign (non-cancerous) tissues. Coupled with the non-ionising properties discussed above, the use of THz has huge promise in skin disease diagnostics, illustrated in Figure 1.6.

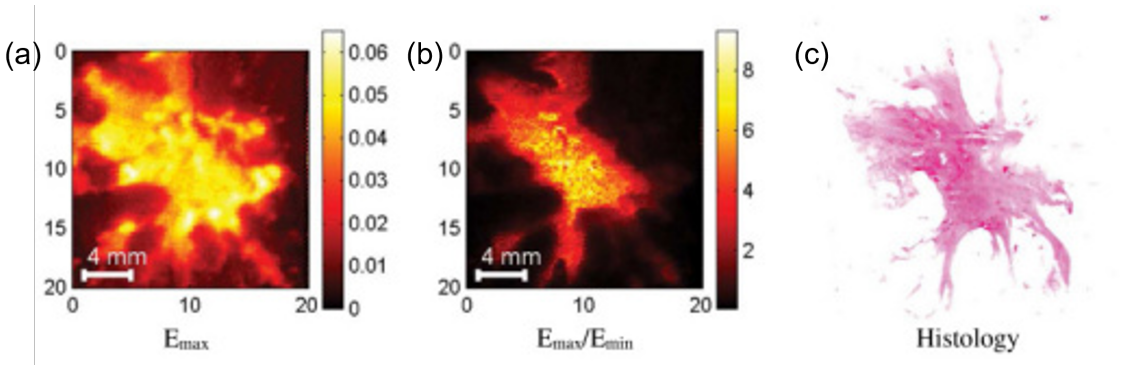

Figure 1.6: THz images of (a) tumour and the surrounding adipose tissue, (b) ratio of the maximum and minimum of the reflected THz pulse and (c) histology image of the tumour. Figure taken from reference [30].

To progress towards 6G in the increasingly demanding digital world would require an increase in data rates, which has ultimately led to research into utilising higher carrier frequencies, such as THz. Tapping into the THz frequency is one solution that would allow for up to several terabits-per second to be transmitted. As well as the increased data rates, utilising THz for wireless communications is a very attractive venture commercially, with a huge untapped bandwidth yet to be bought [32].

1.4 THz Atmospheric and Space Chemistry

The ability to detect a wide range of gas species underpins a number of applications within atmospheric and space research. The now heightened urgency, complexity and socio-economic implications of acting to reduce greenhouse gas emissions demands strategic investment in science-led information. THz spectroscopy is potentially a valuable technique that can be used to monitor trends and test the validity of atmospheric models. Alongside climate research, THz observations of atoms and molecules in the interstellar medium (ISM) can provide further insight into the origins of our galaxy. This Section serves to demonstrate the usefulness of THz radiation for these applications, with specific examples given of remote sensing measurements that have employed THz instrumentation.

The hydroxyl radical (OH), ammonia (NH_3) and ozone (O_3), all have spectral signatures that reside in the THz frequency range (see Figure 1.7). OH, for example, is a key oxidising intermediate, reacting and hence decreasing the concentration of carbon monoxide (CO), volatile organic compounds (VOCs) and methane (CH_4) that degrades air quality. However, at the same time, OH is also involved in the chemistry that leads to the formation of tropospheric O_3 and CO_2, highlighting the complexity of just one gaseous species reaction pathway. Agriculture is a major source of NH_3 emissions, that in turn lead to the formation of secondary particulate

matter (PM), a key contributor to ground-level smog [33, 34]. Mentioned here are just some of the molecules that have a pivotal role in controlling the climate, many others (see Figure 1.7) also give rise to spectral lines in the THz region with their own unique reaction pathways that need to be understood.

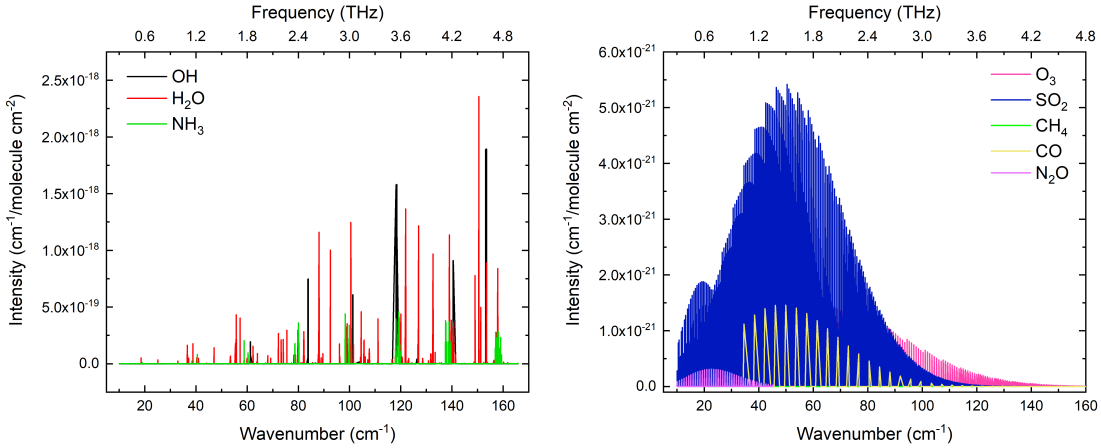

Figure 1.7: THz absorption lines for key gaseous species in the Earth's atmosphere, simulated using HITRAN [35].

Many elements that take part in astrophysical phenomena such as the evolution of galaxies, formation of interstellar clouds and the buildings blocks of life, amino acids, exhibit diagnostic and strongly luminous spectral lines within the THz region [36]. The typical size of interstellar dust grains ($\sim 0.1\,\mu$m) means they are effective at absorbing and scattering light which has a wavelength similar to its size e.g. short wavelengths seen in the UV, visible, and even near-IR range. Longer wavelengths with respect to the size of dust grains (∼100–1000 µm) like THz radiation generally pass unhindered, which allows for the deeper regions of interstellar dust clouds to be probed [37].

Oxygen (O), carbon (C) and nitrogen (N) are the most abundant elements in our universe after hydrogen (H) and helium (He), with the O, O^{++}, C, C^{+}, N^{+} and N^{++} fine-structure emission lines residing in the THz region. The frequency, transition and intensity of these emissions can be found in Table 1.1. Two of the brightest emission lines, the C^{+} and O line at 1.9 THz [38] and 4.7 THz [39] respectively, are cooling lines. Cooling lines arise from collisions between molecules. The thermal energy from the collision is converted into kinetic energy in the form of a rotation or vibration. The de-excitation of the molecule causes the energy to be released by the emission of a photon. The photon dissipates through the cloud of gas, cooling it. Interstellar dust clouds cool first before they collapse and form stars. Therefore, THz observations of these lines can aid in studies of the evolution of the ISM.

Gas Species	$\boldsymbol{\nu}$ (THz)	$\tilde{\boldsymbol{\nu}}$ (cm^{-1})	Transition	$\boldsymbol{S}$ (cm^{-1}/molecule cm^{-2})
O	2.06	68.71	$^3P_0$ - $^3P_1$	9.57×10^{-23}
	4.74	158.10	$^3P_1$ - $^3P_2$	1.11×10^{-21}
O^{++}	3.39	113.07	$^3P_1$ - $^3P_0$	
	5.78	192.80	$^3P_2$ - $^3P_1$	
C	0.49	16.34	$^3P_1 - {}^3P_0$	1.14×10^{-23}
	0.80	26.68	$^3P_2$ - $^3P_1$	3.47×10^{-23}
C^+	1.90	63.37	$^3P_{3/2}$ - $^3P_{1/2}$	1.62×10^{-22}
N^+	1.46	48.70	$^3P_1$ - $^3P_0$	7.25×10^{-23}
	2.45	81.72	$^3P_2$ - $^3P_1$	1.45×10^{-22}
N^{++}	5.23	174.45	$^2P_{3/2}$ - $^2P_{1/2}$	

Table 1.1: THz lines of elemental atoms and ions fine structure transitions. ν is the frequency, $\tilde{\nu}$ is the wavenumber and S is the spectral line intensity. Data taken from [40].

Briefly mentioned in the previous Section, H_2O is highly attenuating in the THz region which prevents ground-based observations unless at high, dry and cold sites [41, 42]. More often than not, THz observations are conducted in space using satellites, aircrafts or balloon-borne platforms. For example, following on from the success of the Stratospheric Terahertz Observatory (STO), the Ultra Long Duration Balloon (ULDB) Galactic/Extra-Galactic Spectroscopic Terahertz Observatory (GUSTO) mission intends to investigate the structure, formation, and life cycle of the ISM. On-board GUSTO will be three heterodyne receivers (principles discussed in Section 2.5) measuring the emission lines of N^+, C^+ and O at 1.4 THz, 1.9 THz and 4.7 THz respectively [43]. The German REceiver for Astronomy at Terahertz frequencies (GREAT) instrument on board the Stratospheric Observatory for Infrared Astronomy (SOFIA) has successfully detected the $^3P_1$ - $^3P_2$ transition of atomic O at 4.7 THz in the atmosphere of Mars. Whilst O can be measured with UV spectrometers, the various energy sources and chemical pathways that occur in space can often obscure a UV emission. By using a far-IR transition that is less susceptible to scattering and dust opacity, a more reliable measurement of O can be made [44].

Launched in 2004, the Microwave Limb Sounder (MLS) onboard of the National Aeronautics and Space Administration (NASA) Aura satellite is used to measure OH abundance and distribution at 2.5 THz. By using a satellite platform, data is collected on a global scale. Specifically, the Aura satellite follows a polar orbit, which allows for pole-to-pole coverage. The advantage of measuring at this frequency is that there are relatively few transitions from itself or other abundant molecules nearby, and therefore monitoring is made easier [45]. More recently, an Earth exploration mission named KEYSTONE has been proposed to observe the mesosphere

lower thermosphere (MLT) region of the Earth's atmosphere (see Figure 1.8). The MLT region lies at the interface between the lower atmosphere of Earth and the solar and space-weather from above. It is particularly sensitive to temperature and is cooling at an order of magnitude faster than model predictions. Observations in this region will be able to interpret the thermal fluctuations that are occurring, as well as give insight into the influence that the mixing of natural and anthropogenic species from each boundary layer has on the Earth's climate. Despite the obvious importance of these measurements, the MLT region is still poorly understood. The objective of KEYSTONE is to measure the concentration profiles of O directly, as well as O_2, NO, OH, CO and HO_2 at four spectral bands. Bands 1 (4.7 THz) and bands 2 (3.5 THz) employ a THz QCL to be used as a local oscillator (LO) source. Bands 3 (1.1 THz) and bands 4 (0.8 THz) utilise frequency multiplied electronic microwave sources as a LO source [46, 47]. The following chapter gives a more in-depth explanation of LOs and QCLs.

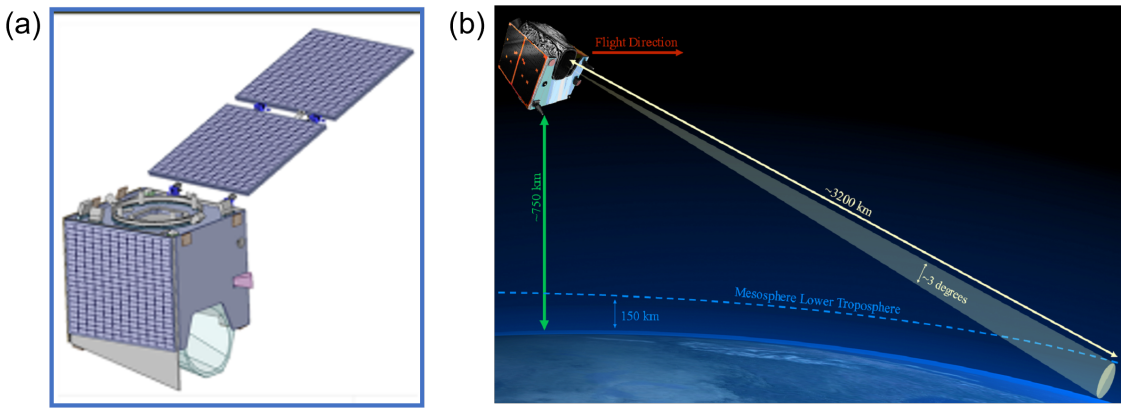

Figure 1.8: Schematic diagrams of the KEYSTONE mission (a) Structural design of the KEYSTONE satellite and (b) KEYSTONE scanning of the MLT region.

1.5 Project aims and thesis structure

Whilst QCLs are high-powered, compact and narrowband, they have yet to be fully realised as a source in a controlled laboratory gas spectroscopy system. THz radiation offers a number of advantages for spectroscopy compared to other radiative techniques. As outlined in Section 1.4, THz radiation experiences less scattering than IR and UV radiation owing to its longer wavelength, making it particularly beneficial for atmospheric and space research. Furthermore, as mentioned in section 1.3, THz primarily probes molecular rotations while IR spectroscopy focuses on vibrational modes associated with functional groups. This key difference often means that IR spectra, especially of large molecules or mixtures, can become convoluted when the measured species have similar functional groups. As such, THz in general

tends to exhibit a higher chemical selectivity for gas-phase measurements as opposed to IR [48].

The work in this project was to characterise THz QCLs to be used for spectral measurements, to develop a THz gas spectroscopy system, and to undertake preliminary measurements of gas species. The work in this project will hopefully lead to the successful fabrication of a high-powered, highly sensitive and compact THz gas spectroscopy system that has potential to be portable for field measurements. The structure of this thesis is as follows.

Chapter 2 provides a literature review of the key instrumentation used in this work, the THz QCL, including laser theory, active region designs, waveguides, and alternate THz sources.

The characterisation of the QCLs used in this project is given in chapter 3. Here, the fabrication, spectral characteristics as well as beam profiling analysis is presented.

The second experimental chapter in this thesis is given in chapter 4, where SM, the first of two spectroscopic methods used in this project is introduced. A detailed review of SM theory is presented. What follows is the experimental arrangement used and the gas spectroscopy measurements of gaseous species and mixtures.

The structure of chapter 5 follows similarly to that of chapter 4. Here, the FTIR spectroscopic method is explained including the experimental setup used. This is followed by the gas spectroscopy measurements performed with analysis. The advantages of using this set-up compared to the SM method discussed in chapter 4 provide and also contains a number of measurements and analysis that look at the power instability issues of THz QCLs.

Concluding remarks and potential future work are described in chapter 6.

Chapter 2

THz Spectroscopy Instrumentation

This chapter gives an overview of the key instrumentation that is currently being used for THz gas spectroscopy, including overall system configurations, THz sources and detectors. The chapter starts with an introduction into the basic principles of laser spectroscopy. This is followed by an overview of the range of available THz sources and detectors and their potential applications. After which, a more in-depth examination of the laser source used in this project, the QCL, is given. This Section serves to provide the relevant theory behind the THz QCL, as well as specifics into the fabrication process. At the end of this chapter, an overview of active and passive sensing can be found.

2.1 Laser Theory

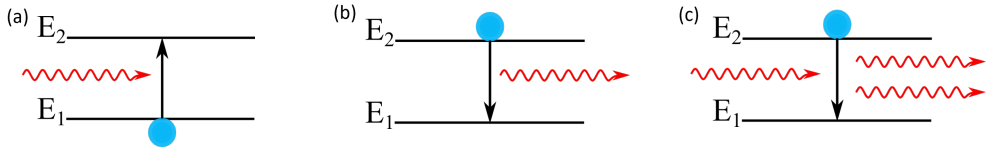

Figure 2.1: Schematic illustration of three different interactions between light and electrons (a) absorption (b) spontaneous emission. and (c) stimulated emission

In a simple electronic system with two energy levels, a photon is emitted upon an electron transitioning from the upper energy level (E_2) to the lower energy level

(E_1), with the frequency of the photon being equal to:

$$\nu = \frac{E_2 - E_1}{h} \tag{2.1}$$

where ν is the frequency and h is Planck's constant.

There are three interactions that can occur between light and electrons: absorption, spontaneous emission and stimulated emission. Absorption (see Figure 2.1a) is a process where an incident photon is absorbed and an electron is excited from E_1 to E_2 and no photon is emitted. The change in population of E_2 during absorption is given by,

$$\frac{\partial N_2}{\partial t} = B_{12} p(\nu) N_1 \tag{2.2}$$

where N_2 and N_1 are the populations of the upper and lower energy level, B_{12} is Einstein's B coefficient and is the probability (per unit time) of an electron transitioning from E_1 to E_2 and $p(\nu)$ is the energy density of radiation [49].

Figure 2.1b depicts spontaneous emission. This is a random process where an electron from E_2 relaxes to E_1 without external perturbation and a photon is emitted. The emitted photons are not in the same phase or direction as one another, otherwise known as incoherent radiation. The population of E_2 will decrease as spontaneous emission occurs, the rate of which can be calculated using the equation,

$$\frac{\partial N_2}{\partial t} = -A_{21} N_2 \tag{2.3}$$

where A_{21} is the probability of the electron transitioning from E_2 to E_1.

In stimulated emission (see Figure 2.1c), if the energy of the incident photon equals $h\nu$, an electron transitions from E_2 to E_1. The emitted photon is in the same phase and direction as the incident photon, known as coherent radiation. The rate of change in the population of E_1 is written as,

$$\frac{\partial N_1}{\partial t} = B_{21} p(\nu) N_2 \tag{2.4}$$

where B_{21} is the probability of the electron transitioning from E_2 to E_1.

For stimulated emission to be greater than absorption (i.e. a net amplification of photons), E_2 must have a greater population than E_1 (a population inversion). This cannot be achieved naturally under thermal equilibrium conditions, shown by

the Boltzmann equation,

$$\frac{N_2}{N_1} = e^{-\left(\frac{E_2 - E_1}{kT}\right)} \tag{2.5}$$

where k is the Boltzmann's constant and T is the equilibrium temperature. Through this equation it can be shown that the population of E_2 will never exceed that of E_1 as the temperature must be positive. Consequently, for stimulated emission to occur, the system needs to be in a non-equilibrium state, e.g. through a three-level system with an external optical or electrical pump.

A three-level laser medium was first demonstrated by Maiman in 1960 with a ruby crystal [13]. In a three-level system (Figure 2.2), electrons are 'pumped' into the upper level E_3 by photon pumping, electrical discharge, or collisions arising from chemical reactions. The lifetime of the electrons in E_3 is short and they will rapidly decay to E_2, with this transition typically being non-radiative. The decay time from E_2 - E_1 is much longer than between E_3 - E_2, meaning that a population inversion now occurs between E_2 and E_1. An electron in E_2 can now transition through stimulated emission down to E_1. For there to be a population inversion, more than 50 % of the electrons are required to be in E_2. As a result, a lot of pump power is needed.

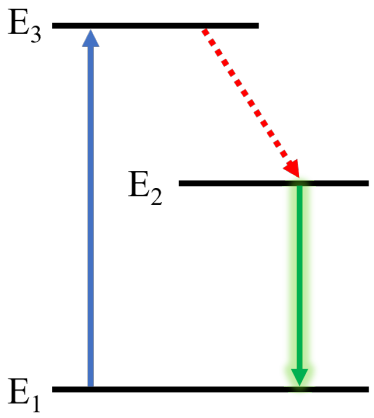

Figure 2.2: Three-level laser system.

Alternatively, a more efficient system is a four-level laser medium (see Figure 2.3). In this system, electrons are pumped into E_4 and quickly decay down to E_3. The lasing transition here is E_3 - E_2, the lifetime in E_2 is so short that no population of the level is likely to occur before the electrons transition down to E_1, the ground state. Because of this, fewer electrons are needed to be pumped to E_4 to create a population inversion between E_3 and E_2 and therefore a smaller pump power is

required as opposed to a three-level system.

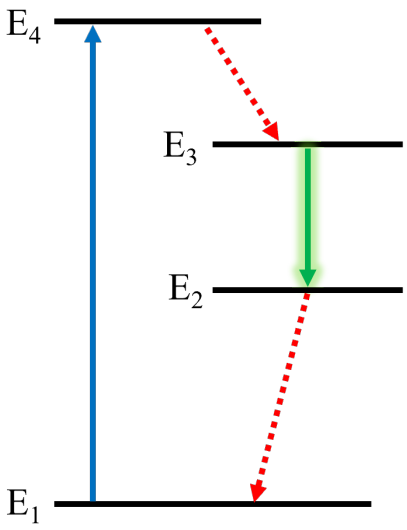

Figure 2.3: Four-level laser system.

Even with a large population inversion, the gain is still relatively small. To achieve a high gain, a positive feedback mechanism is needed. To implement this, the laser medium is placed between two reflective mirrors, one of which is highly reflective whilst the other is partially reflective. This laser cavity is known as a Fabry-Perot cavity. By doing so, emitted photons can be reflected back into the lasing medium to be reused in order to amplify the signal. The length of the laser cavity has to be such that constructive interference occurs at the target wavelength, i.e. the cavity path length is equal to an integer number of half wavelengths. Figure 2.4 shows the cavity modes for n = 1, 2 and 3.

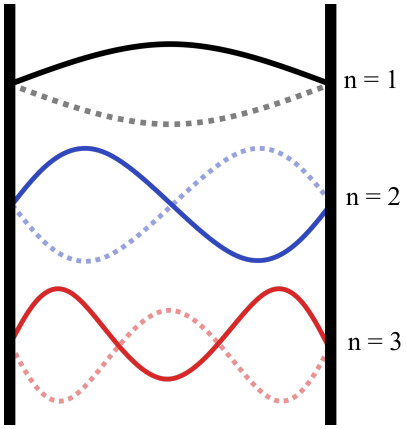

Figure 2.4: Harmonics of a standing wave.

All other wavelengths will destructively interfere within the cavity and will not be transmitted. As such, only specific wavelengths are present at a given cavity length, known as Fabry-Perot modes.

2.2 Active THz Sources

THz radiation sources are typically defined as being either broadband or narrowband radiation sources. Two of the most common methods used to emit broadband THz radiation are based on photoconductive antenna (PCA) or optical rectification. In both methods, a fs laser (usually a Ti:Sapphire laser emitting around 800 nm), is coupled to either a photoconductive (PC) emitter [50] or an electro-optic (EO) crystal [51]. The PC emitter is a PC switch fabricated onto a GaAs (traditionally) semiconductor. The fs laser emits an optical pulse with a wavelength larger than that of the semiconductor bandgap, creating electron-hole pairs. A voltage is applied across the terminals of the switch that generates a strong electric field, causing the charges to accelerate away from each other and subsequently giving rise to an ultra-short broadband THz pulse. Similarly, the fs laser optical pulse can propagate through a nonlinear EO crystal, inducing a polarisation that also gives rise to a broadband THz pulse. These sources offer a very broad bandwidth, as well as working at room temperature. However, the output power is extremely low and it is challenging to perform measurements with a high spectral resolution.

For the purpose of performing gas-phase spectroscopy, a narrowband laser source is preferred. Gaseous spectral lines are narrower compared to those of liquids and solids. This is because gases are more dispersed through space, which reduces the likelihood of interactions. However, linewidth broadening can still occur, either through pressure broadening caused by collisions between gas atoms and/or molecules, as well as Doppler broadening caused by the motion of gas particles. These broadening effects are described by influence over the Einstein coefficients in equations 2.2, 2.3 and 2.4.

In addition to exhibiting sharper spectral features to other states, gas lines can appear very close together in frequency, which will also require high spectral resolution measurements.

There are now multiple narrowband laser sources that can work within the THz region. For example, backward wave oscillator (BWO) [52] and gyrotrons [53] are narrowband sources capable of achieving high output power (> 100 mW) up to approximately 3 THz. Alternatively, IR-pumped gas lasers can be used. Here, a CO_2 laser (standard output is $\sim$10 µm), is used to excite a molecular rotational transition of a gas, where the gas chosen depends on the required frequency. The most commonly used gas laser in the THz region is the CH_3OH laser emitting at 2.54 THz [54]. However, multiple different gas lasers are available, including CH_3F [54], NH_3 [55], and D_2O [56]. Whilst these lasers exhibit a large output power of a few hundred mWs, this power decreases over time as the laser has a tendency

to leak, causing a decrease of the gas pressure. Gas lasers have small tunability (a few MHz), as they are restricted to the one transition of the gas, and the need for a CO_2 pump laser increases the bulk of the system. In recent years, it has been demonstrated that mid-IR QCLs are a good alternate to the CO_2 laser, from which the tunability also increases [57].

Alternatively, frequency multiplication of electronic sources in the microwave region such as Schottky diodes [58] and resonant tunneling diodes (RTDs) [59] can be used. THz radiation is generated from harmonics of the input signal, owing to the non-linearity of the diode. They are commonly used as LOs and mixers in heterodyne spectroscopy (see Section 2.5). The main limitations of these sources is the output power. Whilst an amplifier is typically used alongside the diode, the power drops with each harmonic. As a result, these sources are typically restricted to frequencies below 1 THz [60]. For this project, the narrowband laser source used is a THz QCL, the principles of which are discussed in more detail in Section 2.4.

2.3 THz detection methods

THz radiation detection methods are commonly classified as being either coherent or incoherent. In a coherent detection scheme, the phase and amplitude of the THz field is measured. An incoherent detector rectifies the electric field of the incoming THz wave and generates a voltage or current proportional to the incident power [61]. Popular coherent THz detectors used are PC antennas [62] and EO-crystals [63] mentioned above in Section 2.2.

Golay cells [64], pyroelectric detectors [65] and bolometers [66] are all thermal incoherent detectors that are sensitive to the change in temperature caused by the incoming THz radiation. A bolometer detects the change in electrical resistance subject to a rise in temperature in comparison to the heat sink. Highly sensitive bolometers (like the one used in the FTIR measurements in chapter 5) rely on being cryogenically cooled first to remove thermal background noise. Golay cells and pyroelectric detectors work at room temperature, meaning they are much more susceptible to thermal noise, albeit they are more compact and robust in comparison to bolometers. Schottky diodes [67] are an example of electrical THz detectors that work on the principle that the incident THz radiation has sufficient energy to promote electrons over a barrier. They have an extremely fast response, although the detection frequency is determined by the design of the coupling antenna.

In this work two detection schemes were used. Self-mixing (SM) is a technique whereby the laser source, e.g. a QCL, also acts as a interferometric detector as the

radiation is intentionally reflected back into the laser cavity. This causes interference and induces a change in the lasers terminal voltage, which is sensitive to both the amplitude and phase of the reflected radiation. SM is discussed in more detail in chapter 4. Measurements taken using FTIR spectroscopy used a bolometric detector, discussed in chapter 5.

2.4 Quantum cascade laser

A traditional semiconductor laser, e.g. a diode laser, has its wavelength dictated by the size of the materials bandgap between the valence and conduction band. These lasers are extremely well established in the near-IR region, however cannot be used at THz frequencies. In the THz band, a semiconductor bandgap with a photon energy of <40 meV is required to reach below 10 THz, something which to date, is not available. For that reason, a different approach is needed in order to generate THz radiation.

From the basis of semiconductor lasers (principles discussed in Section 2.1), Kazarinov and Suris in 1971 developed the idea of stimulated emission occurring entirely in the conduction band, where radiation is now generated through intersubband transitions [68]. Faist et al. [69], built upon this idea and produced the first QCL, an intersubband cascade laser designed by overlapping multiple quantum wells (QWs) that are slightly offset from one another, forming 'minibands'.

Equation 2.6 gives the energies of the individual electron states in an infinitely deep QW. When QWs overlap, the electron states in neighbouring QWs interact and shift to different energies. With the well width being inversely proportional to the energy of the state, decreasing the width of a QW will result in an increase in the energy of the electron state. Therefore, the operating frequency of a QCL is governed by the thickness of the QW rather than the bandgap of the semiconductor. For this reason, different materials can be used in the fabrication of QCLs.

$$E = \frac{\hbar^2 \pi^2 n^2}{2 m_e L^2} \tag{2.6}$$

where n is the quantum number of the energy state, m_e is the effective mass of an electron, and L is the well width of the QW.

In practice though, for a multi-layer structure such as a QCL, the energies of states are much more complex, and must be calculated numerically.

Figure 2.5 depicts a schematic diagram of a QCL. A QCL is made up of two regions, the active region and the injector/extractor region. Electrons are firstly injected into

the higher energy level (E_3) of the active region in the QW. Population inversion occurs and as the electron transitions down to the lower energy level (E_2) a THz photon is emitted. There are a number of different ways to achieve population inversion, the most popular ones utilised are discussed in Section 2.4.2. The electron relaxes into the extractor region where resonant tunnelling occurs and the electron is injected through to the adjacent QW and the process repeats itself. As a result of this, one electron has the ability to produce multiple THz photons as it 'cascades' through the multiple layers (QWs) of the QCL.

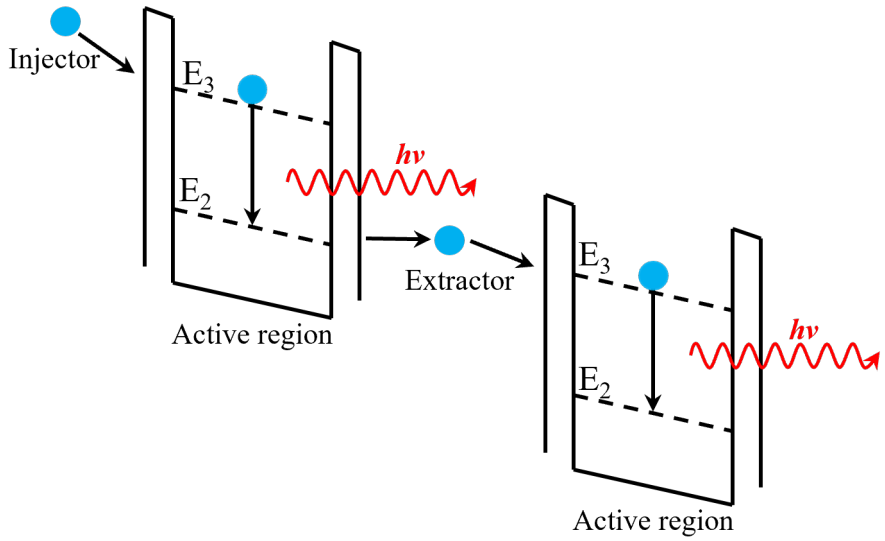

Figure 2.5: Schematic illustration of a QCL. The energy of the E_2 state of the first quantum well is higher in energy than the upper lasing level (E_3) of the adjacent QW, causing a 'cascade' effect.

For a number of reasons, the materials used for mid-IR QCLs cannot also be used for THz frequencies. Firstly, the energy spacing required to generate THz is typically between 4-25 meV, much smaller than what we see in mid-IR QCLs. This means it is difficult to inject an electron into the correct subband to create population inversion because the subbands are spaced so closely together. There is also a risk of a decline in population inversion and hence gain from thermal backfilling and thermally activated phonon scattering. Thermal backfilling occurs when an electron from the injector region of a QW is thermally excited back to the lower energy level of the previous QW. Thermally activated phonon scattering is caused by the electrons having sufficient kinetic energy to emit a longitudinal optic (LO) phonon rather than a photon [70]. As such, THz QCLs are required to operate at cryogenic temperatures. These complexities delayed the production of the first THz QCL until almost a decade after the creation of the first QCL. In 2002, Kohler et al. [71] developed a THz QCL emitting a few milliwatts of power at 4.4 THz from a GaAs/AlGaAs wafer grown using molecular beam epitaxy (MBE) [72]. Various

other materials have now been demonstrated to work at THz frequencies, including n-doped InGaAs/InAlAs [69] and and InGaAs/AlAsSb [73]. Since, THz QCLs have been widely utilised in imaging [74], communication [75], and spectroscopy applications [76] up to 5 THz. Above 5 THz we reach the Restsrahlen band of multiple different polar semiconductors, where the light is reflected (rather than absorbed) because the photon of light interacts strongly with the optical phonons in the semiconductor crystal.

2.4.1 Active region designs

The four main THz QCL designs are shown in Figure 2.6. The first THz QCL mentioned in Section 2.4 adopted a chirped superlattice (CSL) active region design (Figure 2.6a). Population inversion occurs between an upper miniband and the lower energy state, however since the electron can be injected into many upper energy states within the miniband, the frequency of the emitted THz photons can vary. In addition, the CSL design means the QCL is much more susceptible to thermal backfilling and thermal assisted phonon scattering mentioned above. A bound-to-continuum (BTC) design (Figure 2.6b) was first demonstrated using mid-IR QCLs [77] before it was successfully used in the fabrication of a THz QCL operating at 3.5 THz in 2003 by Scalari et al. [78]. Here, electrons are injected into an isolated upper energy state that is adjacent to the injection barrier. In doing so, population inversion occurs between one single upper energy level and a lower energy level in an adjacent miniband which leads to a much narrower frequency range as opposed to the CSL design. In addition, the increase in injection efficiency leads to an improvement in the power and thermal performance. The resonant phonon (RP) design [79] (Figure 2.6c) replaces the extractor region employed in CSL and BTC design schemes with LO phonon-scattering to depopulate the lower energy state. This method of depopulation reduces the chance of thermal excitation, but a much larger drive current of up to 2 A with a voltage typically above 10 V is required. Because of the larger drive current, the device will heat up, and therefore QCLs that adopt this design are typically limited to pulsed operation only. An alternate active region is the hybrid/interlaced design (Figure 2.6d) that utilises aspects from both the BTC and RP designs. In this project, the QCLs have a hybrid active region unless otherwise stated.

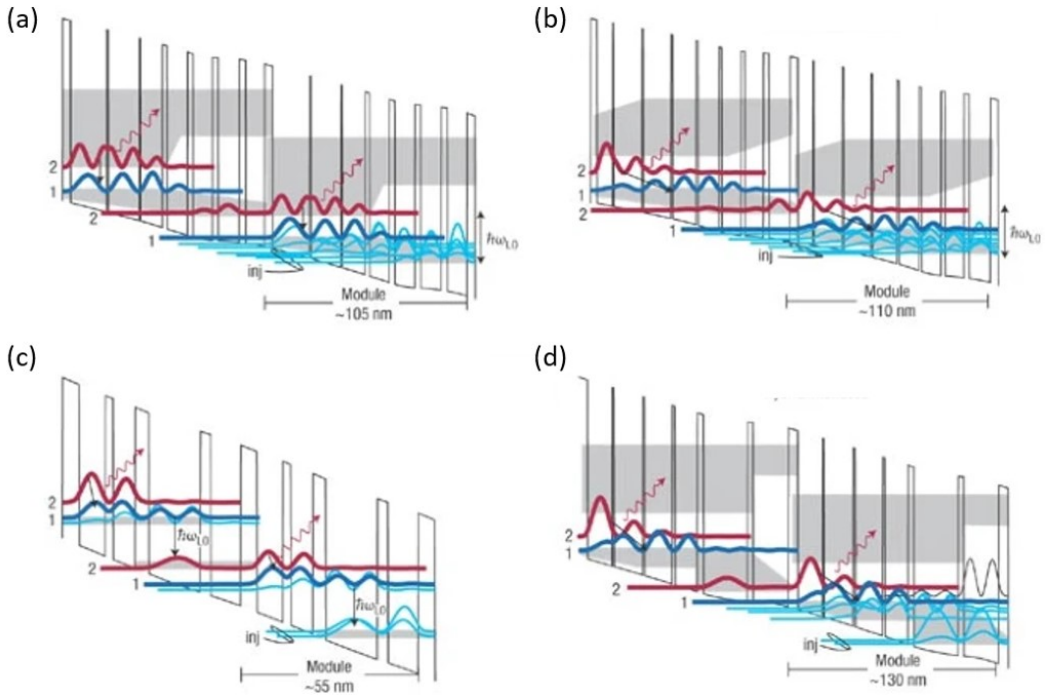

Figure 2.6: The four main active region designs used in THz QCLs, (a) CSL, (b) BTC, (c) RP and (d) a hybrid design which is a combination of BTC and RP. Figure taken from [70].

2.4.2 Waveguides

In order to increase the gain and control the directionality of the radiation from a THz QCL, the laser medium must be confined within a waveguide. As well as it being required that the wave must reproduce itself after a round trip in the Fabry-Perot cavity, the gain must also be equal to the total loss. The threshold condition is given by,

$$\Gamma g_{th} = \alpha_w + \alpha_m \tag{2.7}$$

where Γ is the confinement factor, g_{th} is the threshold bulk gain of the active region, α_w is the waveguide absorption loss and α_m is the mirror loss calculated by,

$$\alpha_m = \frac{-\ln(R_1 R_2)}{2L} \tag{2.8}$$

where R_1 and R_2 are the reflectivities of the mirrors and L is the cavity length.

For dielectric waveguides (or fibres) mostly used at mid/near-IR and optical frequencies, light is confined between two materials of different refractive indexes. At THz frequencies, this approach required the wavelength to be smaller than the dimensions of the device structure. For example, in this project a wavelength of 88 µm

is used. For the QCL to be grown via MBE to a thickness larger than this would be extremely time consuming. Moreover, adding additional layers also comes with a risk of introducing defects into the waveguide. Instead at THz frequencies, metallic waveguides are used, with the most common being the semi-insulating surface plasmon (SI-SP) waveguide [80] and the double-metal (DM) waveguide [81] shown in Figure 2.7. The SI-SP waveguide has one metal layer above the active region, and a highly doped semiconductor layer below. A surface-plasmon mode is formed, in which the THz electric field propagating at the semiconductor surface is coupled to charge oscillations at the metal boundary. However as shown in Figure. 2.7, radiation leaks into the substrate layer below the active region.

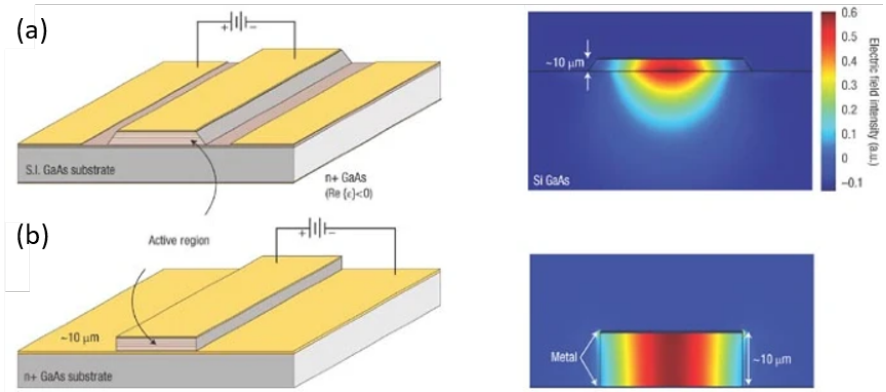

Figure 2.7: Schematic diagrams of (a) SI-SP and (b) DM waveguide and their corresponding two-dimensional mode intensity pattern. Figure taken from [70].

The DM waveguide overcomes this issue by having an additional metal layer below the active region. As a result, there is less leakage between the layers, with the metal layers acting as a heat sink which increases the thermal performance of the device. This comes at a cost, as the output beam becomes extremely divergent [82], causing the DM waveguide to exhibit poorer output power compared to a SI-SP waveguide. The use of a diagonal feedhorn to collimate the radiation (discussed in more detail in the following chapter) helps to increase the output power.

The waveguides mentioned are based on Fabry-Perot cavities, where the QCL emission is relatively broadband. For applications that require a narrowband tunable emission, i.e. chemical sensing, modifications have to be made. A single mode QCL can be made by using a distributed feedback waveguide structure [83–85]. A layer of grating is incorporated into the topmost layer of the waveguide at a selective wavelength. In both waveguide structures, the modes can be tuned through thermal and electrical bias control. The frequency of a QCL shifts with temperature and/or a change in the driving current. Increasing the current to the QCL causes the laser

cavity to heat up, which causes a frequency shift in the allowed modes.

2.4.3 QCL Performance

Through the various different active region designs and waveguides that have been developed over the years, the frequency coverage, temperature, and output power performance of THz QCLs has drastically improved. To date, THz QCLs cover the spectral band between 1–5 THz [71, 86–88] and have been shown to work at 261 K at 4 THz in pulsed mode [89] and 117 K in CW at 3 THz [90]. At present, the highest output power achieved is reported to be ~ 2.4 W in pulsed mode operating at 4.4 THz at 10 K [91], whilst in CW mode, an output power of 230 mW has been achieved from a QCL operating at 3.1 THz [92].

2.5 Active and Passive Sensing

Gas spectroscopy measurements can be obtained either actively or passively. Passive sensing uses only a detector or receiver to measure the EM radiation that is naturally emitted from the gas under study or from solar radiation. In active sensing a source is used to generate the EM radiation and a detector/receiver is used to measure any absorption of the radiation from a gas. One popular technique for passive remote sensing is heterodyne spectroscopy, mentioned briefly in Section 1.4. Shown in Figure 2.8, the LO, emitting at a frequency ν_{LO} and the frequency of the gas signal ν_{s} picked up by the receiver are directed into a mixer. The output signal from the mixer is the intermediate frequency (IF), that is $\nu_{IF} = \nu_{LO} - \nu_s$, and is typically in the GHz or MHz range. The IF signal is then amplified and filtered by the IF processor and the result is a gas spectrum at ν_{IF} that can be detected using conventional microwave electronics [93]. This technique has been widely used in the microwave/submillimetre-wave region, where the instrumentation is readily available. Progress is now being made on developing specialised components to work as mixers and LOs within the THz spectral band. Because of their robustness, compact size, and low energy consumption, QCLss can potentially be used as a LO. In this work, QCL characterisation was done in order to judge their suitability for heterodyne spectroscopy applications, found in chapter 3.

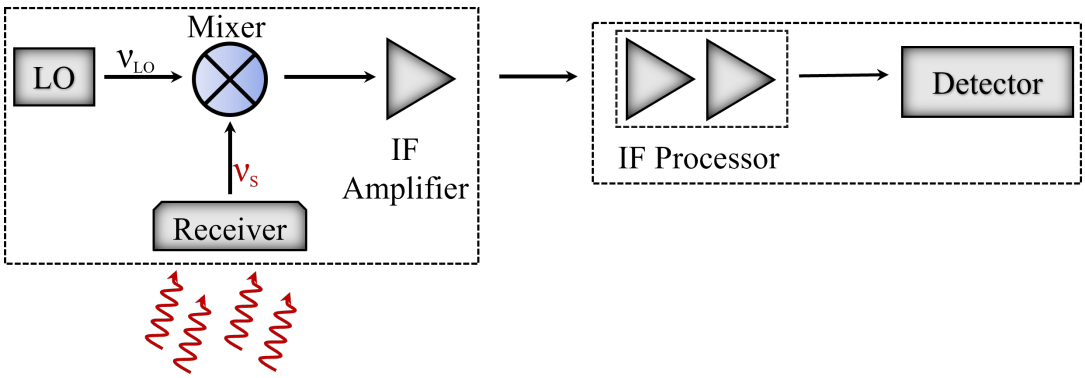

Figure 2.8: Components of a heterodyne receiver. The red arrows indicates the incoming gas signal. Figure adapted from reference [93].

Chapter 3

THz quantum cascade lasers for gas-phase spectroscopy

In chapter 2, an introduction to THz QCLs was given, where its uses for spectroscopy over other THz sources was highlighted. QCLs are narrowband lasers, with a high emission intensity whilst still being compact in size.

When considering gas-phase spectroscopy, the ideal QCL would be a multimode device. The advantage of using a multimode device for gas spectroscopy is highlighted in Chapter 4, where it enables multiple peaks to be resolved. Additionally, in order to replicate atmospheric conditions and the detection of trace gases in the laboratory, the QCL should have a sufficiently high output power.

Conversely, if the QCL is intended to be used as a LO in heterodyne spectroscopy, the size of the device is more crucial, especially in applications that have weight and size constrains, e.g. KEYSTONE (see Section 1.4) is planned to be a small satellite and has a weight constraint of 150 kg in total [46]. Moreover, it is favourable to have linearly polarised QCLs for effective coupling into mixers (see Section 3.1). Lastly, atmospheric and space missions tend to focus on monitoring one particular molecule or atom. Because of this, ideally the QCL should be single-mode, emitting at a frequency close to a transition of the target species.

For both applications, it is advantageous for the QCL to be operating in CW so as to minimise any instability associated with pulsed mode. The QCL should also have minimal divergence, allowing efficient coupling of radiation into the respective detector or mixer.

This chapter begins with an overview of the integration methods that can be used to improve the beam quality of a QCL. The QCLs used in this project are enclosed within a metallic waveguide structure, described in the following Section, along with

the characterisation and spectral results. This includes LIV and emission spectra in Section 3.2, as well as beam profiling measurements in Section 3.3. Within these sections, a thorough analysis of the thermal properties and beam quality is found.

3.1 QCL integration

An unmounted QCL, shown in Figure 3.1, exhibits poor spatial power distribution with a beam divergence upwards of $> 100°$ [82] and non-Gaussian far-field beam quality. THz QCLs have a typical total thickness of 10–15 µm, which is considerably smaller than the emitted wavelength, causing the beam to be extremely divergent (discussed in Section 3.3 and described using equations 3.24 and 3.25 . Therefore, their uses are limited when it comes to free-space applications. Through device assembly [94–96] or with the additional use of antennas and lenses [97, 98] the beam quality can be improved. However, for QCLs to be realised as a potential laser source in space and atmospheric applications, e.g. heterodyne spectroscopy (see Section 2.5) the QCL must be integrated with external components such as waveguides and mixers, whilst negating the need for additional optics that increase the risk of misalignment during launch. In addition, the integration method must be compliant for satellite and aircraft use, i.e. must be within an allowed volume, mass and power consumption.

Over the years, a number of methods have been proposed to address the beam quality of a THz QCL, with progression towards a completely integrated heterodyne system. For example, Wanke et al. [99] integrated a Schottky diode monolithically into the QCL waveguide cavity. By doing so, no optical coupling path is required to the mixer. Similarly, in 2015, Miao et al. [100] demonstrated the successful integration of a hot electron bolometer (HEB) mixer and a THz QCL in a single cryostat.

In the aforementioned methods however, there are some issues. With regards to the monolithic integration of a QCL with a Schottky diode mixer, they have both been grown on the same wafer, meaning this integrated circuit is extremely complicated to make. Furthermore, the HEB mixer and QCL still requires optics which makes the system bulky and fragile. The HEB mixer is also at risk of not working, owing to the high heat output from the QCL. In this project an integration method that is compliant for space operation, as well as being mechanically robust and reproducible is used.

In this project, the QCLs used are integrated into a precision micro-machined metallic waveguide cavity with a diagonal feedhorn (see Figure 3.2a). This concept was first demonstrated in the microwave region [101] using horn antennas and has now

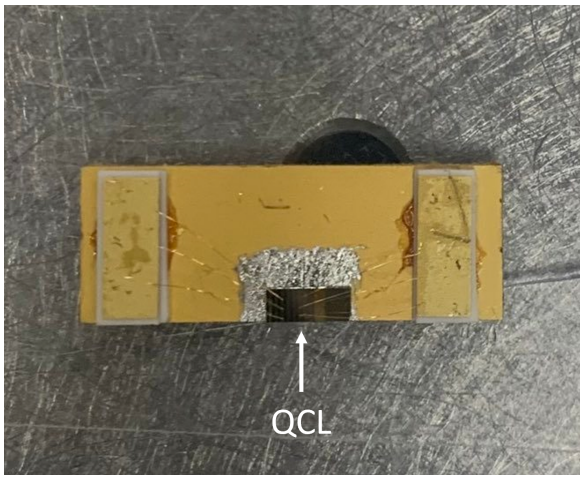

Figure 3.1: Unmounted THz QCL is indium (In) soldered onto a Au plated Cu submount with the QCL wired to two Au coated ceramic bonding pads.

been adapted to work at THz frequencies, yielding a beam divergence of $< 20°$ [102]. THz QCLs with rectangular apertures [102] were demonstrated before a diagonal feedhorn design [103, 104] was later adopted. The use of a diagonal feedhorn minimised the beam divergence further as the beam now gradually disperses from the block. A cylindrical feedhorn would further improve the beam quality, however the manufacturing process detailed below becomes increasingly more complex.

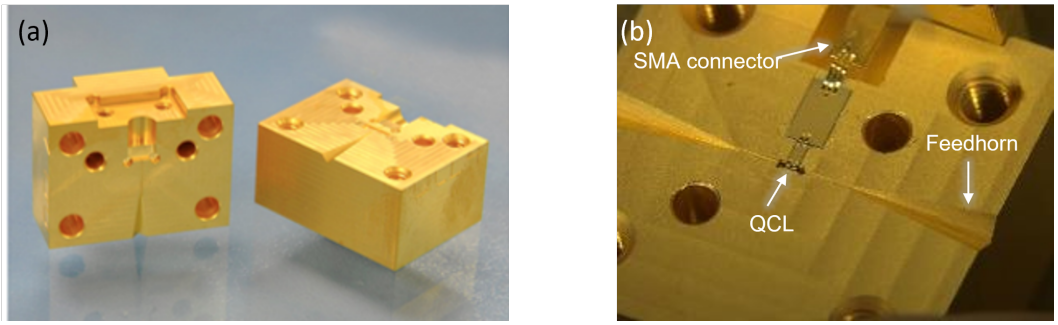

Figure 3.2: (a) Pair of metallic waveguide modules and (b) interior of a metallic waveguide with an integrated QCL.

A waveguide cavity is precision milled by the RAL Space Precision Development Facility into a pair of oxygen-free Copper (Cu) blocks with a diagonal feedhorn machined at each end of the waveguide channel. The QCL is solder-mounted within the waveguide channel and the pair of Cu blocks are assembled together using alignment dowels to form a rectangular waveguide. Figure 3.2b shows the metallic waveguides with an integrated QCL. The heat sink temperature of the QCL is monitored using a temperature sensor attached to the block (Figure 3.3a) and is biased through a subminiature-A (SMA) connector on the back facet of the device (Figure 3.3b). Before the QCL is mounted, the Cu blocks receive diamond turning and electro-less

gold plating to improve surface roughness, thermal performance, and to prevent corrosion.

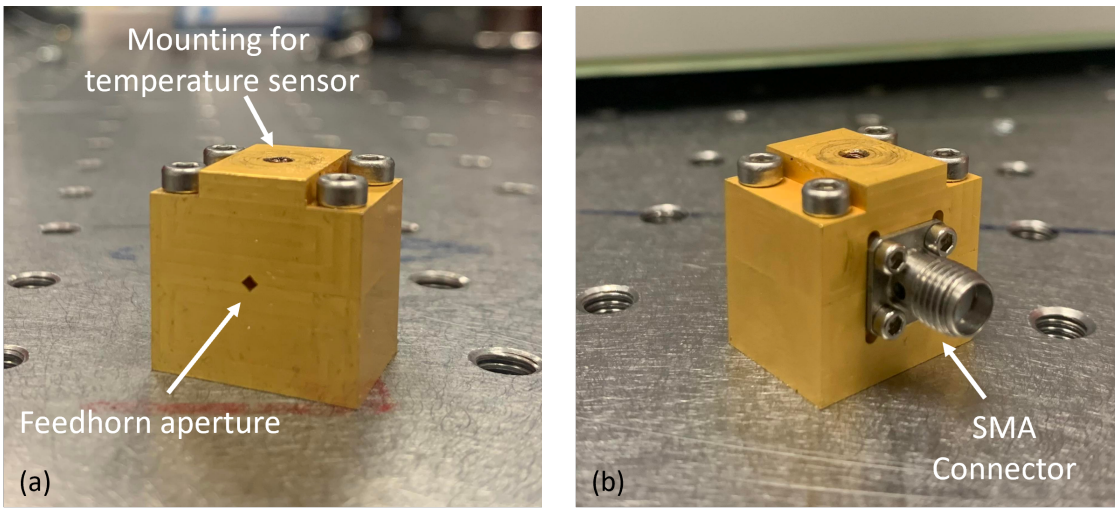

Figure 3.3: (a) Front facet of the QCL showing the diagonal feedhorn aperture and temperature sensor and (b) the back facet of the QCL with the SMA connector.

3.2 QCL characterisation

In this project, two THz QCLs operating at 3.4 THz and one THz QCL at 4.7 THz were used. The 3.4 THz QCLs had a single diagonal feedhorn machined into each metallic waveguide block. For the 4.7 THz QCL, two diagonal feedhorns at each end of the waveguide channel were machined.

The two 3.4 THz QCLs used in this project were fabricated from the same GaAs substrate grown using MBE. However, the devices had different ridge widths. 'Device A', had a length of 980 µm and a width of 55 µm. 'Device B' had a length of 980 µm with a wider ridge of 60 µm. Aside from the different ridge width, the fabrication process remained the same and is detailed in the next Section. The fabrication process for the 4.7 THz QCL is discussed in Section 3.2.5.

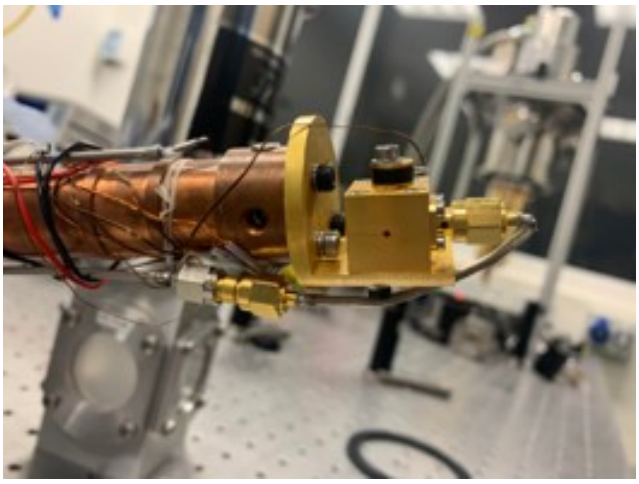

Figure 3.4: Block integrated QCL mounted onto a Janis cryostat.

In the next Sections, a thorough characterisation (LIV and spectral) of each QCL is given. In all cases, the QCL was mounted onto the cold-finger of a Janis ST-100 liquid-helium cryostat (see Figure 3.4).

The emitted THz radiation was coupled into a helium-cooled silicon (Si) bolometric detector using a pair of off-axis paraboloidal mirrors. The temperature was controlled using a Lakeshore model 336 temperature controller. For pulsed characterisation, the QCL was driven using an Agilent 8114A high-current pulse generator at 10 kHz 2 % duty-cycle and modulated at the optimum frequency for bolometric detection, 167 Hz. The emission spectra of the QCL was recorded using a Bruker FTIR spectrometer. FTIR spectroscopy is discussed in more depth in chapter 5, however the basic principle is that FTIR uses interferometry to obtain information in the spatial-domain that is then Fourier transformed to output a spectrum in the frequency domain. For CW characterisation an Aim-TTi QL564P power supply was used to drive the QCL. The THz beam was modulated with an optical chopper at 167 Hz. A schematic diagram of the set-up used is given in Figure 3.5.

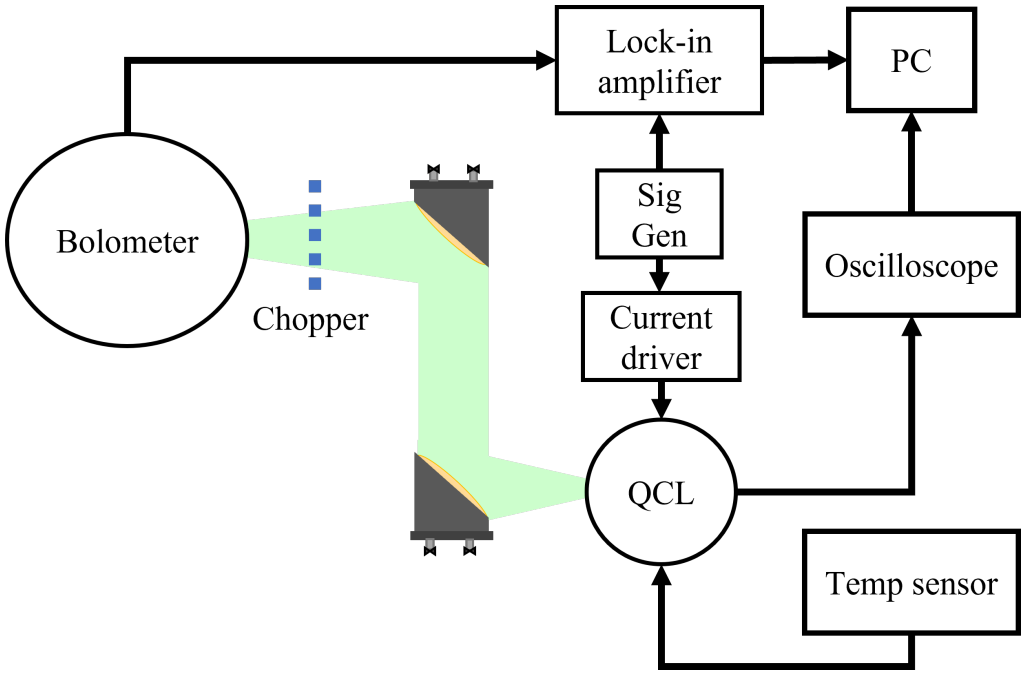

Figure 3.5: Schematic diagram of the experimental setup used for QCL characterisation. The QCL is driven using the current driver. The temperature of the QCL is monitored with the temperature sensor. For pulsed characterisation, the signal generator (Sig Gen) emits a square wave at the optimum response frequency of the bolometer (167 Hz). In CW operation, the chopper is used to optically modulate the signal. The QCL current and voltage is measured on the oscilloscope. The voltage output from the bolometer is measured on the lock-in amplifier.

3.2.1 3.4 THz QCL fabrication

On top of the GaAs substrate is a GaAs buffer layer and a 300 nm-thick $Al_{0.5}Ga_{0.5}As$ etch-stop layer, followed by a 700 nm-thick silicon (Si)-doped n^+-GaAs contact layer with a doping density, $n = 2 \times 10^{18}$ cm^{-3}. The active region, based on a hybrid design [105], was grown to a total thickness of 14 µm (see Figure 3.6). After which, a 50 nm-thick Si-doped n^+-GaAs contact layer (5×10^{18} cm^{-3}) was grown. A titanium/gold (Ti/Au) layer of thickness 10/500 nm was deposited on top of the QCL wafer, as well as on a n^+-GaAs acceptor wafer. The two wafers were thermal compression bonded at the metallic interfaces and processed into a gold-gold (Au-Au) waveguide structure using wet chemical etching. A Ti/Au layer of thickness 10/150 nm was deposited on top of the waveguide, before the substrate was thinned.

The QCL channel was precision-machined directly into a Cu block with cross-section dimensions of 300 µm × 150 µm. The QCL was mounted into the rectangular channel using indium (In) foil to achieve a good thermal contact. At one end of the waveguide was a diagonal feedhorn with an across-diagonal aperture of 1.56 mm × 1.56 mm and a slant angle of 7.5° [106]. Lastly, the waveguide block underwent a process of electro-less gold plating in order to minimise the surface roughness and improve the

propagation and outcoupling of the radiation.

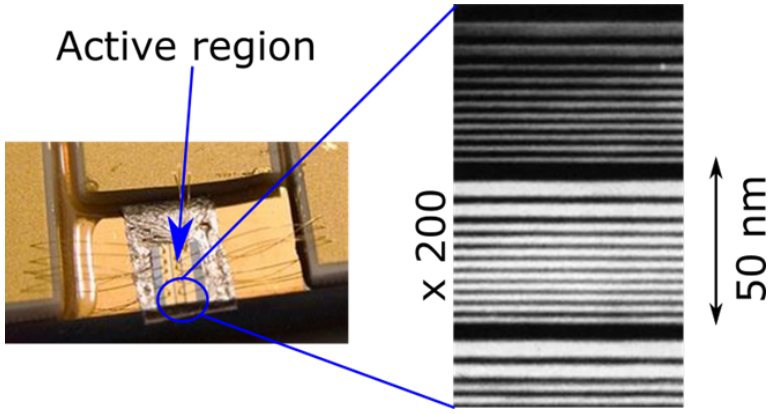

Figure 3.6: Image of a QCL active region with an enlarged microscope picture of the QCL layers.

3.2.2 Unmounted 3.4 THz QCL characterisation

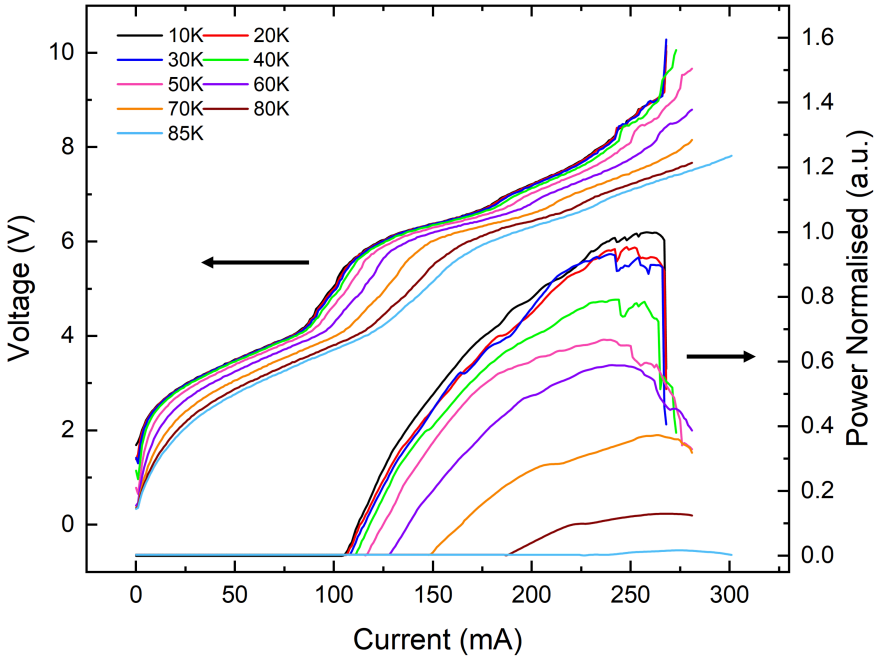

Figure 3.7: LIV curves of the unmounted 3.4 THz QCL in CW between 10–85 K. Current threshold at 10 K is 107 mA.

In Figure 3.7, the LIV characteristics of an unmounted (no integration) 3.4 THz QCL grown from the same wafer as Device A and B with dimensions of 980 µm × 75 µm is shown. The QCL was emitting in CW. The recorded current threshold is 107 mA at 10 K, with a maximum operating temperature of 80 K.

3.2.3 Device A characterisation

The LIV curves of Device A in pulsed mode with an 8 % duty cycle at various temperatures are given in Figure 3.8. The maximum operating temperature is 100 K with a current threshold of 98 mA, and an absolute power of 5 mW.

For comparison purposes, the current density J_{th} is typically used,

$$J_{th} = \frac{I_{th}}{L \times W} \tag{3.1}$$

where I_{th} is the current threshold, L is the length of the QCL and W is the width of the QCL.

Device A has a J_{th} value of 181 A cm^{-2}. Compared to the current density for the unmounted QCL in CW conditions, 145 A cm^{-2}, there is a slight increase. The difference in current density is most likely attributed to the thermal mounting of the integrated device. The operating temperature is also slightly higher for Device A. This is expected, since less internal heating of the device occurs in pulsed operation. This demonstrates successful integration of the QCL into the metallic waveguide, with minimal changes to its electrical properties. Although a higher current density is calculated for Device A, it is not detrimental to the lasing of the device.

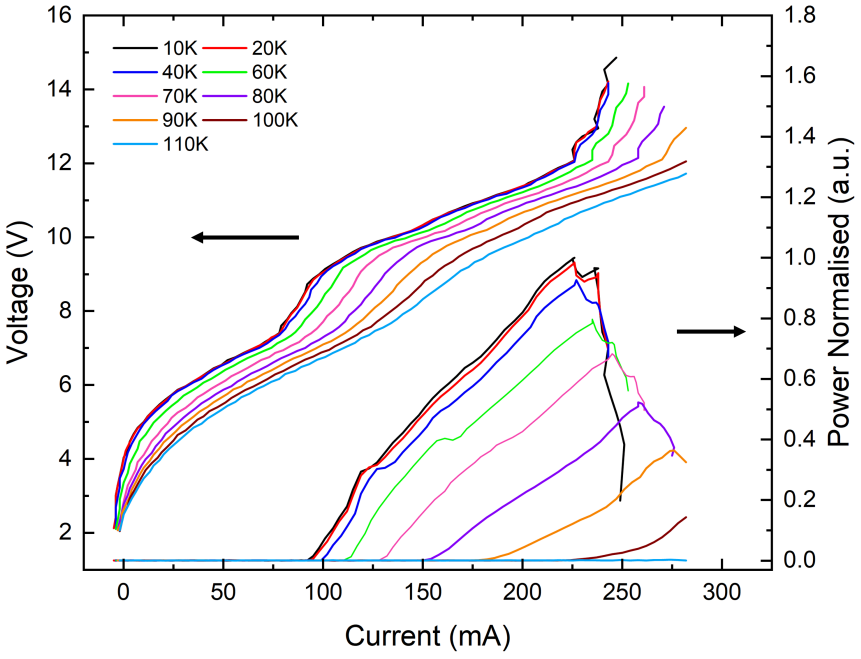

Figure 3.8: LIV curves of Device A in pulsed mode between 10–110 K. Current threshold at 10 K is 98 mA.

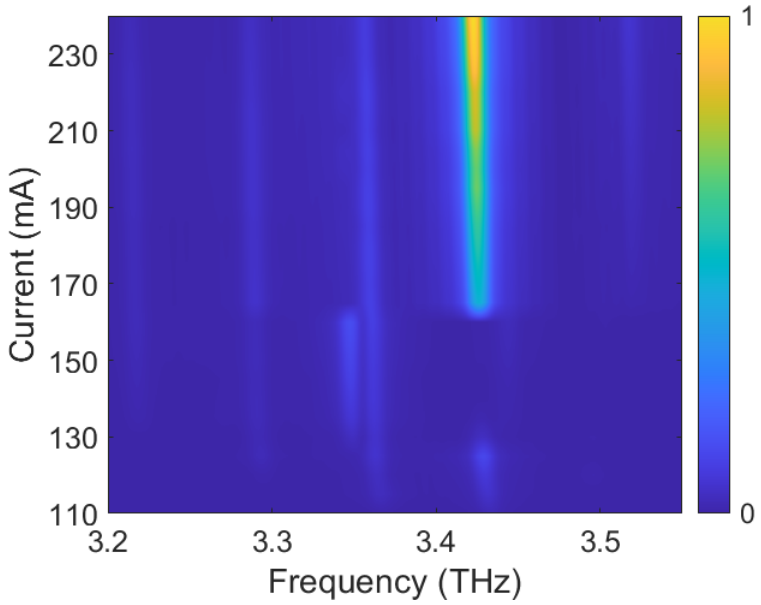

Figure 3.9: FTIR spectrum of Device A measured between 110–250 mA at a QCL temperature of 10 K. There are three main emission modes at 3.34 THz, 3.36 THz and 3.42 THz and three weaker emission modes at 3.21 THz, 3.28 THz and 3.51 THz.

The Bruker FTIR spectrum of Device A is shown in Figure 3.9. The spectrum was measured at 10 K between 110–250 mA with a step size of 5 mA. The Bruker had a spectral resolution of 0.25 cm^{-1}, a scan speed of 7.5 kHz, and 2 × zero-padding. Results show that Device A is a multimode QCL with three main emission modes at 3.34 THz, 3.36 THz, and 3.42 THz. In addition, there are three weaker emission modes at 3.21 THz, 3.28 THz, and 3.51 THz.

The free spectral range (FSR) describes the difference in frequency between two resonant modes inside a Fabry-Perot cavity. Using the following equation the FSR can be calculated,

$$\mathrm{FSR} = \frac{c}{2nL} \tag{3.2}$$

where c is the speed of light, n is the effective refractive index of the optical mode, and L is the length of the cavity.

For Device A, the FSR is estimated to be 43 ± 3 GHz where n typically has a value between 3.4-3.8 for THz QCL structures. From Figure 3.9, the FSR between the two modes 3.36 THz and 3.42 THz at 200 mA was measured as 67 ± 24 GHz, within the calculated range. The FSR between the 3.34 THz and 3.36 THz mode is 13.5 ± 7.5 GHz outside of the estimated FSR for this device. This value is expected, since equation 3.2 applies to a Fabry-Perot cavity, where reflections occur between two perfect mirrors. For a block integrated QCL, the formation of standing waves within the metallic waveguide also arise, as well as in different planes. In addition,

n can vary depending on whether the device is SI-SP or DM and the level of doping there is in the device (see Figure 2.7 for the two-dimensional mode profiles).

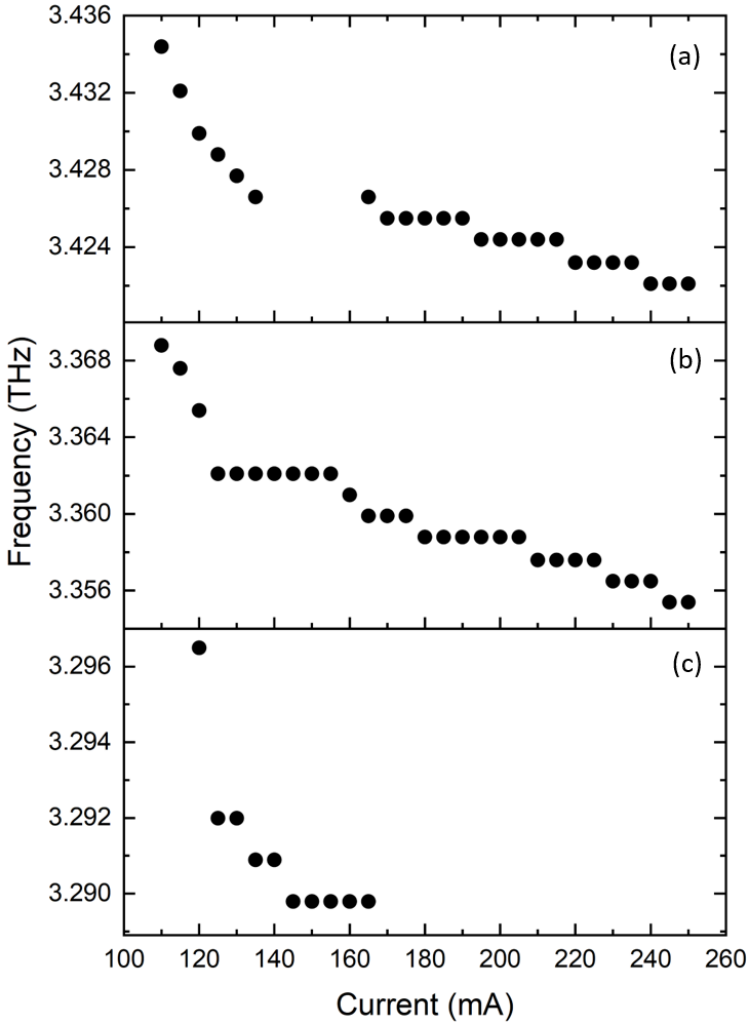

Figure 3.10: Frequency of the three main emission modes of Device A (a) 3.42 THz, (b) 3.36 THz and (c) 3.29 THz between 110–250 mA. Measurements taken at a QCL temperature of 10 K.

In Figure 3.10, the frequency of the three main emission modes, 3.29 THz, 3.36 THz and 3.42 THz between 110–250 mA is presented. In total, emission of the 3 modes is observed across a 32 GHz bandwidth (reason behind the frequency shift is discussed in Section 2.4.2). Referring back to Figure 3.9, the relative power of the 3.42 THz mode is 10.9 dB. From 160 mA, the 3.42 THz mode dominates. Below 160 mA, the power distribution over the three main emission modes is similar. This clearly demonstrates the advantage of using a multimode QCL as opposed to a single mode QCL, where the measurable bandwidth is greatly improved, resulting in possibly multiple gaseous lines being detected.

3.2.4 Device B characterisation

Device B, grown from the same QCL wafer as Device A with the exception of a larger ridge width of 60 µm, was also characterised. The LIV curves of Device B operating in CW are given in Figure 3.11. Under CW conditions, the recorded current threshold is 175 mA at 15 K. The QCL emits up to a temperature of 70 K, 10 K less than the equivalent CW LIV curve for the unmounted device present in Figure 3.7. In addition, the threshold current density for the device is 297 A cm^{-2}, a significant increase to that of the unmounted device. The reason being a thermal mounting issue arising from the integration method.

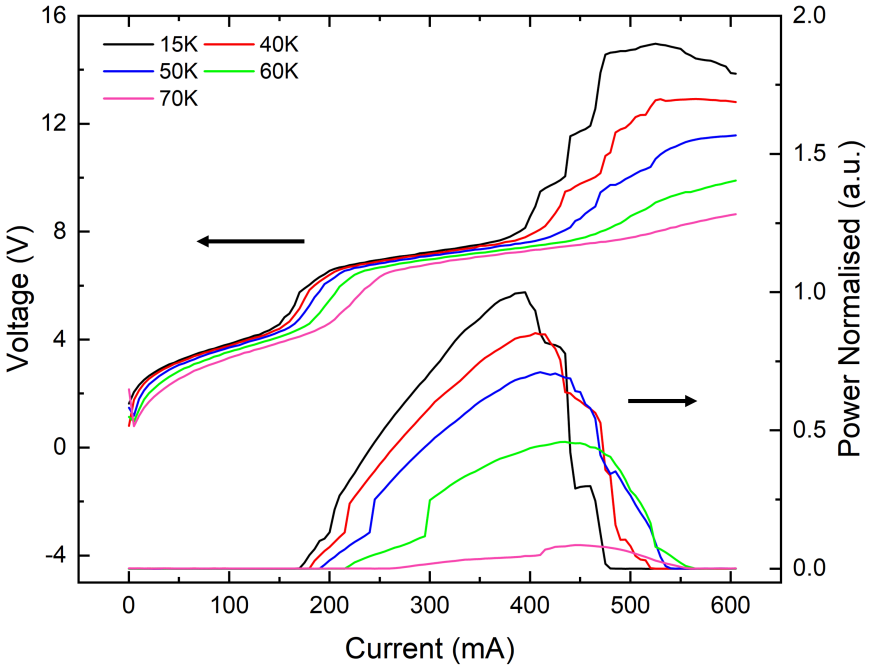

Figure 3.11: LIV curves of Device B in CW mode between 15–70 K. Current threshold at 15 K is 175 mA.

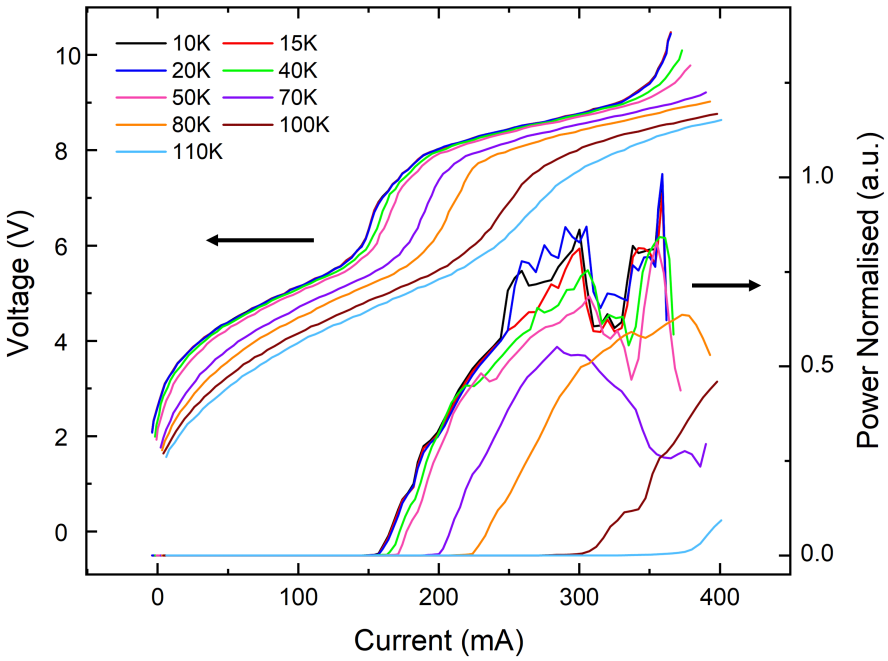

Figure 3.12: LIV curves of Device B in pulsed mode between 10–110 K. Current threshold at 10 K is 157 mA.

In Figure 3.12, the LIV plot of Device B in pulsed mode is shown. The maximum operating temperature of this device was 110 K, with a current threshold of 157 mA ($J_{th} = 267\,\mathrm{A\,cm^{-2}}$) measured at 10 K. Between 10 K and 70 K a decrease in power is observed between 300 mA and 350 mA. There is a possibility that this is attenuation from a residual water line, however this is not the case, as attenuation happens across all three modes. A more likely reason would be that within this current range, carrier leakage occurs whereby electrons leak into the continuum states rather than the intended upper lasing level of the adjacent QW [107].

The Bruker FTIR spectrum recorded with the QCL in pulsed mode is shown in Figure 3.13. The spectrum was measured at 10 K between 160–390 mA with a step size of 10 mA. As expected, Device B is a multimode device with three main emission modes at 3.25 THz, 3.36 THz, and 3.44 THz and one weaker emission mode at 3.41 THz.

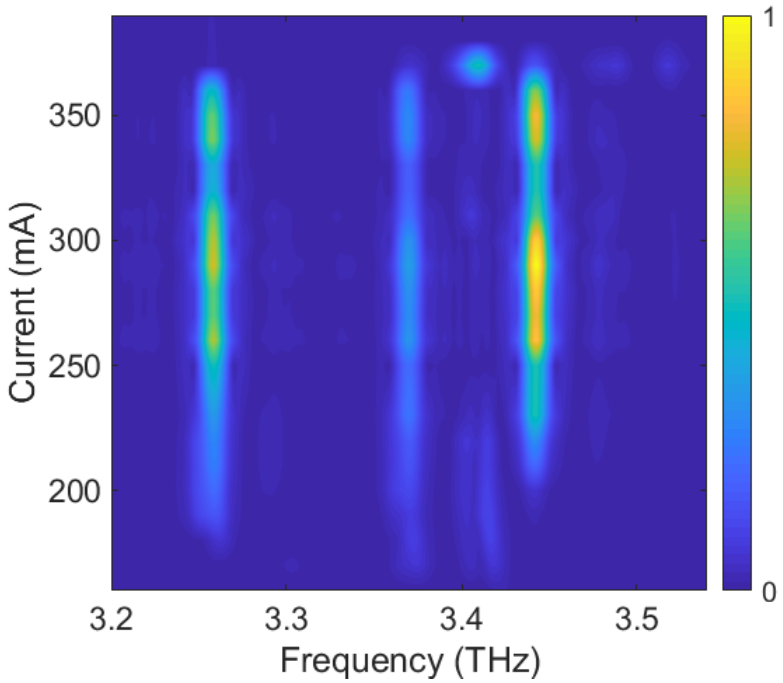

Figure 3.13: FTIR spectrum of Device B measured between 160–390 mA at a QCL temperature of 10 K. There are three main emission modes at 3.25 THz, 3.36 THz and 3.44 THz and one weaker emission modes at 3.41 THz.

In comparison to Device A, there are small variations in the lasing current range and frequency of the lasing modes. Device B exhibits a higher current threshold and has fewer active emission modes than Device A. Although grown from the same wafer, the larger ridge width will contribute to the increase in the current threshold. In addition, there will be small discrepancies during the fabrication process. For example, differences in the thickness of the layers across the wafer may occur when using MBE. Furthermore, there may be defects in the GaAs crystal used. In both instances, the electrical properties of the device, such as operating current and temperature can be affected. Once the QCL is integrated into the waveguide, the optical environment changes, which will influence the spectral characteristics e.g. the frequency of the laser modes.

The calculated FSR is 43 GHz ± 3 GHz. From Figure 3.13, the measured FSR between the 3.25 THz and 3.36 THz modes is 112 GHz ± 11 GHz whilst the FSR is 73 GHz ± 12 GHz for the 3.36 THz and 3.44 THz modes. Both results are outside the estimated range as with Device A, the reasons being the same as those discussed for Device A at the end of Section 3.2.3.

In Figure 3.14, the frequency of the three main emission modes, 3.25 THz, 3.36 THz, and 3.44 THz as a function of drive current is presented. As a result of the multimode nature of the device, the three modes emit across a bandwidth of 11 GHz.

The relative power of the 3.44 THz mode is 1.5 dB. Referring to Figure 3.13, the power distribution over the three main modes is relatively even, with the intensity becoming larger for the 3.44 THz and 3.25 THz between 250–300 mA, and again at 350 mA.

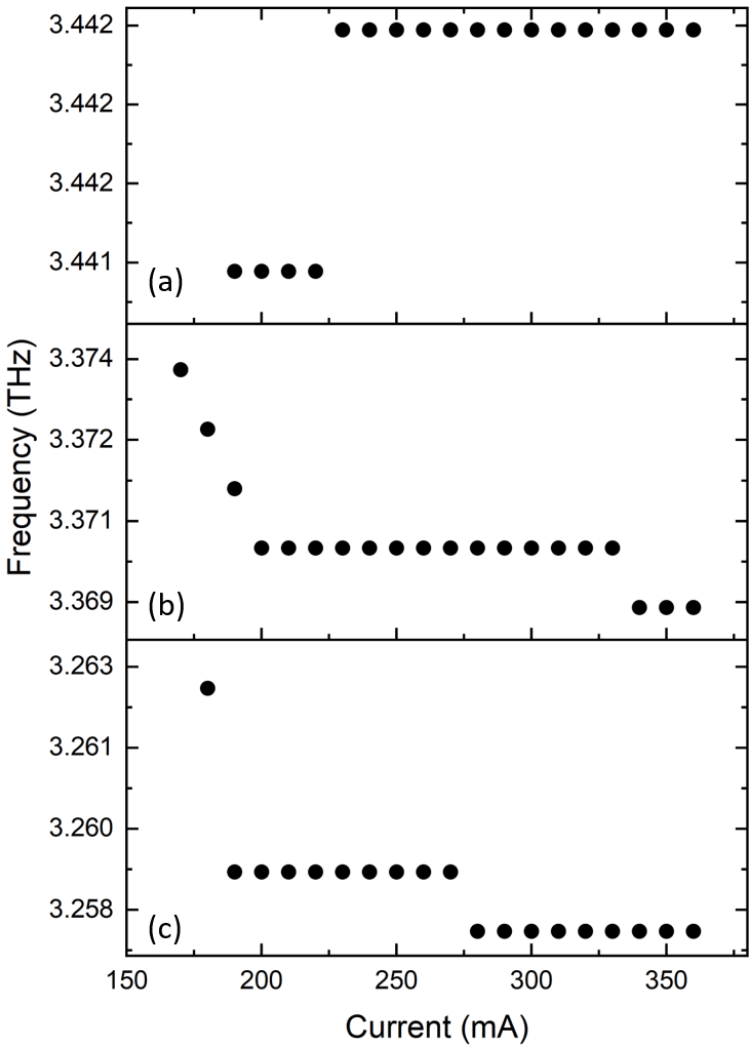

Figure 3.14: Frequency of the three main emission modes of Device B (a) 3.44 THz and (b) 3.36 THz and (c) 3.25 THz as a function of current. Measurements taken at a QCL temperature of 10 K.

3.2.5 4.7-THz QCL fabrication

The 4.7 THz QCL is fabricated from GaAs/AlGaAs materials grown from MBE based on a hybrid design described in [108]. A GaAs buffer layer was deposited onto the 90 µm-GaAs substrate, followed by a $Al_{0.25}Ga_{0.75}As$ etch-stop layer. A 17.2 nm-thick (Si)-doped n^+-GaAs contact layer was deposited with a doping density of 8×10^{16} cm^{-3}. Repeated layers of the active region totalled to a thickness of 12 µm. The device was processed into a Au-Au DM waveguide with a ridge width of 60 µm. The substrate was thinned to a thickness of 88 µm and cleaved to a length of 1200 µm.

Rectangular channels with a cross-sectional area of 170 µm × 40 µm were micro-machined into each Cu block. The two blocks were then joined through alignment dowels to form a rectangular waveguide with a cross-sectional area of 170 µm × 80 µm. Two diagonal feedhorns with an across-diagonal aperture of 1.56 mm × 1.56 mm were precision milled into either end of the waveguide channel with a slant angle of 7.5°. The QCL was solder-mounted into the channel and wire-bonded to the SMA connector.

3.2.6 4.7-THz QCL characterisation

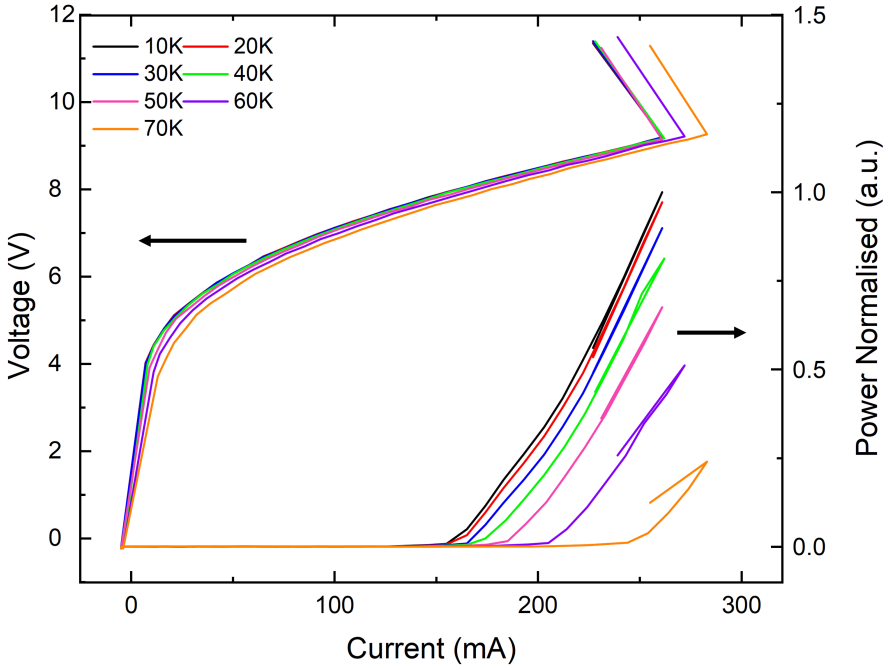

Figure 3.15: LIV curves of the 4.7 THz QCL in pulsed mode between 10–70 K. Current threshold at 10 K is 147 mA.

The LIV curves measured between 10–70 K are given in Figure 3.15. In pulsed mode operation, the current threshold was measured to be 160 mA at a heat-sink temperature of 10 K ($J_{th} = 222\,\mathrm{A\,cm^{-2}}$). Lasing was observed up to a maximum operating temperature of 70 K. In Figure 3.16, the recorded FTIR spectrum is shown. This QCL is multimode with four main emission modes at 4.75 THz, 4.79 THz, 5.00 THz and 5.03 THz.

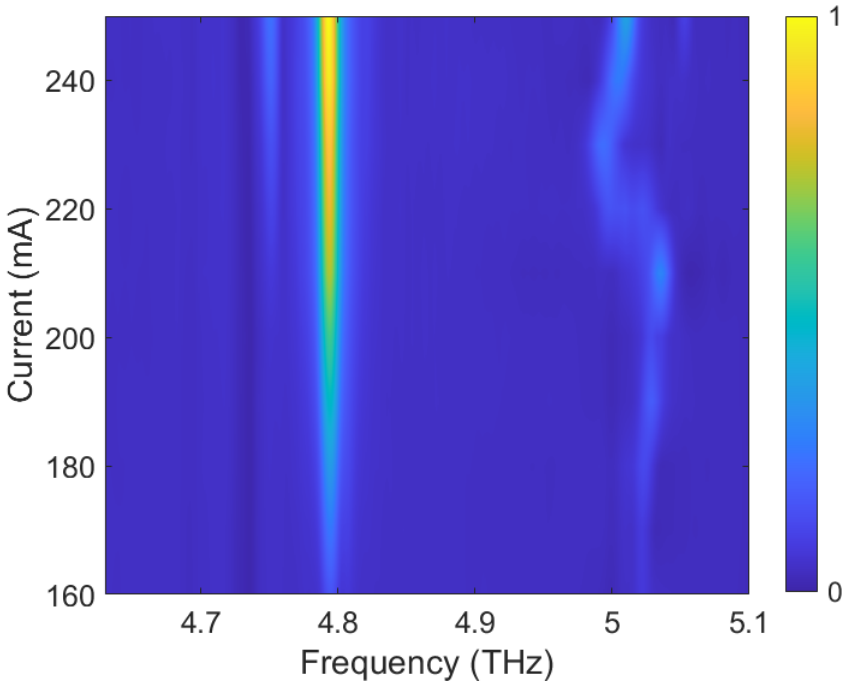

Figure 3.16: FTIR spectrum of the 4.7 THz QCL measured between 150–250 mA at a QCL temperature of 10 K. There are four main emission modes at 4.75 THz, 4.79 THz, 5.00 THz and 5.03 THz.

The output power from the 4.7 THz QCL could not be measured using an absolute THz photoacoustic power meter. The loss in power may be attributed to a high insertion loss caused by a mismatch between the mode profile of the laser cavity and that of the waveguide, and also between the waveguide aperture and free space. This mismatch can induce reflections within the laser, causing a decreasing in output power. In addition, owing to the size of the waveguide channel, the 4.7 THz QCL is extremely overmoded, which causes issues with the beam quality. Ideally, a fundamental WM-47 waveguide would have a width and height of 47 µm and 24 µm respectively [109].

In Figure 3.17, the frequency of the four main emission modes, 4.75 THz, 4.79 THz, 5.00 THz and 5.03 THz as a function of drive current is shown. Over the four modes, a tunability of 30 GHz is obtained. From Figure 3.16 it is shown that the 4.79 THz mode dominates throughout the active current range, with a relative power of 4.1 dB.

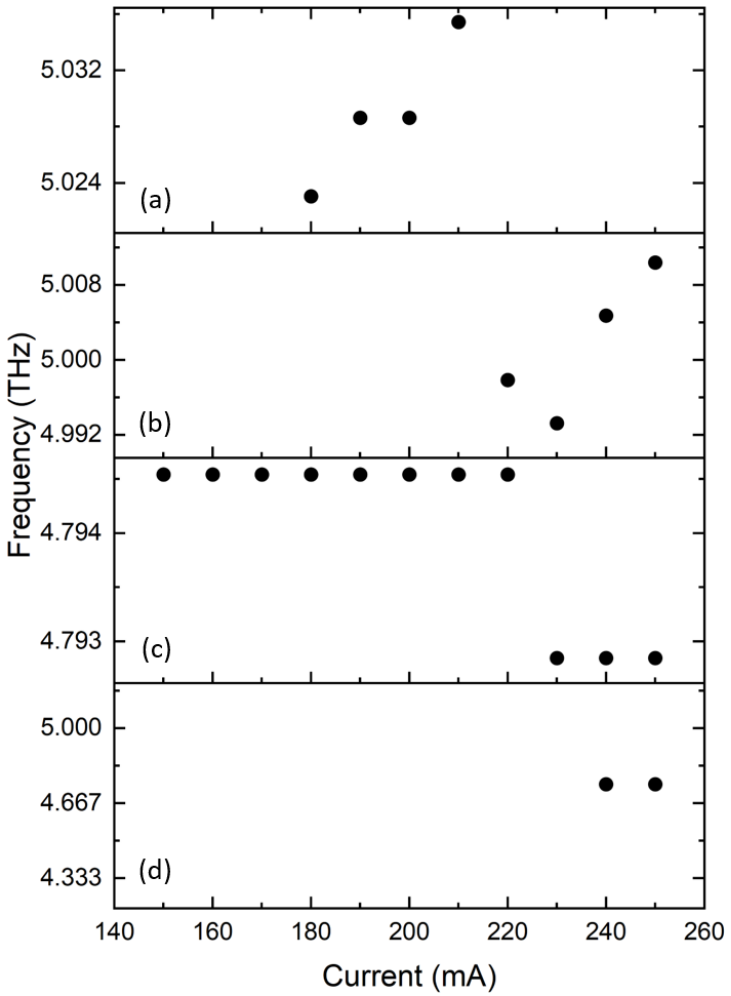

Figure 3.17: Frequency of the four main emission modes of the 4.7 THz QCL, (a) 5.03 THz, (b) 5.00 THz, (c) 4.79 THz and (d) 4.75 THz, as a function of current. Measurements taken at a QCL temperature of 10 K.

3.2.6.1 Thermal analysis

This device did not lase in CW operation, however emission was observed up to a 95 % duty-cycle in continuous pulses at 10 K with a 167 Hz repetition rate. A decrease in power is observed as the duty-cycle is increased (see Figure 3.18). This is a result of internal heating in the QCL, which can be approximated by,

$$T_{AR} = T_{HS} + \gamma I V R_{th} \tag{3.3}$$

where T_{AR} is the temperature of the active region, T_{HS} is the temperature of the heat-sink, γ is the duty-cycle, I is the current, V is the voltage and R_{th} is the thermal resistance [110]. The thermal resistance is an important parameter, which can be inferred experimentally.

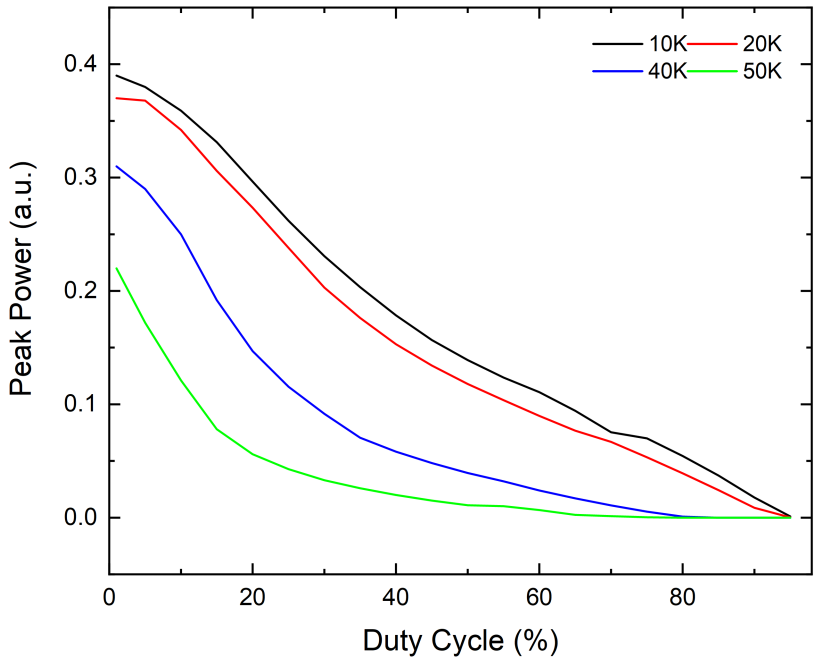

Figure 3.18: Output power of the 4.7 THz QCL as a function of duty cycle between 10–50 K. The QCL operates up to a 95 % duty cycle at a QCL temperature of 10 K.

Taking the peak power recorded in pulsed mode at various temperatures, the thermal resistance of the device can be calculated. Figure 3.19 shows the peak power as a function of heat-sink temperature. Under these short-pulse conditions ($\gamma \approx 0$), $T_{AR} \approx T_{HS}$ and electrical heating is negligible. Note that each point in this figure corresponds to the low duty-cycle values given in Figure 3.18.

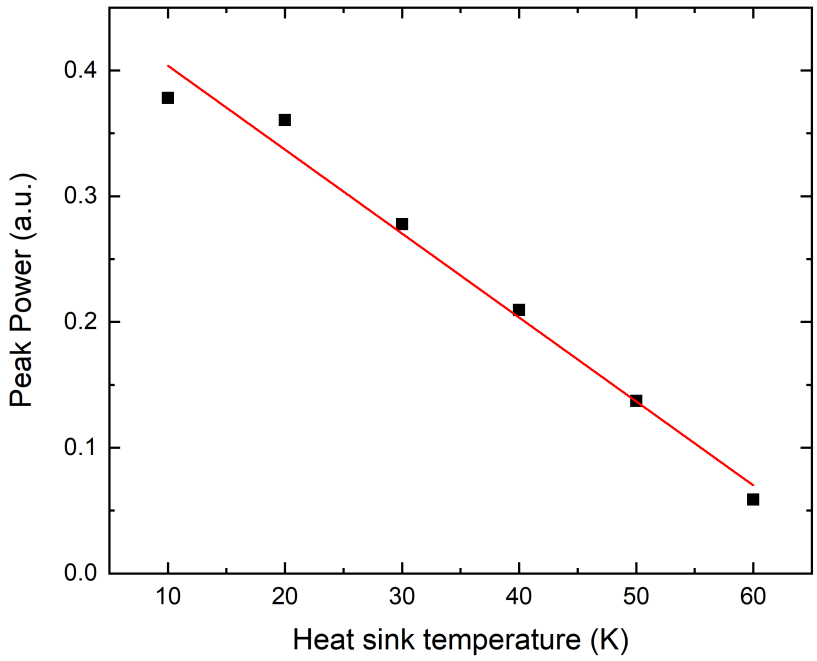

Figure 3.19: Peak power of the 4.7 THz QCL recorded in pulsed mode between 10–60 K.

A linear fit with the expression, $P = 4.75 - 0.06T_{AR}$, therefore relates the internal temperature of the QCL to the peak power, P, recorded as a function of duty-cycle at 10 K. This provides a way of inferring T_{AR} from larger pulsed operation in Figure 3.18. The result as a function of duty-cycle is shown in Figure 3.20, showing $\Delta T = T_{AR} - T_{HS}$.

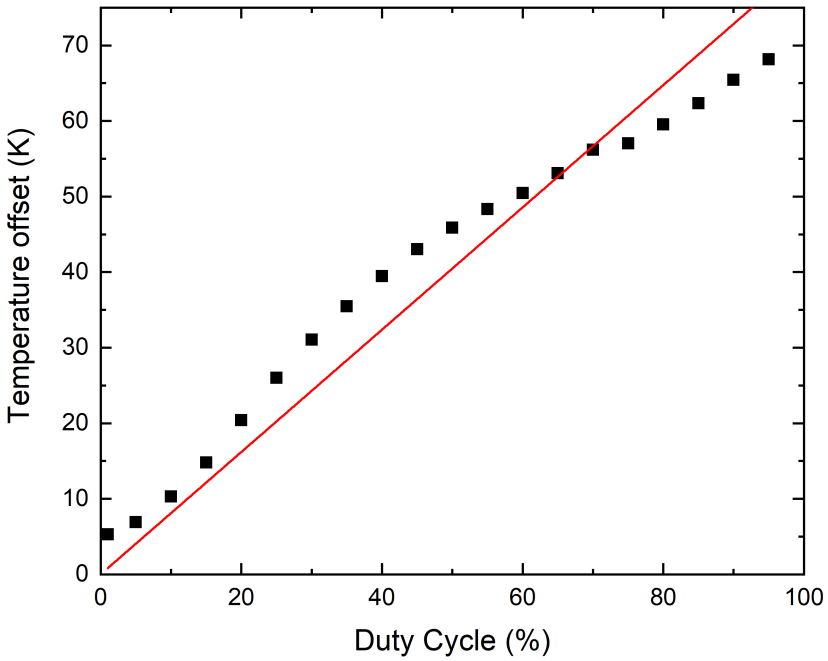

Figure 3.20: Internal temperature of the 4.7 THz QCL from 0–98 % duty cycle.

By applying a proportional fit, the thermal resistance can be calculated from the gradient using the equation,

$$R_{\mathrm{th}} = \left(\frac{\Delta_{\mathrm{T}}}{IV}\right) \times 100 \tag{3.4}$$

The thermal resistance of the device was calculated to be 31 K/W ± 0.9 K/W. Generally, an unmounted QCL would have $R_{th} \approx 8$ K/W [111, 112]. From this value, it is implied that the QCL was unable to operate in CW possibly owing to imperfections in the thermal mounting rather than with the QCL active region or waveguide design. In comparison to Device A and B, which did operate in CW, the 4.7 THz QCL had a narrower waveguide channel. As a result, there is a smaller surface area for the heat to dissipate through.

3.2.6.2 Polarization measurement

For an ideal QCL, the electric field should only be in one plane and hence a QCL is considered to be linearly polarized. This is because the THz emission depends

on intersubband transitions that produce light polarised in the growth direction. However, this is not the case for the integrated device. Once the QCL is confined within a waveguide (discussed in Section 2.4.2), the electric field can to some degree become depolarised through scattering effects. The calculations below determined the amount of ellipticity of the QCL, i.e. how much the electric field deviates out of the linear plane. The polarization of the emitted THz radiation from the front facet of the 4.7 THz QCL was measured using Microtech G50 wire-grid polarizers [113]. These polarizers are considered non-ideal at frequencies above 3 THz, and so measurements taken evaluated the polarization of the QCL as well as the polarizers themselves. Non-ideal polarizers can be characterised through two parameters. With a polarizer set to give minimum transmission, wires are aligned with the electric field polarisation, an electron flux is created and the light is absorbed as it passes through. For a non-ideal polarizer, some light will still leak through, known as the leakage factor (η). Similarly, with the polarizer set to give maximum transmission (wires perpendicular to the electric field polarisation), some light is absorbed, defined as the isotropic power attenuation (μ^2).

To describe the polarization state of a QCL, a Jones vector is used,

$$\psi_0 = \begin{pmatrix} E_{\mathrm{x}} \\ iE_{\mathrm{y}} \end{pmatrix} \tag{3.5}$$

where E_x is the electric field along the major axis and E_y is the electric field along the minor axis.

The ellipticity of the beam, R is defined as $R = E_{\mathrm{x}}/E_{\mathrm{y}}$. Where $R = 1$ for a perfectly circular source and $R = \infty$ for a linear source. For a QCL it is expected that the device is linearly polarised, since transitions occur within only one plane.

In order to measure the polarization, a polarizer was placed in line with the output facet of the QCL and the transmitted power was recorded as a function of rotation angle of the polarizer, results shown in Figure 3.21.

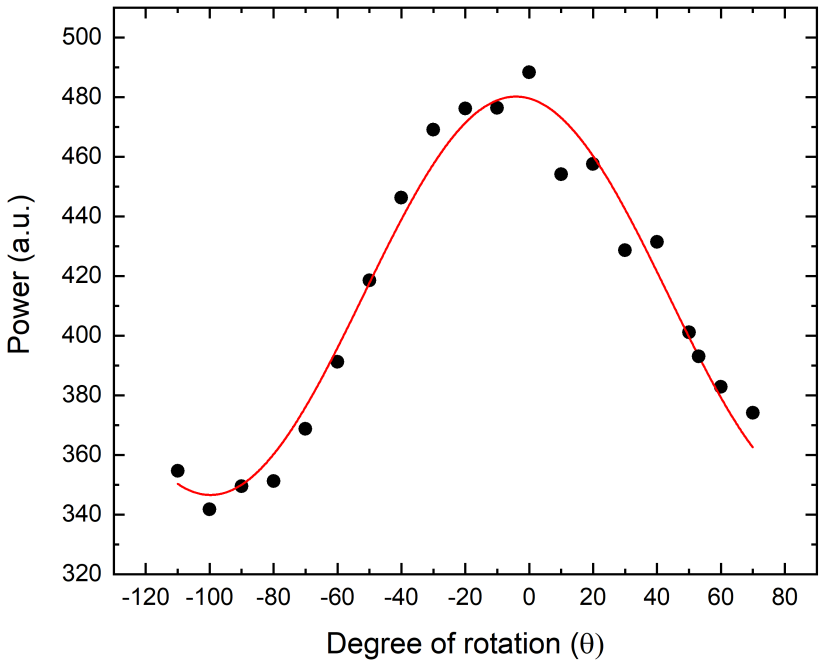

Figure 3.21: Output power from the 4.7 THz QCL transmitted through a polarizer. Red line shows a non-linear fit to the data.

The electric field transmitted through one polarizer at angle θ is given by,

$$\psi_1(\theta) = P(\theta)\psi_0 \tag{3.6}$$

For a perfect polarizer, the Jones matrix is,

$$P(\theta) = \begin{pmatrix} \cos^2\theta & -\cos\theta\sin\theta \\ -\cos\theta\sin\theta & \sin^2\theta \end{pmatrix} \tag{3.7}$$

For a non-ideal polarizer, the isotropic power attenuation (μ^2), and the leakage factor (η) is introduced into the Jones matrix,

$$P(\theta) = \sqrt{\mu}\begin{pmatrix} \cos^2\theta + \eta\sin^2\theta & (\eta-1)\cos\theta\sin\theta \\ (\eta-1)\cos\theta\sin\theta & \sin^2\theta + \eta\cos^2\theta \end{pmatrix} \tag{3.8}$$

where $0 \leq \mu \leq 1$ ($\mu = 1$ for a perfect polarizer) and $0 \leq \eta \leq 1$ ($\eta = 0$ for a perfect polarizer).

This model can be simplified by considering the polarization at 0° (maximum transmission) and 90° (minimum transmission).

$$\psi_1(0°) = P(0°)\psi_0 = \sqrt{\mu}\begin{pmatrix} 1 & 0 \\ 0 & \eta \end{pmatrix}\begin{pmatrix} E_\mathrm{x} \\ E_\mathrm{y} \end{pmatrix} = \sqrt{\mu}\begin{pmatrix} E_\mathrm{x} \\ \eta E_\mathrm{y} \end{pmatrix} \tag{3.9}$$

$$\psi_1(90^\circ) = P(90^\circ)\psi_0 = \sqrt{\mu}\begin{pmatrix}\eta & 0\\ 0 & 1\end{pmatrix}\begin{pmatrix}E_\mathrm{x}\\ E_\mathrm{y}\end{pmatrix} = \sqrt{\mu}\begin{pmatrix}\eta E_\mathrm{x}\\ E_\mathrm{y}\end{pmatrix} \tag{3.10}$$

where the maximum transmitted field after one polarizer is,

$$\psi_1(0^\circ) = P(0^\circ)\psi_0 = E_0\sqrt{\mu}\sqrt{\frac{R^2}{R^2+1}}\begin{pmatrix}1\\ i\frac{\eta}{R}\end{pmatrix} \tag{3.11}$$

The vector-norm of the above equation gives the maximum intensity $I_1(0^\circ)$

$$I_1(0^\circ) = I_0\mu\left(\frac{R^2+\eta^2}{R^2+1}\right) \tag{3.12}$$

The minimum transmission field after one polarizer is given by,

$$\psi_1(90^\circ) = P(90^\circ)\psi_0 = E_0\sqrt{\mu}\sqrt{\frac{R^2}{R^2+1}}\begin{pmatrix}\eta\\ i\frac{1}{R}\end{pmatrix} \tag{3.13}$$

The vector norm gives the minimum intensity $I_1(90^\circ)$,

$$I_1(90^\circ) = I_0\mu\left(\frac{R^2\eta^2+1}{R^2+1}\right) \tag{3.14}$$

A second polarizer was placed behind the first polarizer. The first polarizer (P_1) was angled at ϕ to give maximum transmission, and the transmitted power through the second polarizer (P_2) was recorded as a function of angle θ. The electric field when transmitted through two polarizers is given by,

$$\psi_2(\theta,\phi) = P_1(\phi)P_2(\theta)\psi_0 \tag{3.15}$$

With the first polarizer set to give maximum transmission, the second polarizer is added and fixed to give minimum transmission,

$$\psi_2(0^\circ,90^\circ) = P(90^\circ)P(0^\circ)\psi_0 = E_0\mu\sqrt{\frac{R^2}{R^2+1}}\begin{pmatrix}\eta\\ i\frac{\eta}{R}\end{pmatrix} \tag{3.16}$$

and the intensity transmitted through a pair of cross polarizers, $I_2(0^\circ,90^\circ)$ is,

$$I_2(0^\circ,90^\circ) = I_0\mu^2\eta^2 \tag{3.17}$$

From the above, three equations for the leakage factor η, isotropic power attenuation μ and ellipticity of the source, R, can be derived. By substituting in the following recorded experimentally values, the equations can be solved simultaneously.

$$\begin{aligned} I_0 &= 638.7 \\ I_1(0^\circ) &= 480.17 \\ I_1(90^\circ) &= 346.58 \\ I_2(0^\circ, 90^\circ) &= 223.06 \end{aligned} \tag{3.18}$$

Where I_0 is the detector signal with no polarizers.

The following quartic equation can be solved to give μ,

$$\mu^4 - (\alpha + \beta)\mu^3 + \gamma(\alpha + \beta)\mu - \gamma^2 = 0 \tag{3.19}$$

where α is $I_1(0^\circ)/I_0$, β is $I_1(90^\circ)/I_0$ and γ is $I_2(0^\circ, 90^\circ)/I_0$.

The leakage factor, η is given by,

$$\eta = \frac{\sqrt{\gamma}}{\mu} \tag{3.20}$$

The ellipticity, R is obtained by,

$$R = \sqrt{\frac{\mu\alpha - \gamma}{\mu^2 - \mu\alpha}} \tag{3.21}$$

Using the above equations, μ was calculated to be 92 % and η to be 64 %. The values calculated for μ and η are likely to be reflective of the non-ideality of the polarizers at a frequency above 3 THz. Although these values are not directly recorded in the manufacturers datasheet, it can be extrapolated as having approximately $\mu \approx 94\,\%$ and $\eta \approx 22\,\%$. The transmission factor is close to the expected value. However, the leakage factor is considerably higher. The reason for this is unclear, however possible damage to the polariser may have occured. The ellipticity of the THz beam, R, was measured to be 1.57. This low value implies that the integrated QCL is not a linearly polarized source as a result of depolarisation within the waveguide and feedhorn.

3.3 Beam Profiling

Beam profiles were obtained for each QCL used in this project. This was in order to quantify the beam quality of an integrated QCL in comparison to an unmounted QCL, as well as determine whether the integration method influenced the beam pattern. From these profiles, the angle of divergence, θ, can be calculated using the equation,

$$\theta = 2 \arctan\left(\frac{\mathrm{FWHM}/2}{\mathrm{L}}\right) \tag{3.22}$$

where FWHM is the Full-Width at Half-Maximum (FWHM) and L is the distance from the QCL aperture to the detector. This is a general geometric result that does not assume a particular beam shape.

To profile the beam, a pyroelectric detector was mounted onto a pair of Melles Griot motorised linear stages. The pyroelectric detector had an aperture with an area of 2 mm. This has been accounted for in the angle of divergence error values. No other aperture was used. Profiles were taken in the near-field, far-field and the near-to-far field transition region. In the near-field region the beam profile is of that as the beam first propagates out of the QCL, where the divergence angle is small. For this project, the far-field beam pattern is of more interest, since the gas spectroscopy measurements described in chapters 4 and 5 are taken in the far-field, far from the beam focus where the phase is more ordered.

To calculate the near field limit, known as the Fraunhofer distance, the following equation is used,

$$d = \frac{2D^2}{\lambda} \tag{3.23}$$

where D is the largest dimension of the emission aperture and λ is the wavelength.

3.3.1 Beam profile of device A

The beam pattern of Device A was measured with a 2 mm $\times$ 2 mm step size. The QCL was driven using an Arroyo instruments 4302 LaserSource at a temperature of 10 K at 180 mA with an 85 % duty-cycle.

For the 3.4 THz QCLs, the Fraunhofer distance is 55 mm. In Figure 3.22, the beam profile of device A taken in the near-field (40 mm, 3.22a), near to far-field transition region (50 mm, Figure 3.22b) and far-field (75 mm, Figure 3.22c) are shown. What is observed is a single Gaussian like beam pattern that extends to a dual lobe pattern as the beam transitions into the far-field.

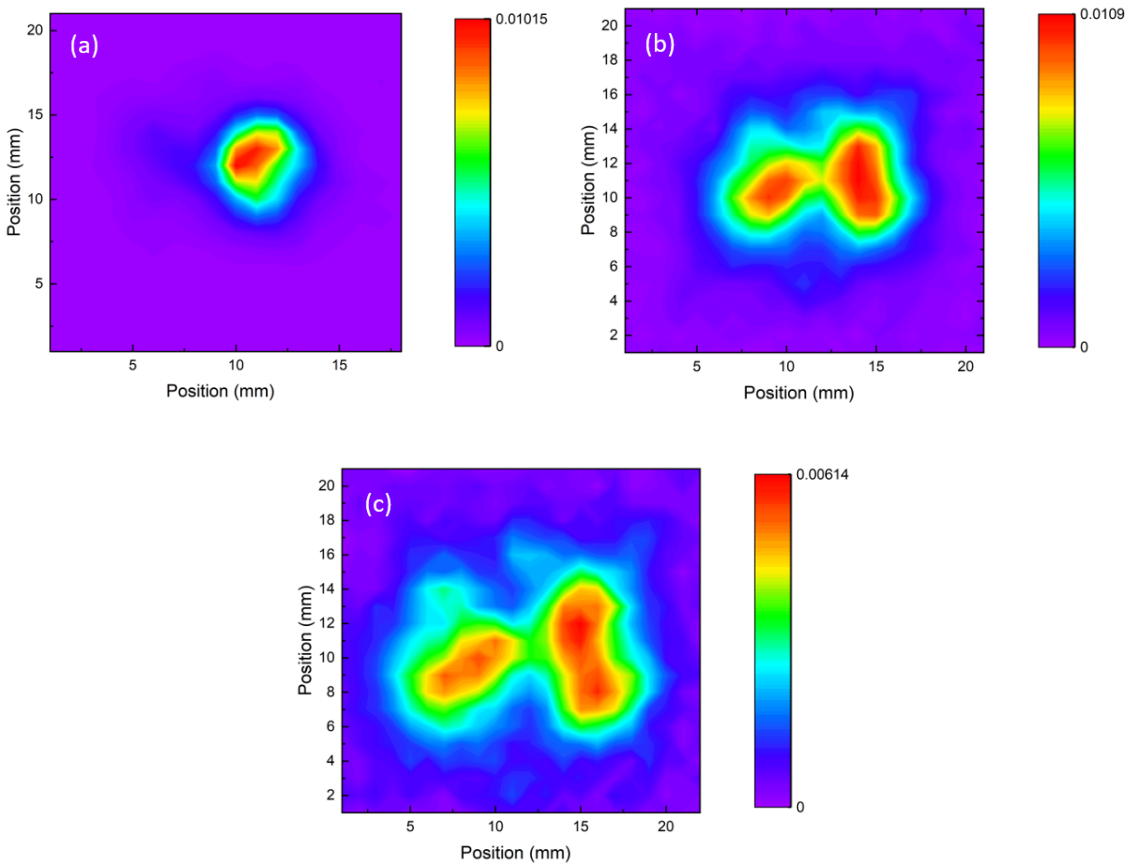

Figure 3.22: Beam profile of Device A at 180 mA. At a distance of (a) 40 mm (b) 50 mm and (c) 75 mm away from the QCL. Measured using a pyroelectric detector.

The angle of divergence for the horizontal and vertical plane was calculated using equation 3.25. The FWHM was taken from a non linear fit of the average horizontal and vertical plane intensity values. The fittings are shown in Figure 3.23.

At 50 mm, the angle of divergence in the horizontal plane is $10.9° \pm 1.1°$ and $7.9° \pm 1.1°$ for the vertical plane. At 75 mm away from the QCL, $10.2° \pm 0.8°$ and $6.5° \pm 0.8°$ were calculated for the horizontal and vertical plane respectively.

Using the following equations [114], an analytical value for a uniform field across a square aperture can be obtained,

$$a = \frac{l}{\sqrt{2}} \tag{3.24}$$

where a is the side length of the QCL aperture and l is the length across the aperture.

$$\theta = \frac{0.88\lambda}{a} \times \frac{180}{\pi} \tag{3.25}$$

where θ is the analytical angle of divergence in degrees and λ is the wavelength of the laser.

From this, a value of 4.1° was calculated. Compared to the measured angle of divergence there is good correlation in the vertical plane. In the horizontal plane, the experimental values are significantly larger than expected. This is attributed to the dual lobe behaviour that is present in the horizontal plane. The Gaussian nonlinear fit extends across two separate peaks (Figures 3.23a and 3.23c) and leads to an artificially large FWHM. Although fitting a double Gaussian (one to each peak) may resolve this problem, it cannot be assumed that the peaks are entirely separate from each other. The equation for a uniform field across a square aperture (equation 3.24) does not account for a dual lobe pattern and therefore a true comparison cannot be made.

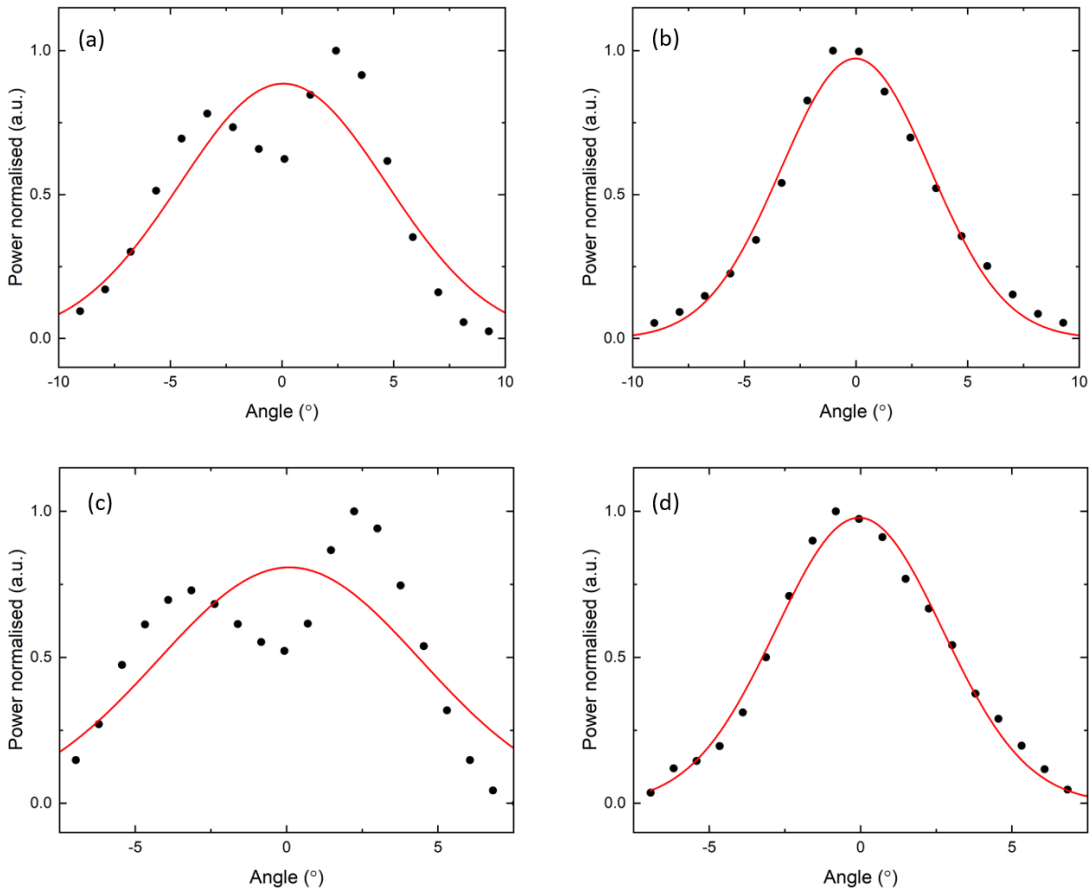

Figure 3.23: Cross-section of the far-field beam profiles of Device A at 50 mm (a,b) and 75 mm using a pyroelectric detector in the horizontal plane (left) and vertical plane (right).

This dual lobe behaviour was observed at all currents and temperatures, and whilst there were small discrepancies in the beam pattern between different days, there is still a clear outline of two lobes above and below the central point of the profile.

There are a number of possibilities to explain the dual lobe pattern. Firstly, there is no back short on the back facet of the QCL, and therefore radiation can be reflected back into the waveguide cavity and cause interference.

Alternatively, with the size of the waveguide channel being larger than the fundamental emission mode of 3.4 THz, multiple transverse electromagnetic (TEM) modes can fit within the waveguide channel and propagate out into free space. The combined near field mode profile is therefore extremely complex. These TEM modes influence the shape of the beam pattern and may well be the source of the dual lobe behaviour. In general, imperfections in the waveguide integration process are possible and can lead to poor beam quality. Another possibility is that the beam pattern may be a result of the interface between the two metallic blocks. After the QCL has been integrated into the waveguide channel, the pair of Cu blocks are combined and secured with alignment dowels that form a diagonal aperture. There is a chance that the radiation dissipates through the split along the diagonal aperture as it propagates through the waveguide channel. The surface current can become split at the interface, resulting in a phase change in the radiated field.

Further analysis was performed to determine how each frequency component of the multimode laser contributes to the overall beam pattern. In order to measure this, beam profiles at a range of currents were taken. The currents were chosen based on the expected modes present from the measured Bruker FTIR spectrum (Figure 3.9). In Figure 3.24, the beam profiles of device A taken at 160 mA, 180 mA and 240 mA are shown. These profiles were taken at a QCL temperature of 10 K at a distance of 70 mm away from the QCL. The QCL was driven in pulsed mode at a 55 % duty-cycle. In all profiles, dual lobe behaviour is exhibited.

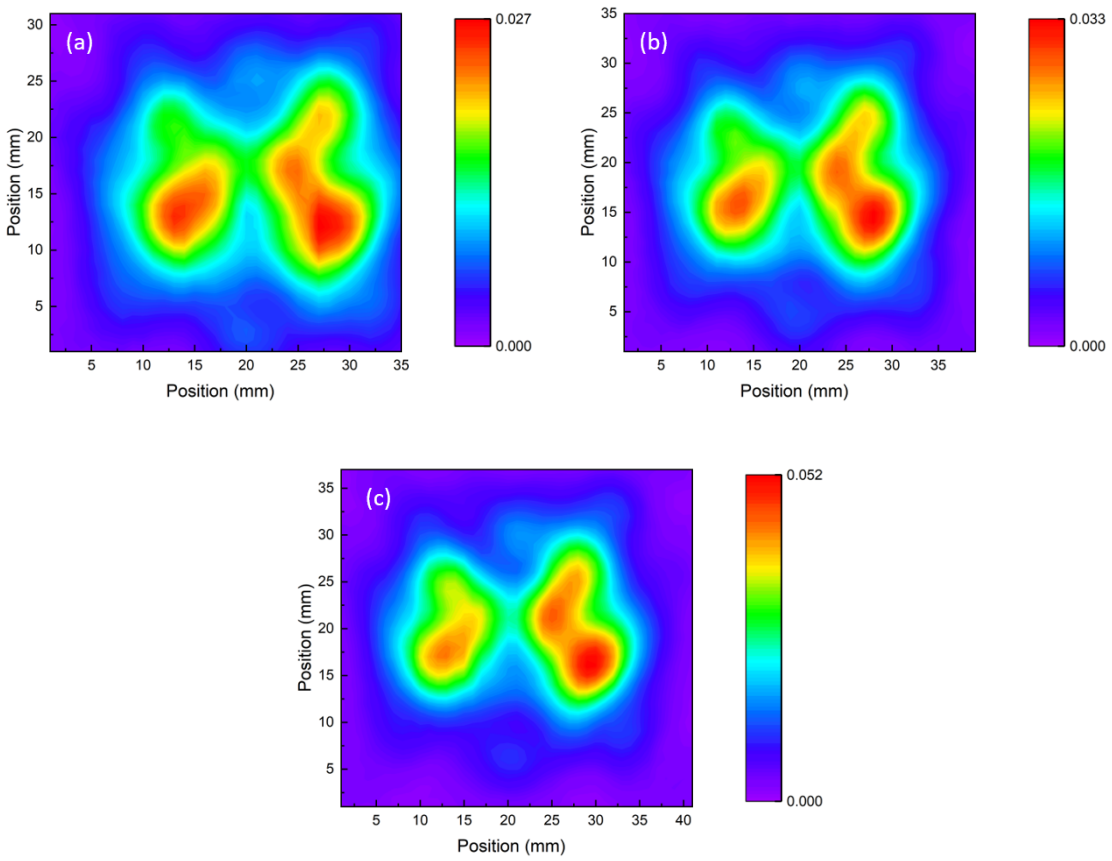

Figure 3.24: Beam profiles of Device A at a distance of 70 mm away from the QCL at a QCL teperature of 10 K. Measured using a pyroelectric detector with the operating current at (a) 160 mA, (b) 180 mA and (c) 240 mA.

The beam profiles in Figure 3.24 are weighted complex sums of the three main modes that appear in Figure 3.9, 3.29 THz, 3.36 THz and 3.42 THz. As such, there are three simultaneous equations that can be solved to determine the area of the beam that comes from each single-frequency component. The equation below is solved for n current beam profiles to give the electric field contribution at each pixel per frequency component,

$$S(n) = |(\sqrt{I_{1(n)}}\tilde{E}_1 + \sqrt{I_{2(n)}}\tilde{E}_2 + \sqrt{I_{3(n)}}\tilde{E}_3)|^2 \tag{3.26}$$

Where S is the intensity of the pixel of the beam profile at n current, I is the measured intensity of the emission mode recorded on the FTIR Bruker system, and $\tilde{E}$ is the complex electric field profile for each frequency.

The equations are solved using the root2d and fsolve function on MATLAB to give the electric field over each frequency at each pixel. An initial estimate of the electric field was determined by taking a sum of the intensity values recorded on the

FTIR Bruker system and dividing by the total modes (3). The electric field values calculated from the solved simultaneous equations are squared to give the intensity values. The output is now 3 plots (Figure 3.25), one for each emission mode, with areas of high intensity highlighting where the specific mode is 'active' in the beam pattern.

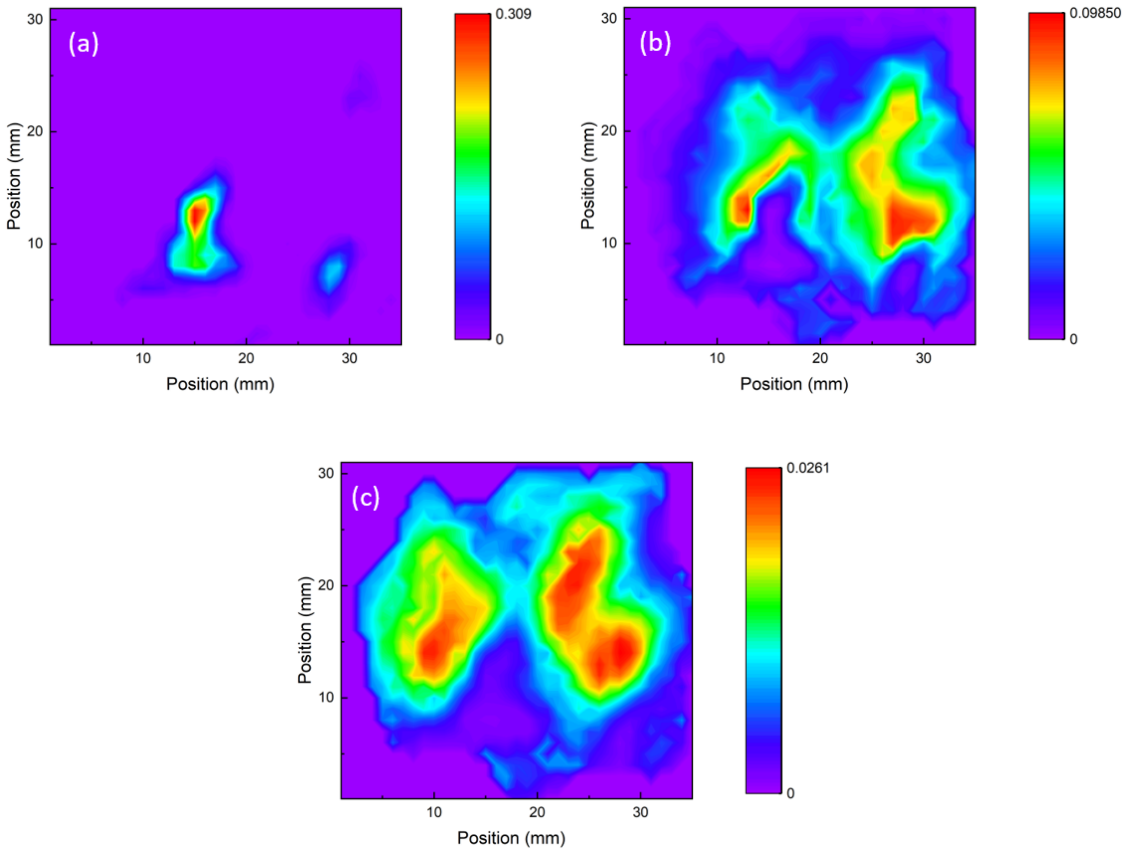

Figure 3.25: Calculate frequency profiles of the (a) 3.29 THz mode (b) 3.36 THz mode and (c) 3.42 THz mode of Device A.

What is deduced from Figure 3.25 is that the specific areas of the profile can be attributed to a specific mode, and that to a certain degree, the modes are spatially separated. The 3.29 THz mode (Figure 3.25a), is active in the lower left region of the bottom lobe which is present in all current profiles from 140 mA given in Figure 3.9. The 3.36 THz and 3.42 THz mode broadly make up the rest of the beam pattern. The 3.42 THz modes in Figure 3.25 has a more intense area in the upper right lobe which is present in the 160 mA, 180 mA, 240 mA plots given in Figure 3.24.

The beam profiles at 120 mA and 140 mA are shown in Figure 3.26. These profiles were taken at 10 K at a distance of 70 mm away from the QCL. The QCL was driven in pulsed mode at a 55 % duty-cycle. Referring to the FTIR spectra in Figure 3.9,

at 120 mA and 140 mA, the 3.42 THz mode is not 'active'. Therefore, it is expected that the upper right lobe is of low intensity. In both plots, the upper right lobe is marked by a black circle and shows low intensity, suggesting that the 3.42 THz mode is not active at these currents.

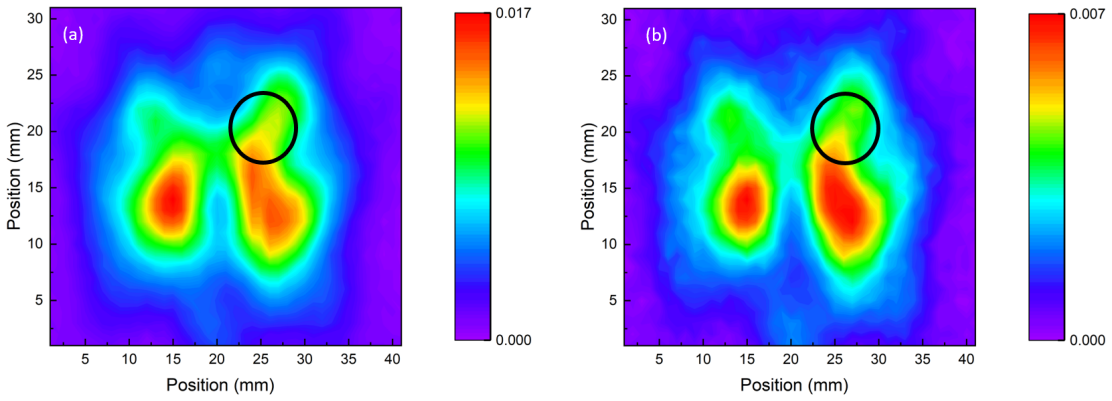

Figure 3.26: Beam profiles of Device A at a distance of 70 mm away from the QCL at a QCL temperature of 10 K. Measured using a pyroelectric detector with the operating current at (a) 120 mA and (b) 140 mA.

3.3.2 Beam profile of Device B

As mentioned previously in Section 3.2, there are small variations in the frequency of the active modes between Device A and Device B. The beam patterns are therefore expected to be slightly different.

The beam was profiled with the QCL operating at 360 mA at 10 K. The device was emitting in pulsed mode at a duty-cycle of 85 %. Figure 3.27 shows the resulting beam profiles at 50 mm (within the near-field), 75 mm and 100 mm (within the far-field) away from the QCL. Similar to device A, the beam pattern is that of a singular lobe in the near field that becomes more dispersed as the distance from the QCL is increased. Within the far-field at 90 mm, multiple lobes of high intensity are present off centre.

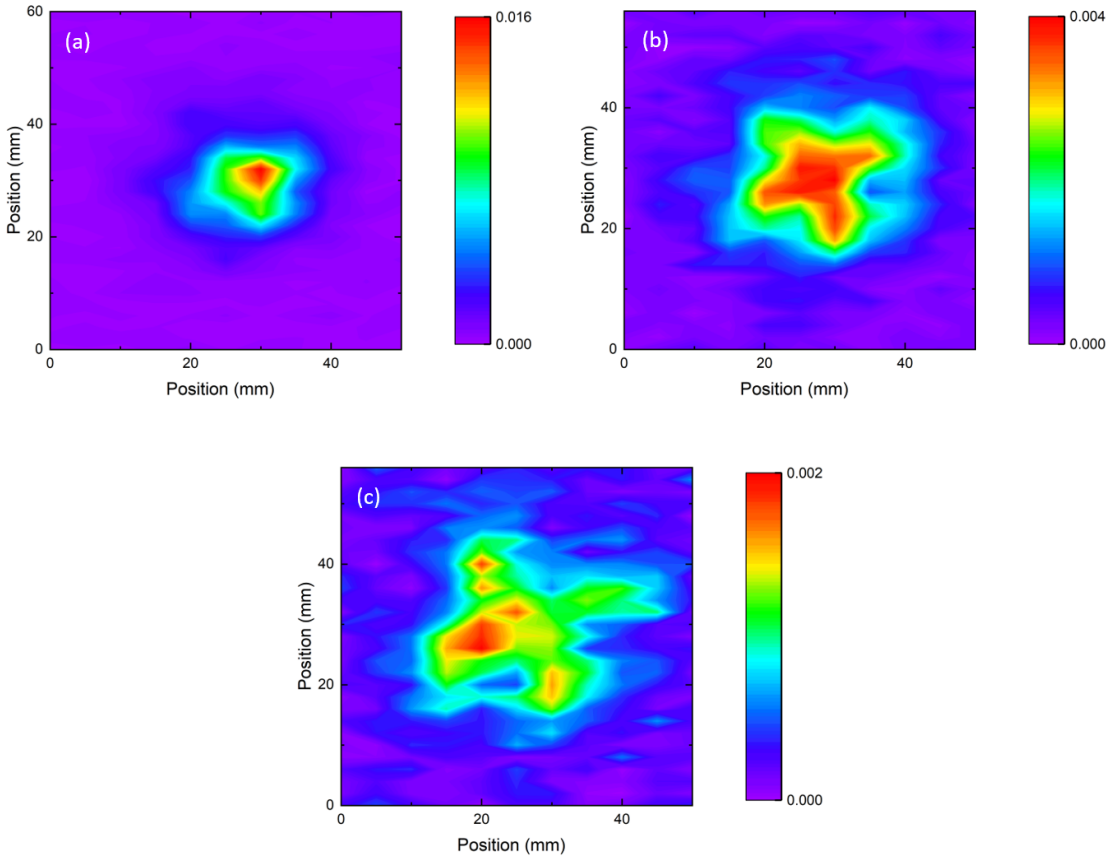

Figure 3.27: Beam profiles of Device B at an operating current of 360 mA. At a distance of (a) 50 mm, (b) 75 mm and (c) 100 mm away from the QCL, with the QCL temperature at 10 K. Measured using a pyroelectric detector.

To calculate the angle of divergence for 75 mm and 100 mm, the FWHM was taken from a nonlinear fit of an average of the horizontal and vertical plane, shown in Figure 3.28. At 75 mm the angle of divergence in the horizontal plane was 17.7° ± 0.8° and in the vertical plane was 16.3° ± 0.8°. For 100 mm, the values of 14.1° ± 0.6° and 15.0° ± 0.6° for the horizontal and vertical plane respectively were calculated. These values are slightly larger than the angles of divergence calculated for Device A. This is because the integration of the QCL into the waveguide channel will always slightly vary between devices. In addition, if the modes are spatially separated as suggested, the beam profile between the two devices is expected to differ as each device has different active modes.

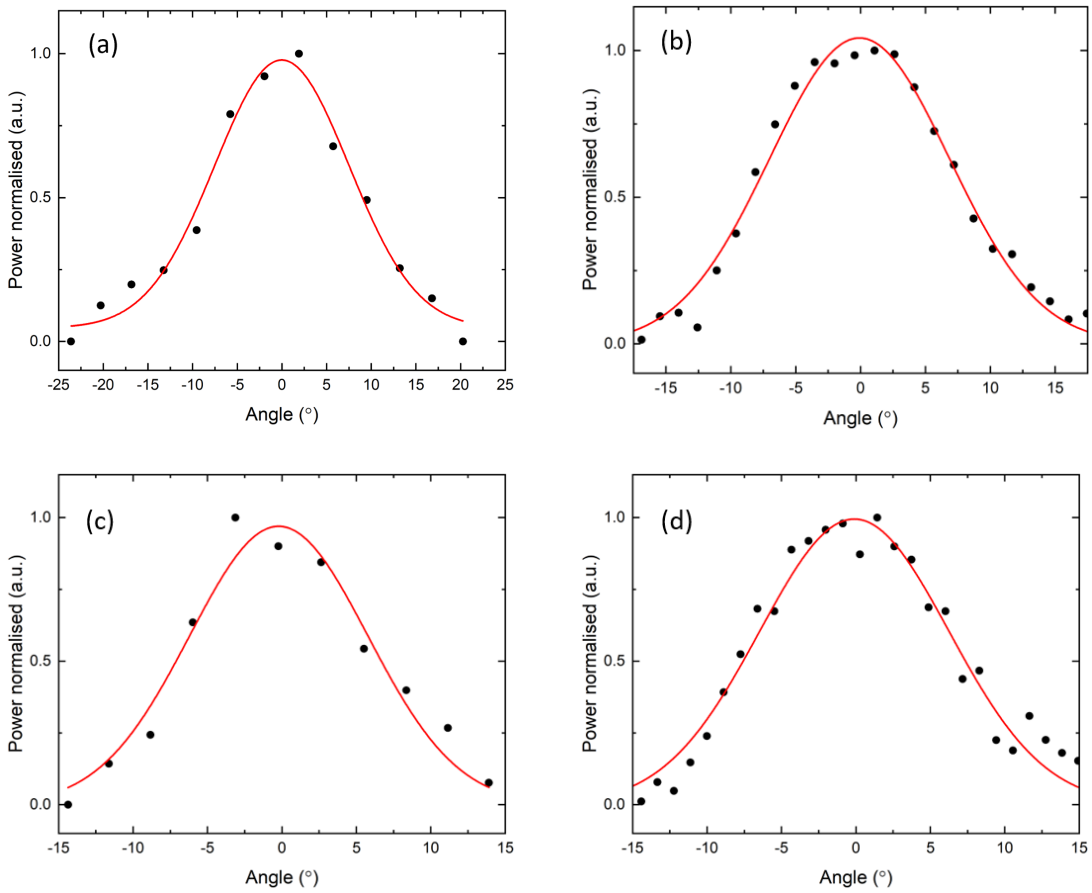

Figure 3.28: Cross-section of the far-field beam profiles of Device B at 75 mm (a,b) and 100 mm (c,d) using a pyroelectric detector in the horizontal plane (left) and vertical plane (right).

3.3.3 Beam profile of 4.7-THz QCL

In order to profile the 4.7 THz QCL, a different approach to the one used for the 3.5 THz devices had to be used. The output power from the divergent beam was too weak to be detected by a pyroelectric detector in the far-field. Instead, a knife edge measurement was taken to determine the FWHM.

The Fraunhofer distance for a 4.7 THz QCL was calculated to be 78 mm. Therefore the knife edge was positioned 110 mm away from the QCL to ensure measurements were taken in the far field. After the knife edge, two parabolic mirrors were position to focus the beam into a liquid He-cooled Si bolometer. The QCL was driven in pulsed mode at a current of 240 mA with a 8 % duty-cycle. The measured heatsink temperature was 10 K and the power was recorded every 1 mm in the vertical and horizontal plane.

Vertical and horizontal knife edge measurements of both the front and back diagonal feedhorn were taken. The results with corresponding nonlinear fits are shown in

Figure 3.29.

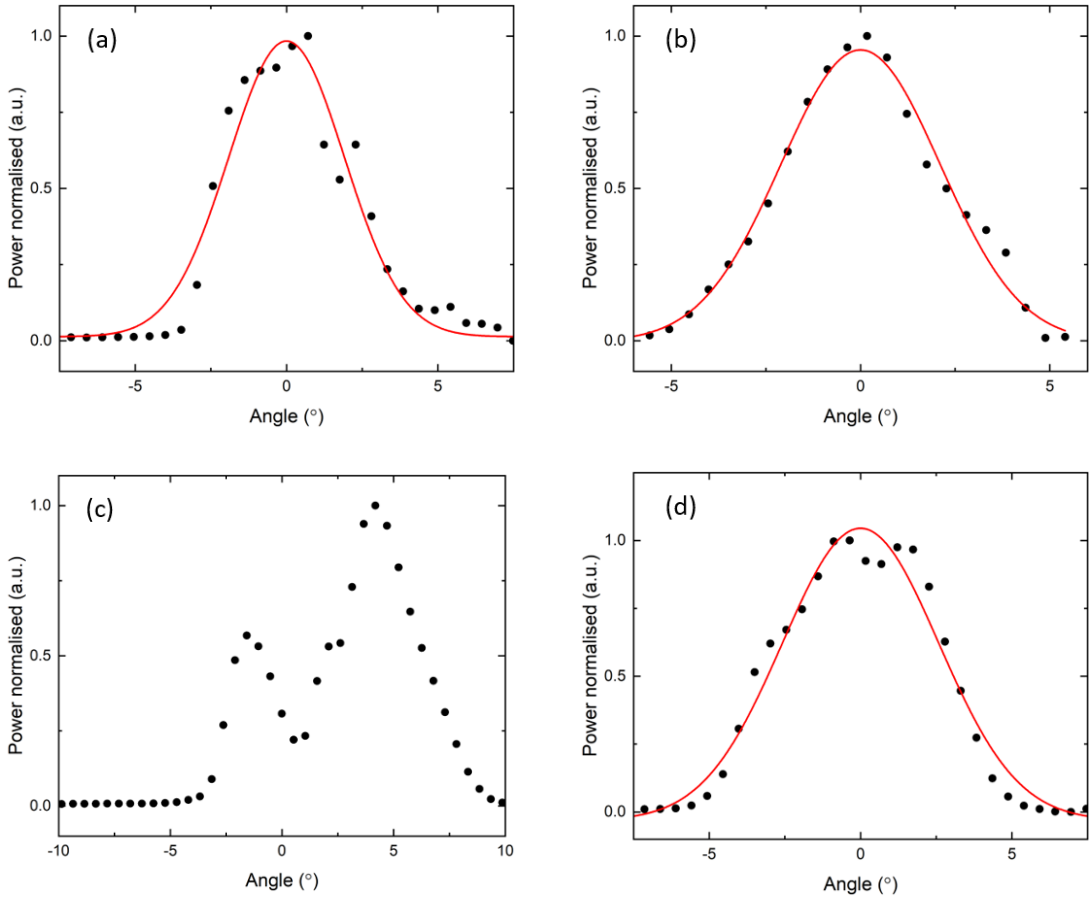

Figure 3.29: Derivative plots of knife-edge measurements of far-field beam profiles of integrated 4.7 THz QCL, for the front facet (a,b) and back facet (c,d) in the perpendicular plane (left) and parallel plane (right) of the waveguide block.

For both the front and back facet, significant dual lobe behaviour was exhibited in the horizontal plane which was more apparent from the back facet.

Calculated using equations 3.24 and 3.25, for a uniform electric field across a square aperture at 4.7 THz, a divergence angle of 2.9° is predicted. As seen in Figure 3.29, the experimental derived horizontal and vertical angle of divergence of the front diagonal feedhorn was 4.4° ± 0.5° and 4.9° ± 0.5° respectively. A value of 6.0° ± 0.5° in the vertical plane of the back diagonal feedhorn was calculated. As seen with both 3.4 THz QCLs, the divergence angle in the horizontal plane cannot be experimentally calculated owing to the beam pattern and the non ideal nonlinear fit to two peaks. These values, aside from the back facet horizontal angle, are generally in good agreement with the analytical value calculated. The angle of divergence for the back facet was larger than that of the front facet. Whilst there is no definitive reason why, it is likely from a combination of experimental error in recording the

distance between the knife edge and QCL and from the integration of the QCL within the laser cavity.

3.4 Conclusion

In this chapter, the THz laser source used in this project was introduced. The QCL integration technique was described and showed to reduce beam divergence and improve beam quality as opposed to an unmounted QCL.

The 3.5 THz and 4.7 THz devices were characterised. What was deduced is that the 3.5 THz devices were a promising choice for gas spectroscopy, offering wide tunability in both CW and pulsed mode. The resulting beam profile patterns were an interesting artefact, however not detrimental in performing gas spectroscopy measurements.

The 4.7 THz QCL failed to work in CW, and coupled with the high thermal resistance, it is unlikely that this device can be used in gas spectroscopy. Further investigation into the fabrication and integration of the device, such as improvements in the solder-mounting and heat-sink design, may well lead to a QCL with the ability to map interesting gaseous species, such as atomic O.

The dual lobe effect appears to increase at higher frequencies, which supports the theory that the effect is due to an artefact of the split-block structure. Variations in the design of the waveguide block could potential resolve this.

Chapter 4

Self-mixing interferometry

In this chapter, the first spectroscopic technique used in this project, SM interferometry is introduced. Firstly, the general principles and underlining theory behind SM is given. This section also contains information of applications that already utilise SM. Then, the experimental setup used is presented along with a description of the scripts used to analyse the data. Lastly, results from the gas spectroscopy measurements of CH_3OH, D_2O and HDO at varying pressures are given.

4.1 Self-mixing

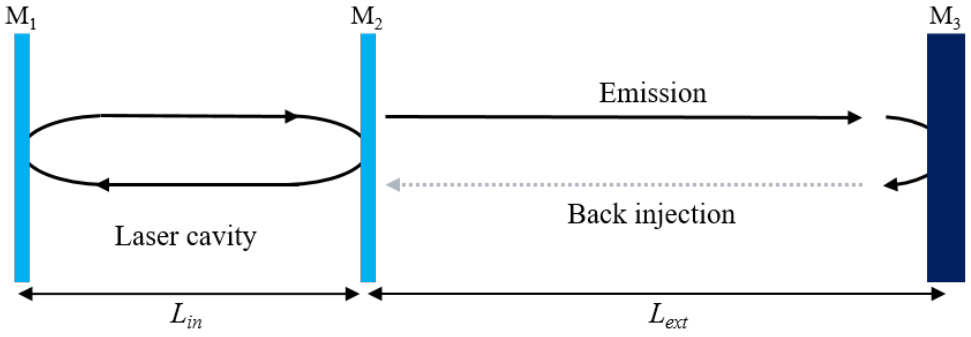

Figure 4.1: Schematic diagram of the SM effect. Light emits from the laser cavity of length L_{in} and transmits through an external cavity of length L_{ext} to a target M_3, and is reflected back through M_2 into the laser cavity. Figure adapted from [115].

The SM phenomenon occurs when a small fraction of a laser's emitted power intentionally re-enters the laser cavity. It is also referred to in literature as induced-modulation [116], injection [117], back scatter modulation [118] or optical/external feedback [119]. The reinjection of light induces a change in the lasing frequency, terminal voltage, threshold gain and emitted power of the laser. These parameters

are all sensitive to both the amplitude and phase of the back-reflected radiation, and as such, the laser can act as a source as well as a coherent detector.

In the majority of applications, optical feedback is undesirable and can lead to an increase in intensity noise [120], coherence collapse [121], and mode hopping [122]. For example, in communications, an optical isolator is typically used to prevent back scattering and amplitude noise [123]. Nevertheless, the SM scheme is highly sensitive, with a response time limited by the lifetime of the lasing state. The measurable perturbations give insight into the external cavity including the complex dielectric properties of the target, all from a minimal, compact optical system.

The effect of SM was first used in order to suppress unwanted modes from a HeNe laser with the addition of a third external reflective mirror by Kleinman and Kisliuk in 1961 [124]. SM was shortly thereafter used in laser metrology, where it was observed using a photosensitive detector that intensity fluctuations occurred as the external cavity length was changed [125]. It was later demonstrated in 1972 that a photodetector is not necessary. Instead, the laser can act as a source, mixer, and detector, with the voltage perturbations across the laser being measured [126]. The SM effect is not restricted to HeNe lasers, and perturbations in the lasing parameters of semiconductor diode lasers [127, 128], interband cascade lasers [129], fiber laser [130], solid state lasers [131] and THz QCLs [132–134] were later realised among many more types. The SM sensing scheme is employed in a vast number of applications and fields. For example, SM is used in metrology [135], material and laser parameters [132], imaging [133] and gas spectroscopy [134, 136].

Despite the fact that many observations of the self mixing effect had been made. It was not until 1980 that Lang and Kobayashi proposed a theoretical model to describe a laser under optical feedback [137]. Here we can assume the Lang-Kobayashi rate equation model under steady-state conditions is equivalent to the three-mirror laser model (see Figure 4.1).

A laser can be assumed to be a Fabry-Perot cavity of length L_{in} with an effective refractive index n_{in} between two mirrors, M_1 with reflectivity R_1 and M_2 with reflectivity R_2. Light can travel through M_2 and emit through an external cavity of a length L_{ext} and effective refractive index n_{ext} to an external target which can be modelled as a third mirror, M_3 with reflectivity R_{ext}. The light is then reflected back into the cavity through M_2.

To characterise the level of feedback there is into the laser cavity from M_3, the

feedback parameter C is used

$$C = \epsilon \frac{\sqrt{R_{\text{ext}}}(1 - R_2)}{\sqrt{R_2}} \frac{L_{\text{ext}}}{L_{\text{in}} n_{\text{in}}} \sqrt{1 + a^2} \tag{4.1}$$

where ϵ is the coupling constant that accounts for optical losses such as attenuation in the external cavity, and α is the linewidth-enhancement factor (LEF) of the laser [138].

Under feedback, the laser frequency shifts. The difference in frequency under steady-state conditions is given by the phase-matching condition [139],

$$(\nu_0 - \nu)\tau_{ext} = C \sin[\nu\tau_{ext} + \arctan(\alpha)] \tag{4.2}$$

in which ν_0 is the unperturbed laser frequency and ν is the laser frequency under feedback. τ_{ext} represents the round-trip delay in the external cavity defined by $\tau_{ext} = 2L_{ext}/c$, where c is the speed of light.

Depending on the phase of the optical feedback, the gain of the laser cavity will increase or decrease. As a result, the laser power P will vary by,

$$P(\tau_{ext}) = P_0[1 + m\cos(\nu\tau_{ext})] \tag{4.3}$$

where P_0 is the unperturbed laser power and m is the amplitude factor, proportional to $\epsilon\sqrt{R_{ext}}$ [140], and the threshold carrier density is given by,

$$n - n_0 = -\tilde{\beta}\cos(2\pi\nu\tau_{ext}) \tag{4.4}$$

where n is the carrier density under feedback, n_0 is the unperturbed carrier density, and $\tilde{\beta}$ is the coupling rate of feedback relative to the rate of the carrier density gain.

The feedback parameter C is important since its value describes the magnitude of the voltage perturbations with respect to the laser frequency under optical feedback. Depending on the level of feedback, there are four different feedback regimes that the laser can be operating in. The strength of the feedback influences the refractive index in the laser cavity, and can lead to self-mixing hysteresis, depicted in Figure 4.2.

- C < 0.1, the *very weak feedback regime*. In this regime, $\nu \approx \nu_0$ and $\cos(\nu\tau_{ext})$ is sinusoidal. The laser is assumed to have the same properties as those in an unperturbed state.
- $0.1 <$ C < 1, the *weak feedback regime*. $\cos(\nu\tau_{ext})$ becomes distorted, shown in Figure 4.2(a).

- $1 < \mathrm{C} < 4.6$, the *moderate feedback regime*. The system is bi-stable, with two stable states and one unstable. The interferometric signal becomes a distorted sinusoidal shape and the laser's properties differ to those in the unperturbed state. Phase hopping may occur due to hysteresis, i.e. in Figure 4.2(b), when the system is in A and ϕ_L (the round-trip phase due to feedback) is increased, the phase jumps down. When the system is in B and ϕ_L is decreased, the phase jumps up.
- $\mathrm{C} > 4.6$, the *strong feedback regime*. $\cos(\nu\tau_{ext})$ becomes very unstable and interferometry measurements are no longer possible owing to multiple phase hopping (Figure 4.2(c)).

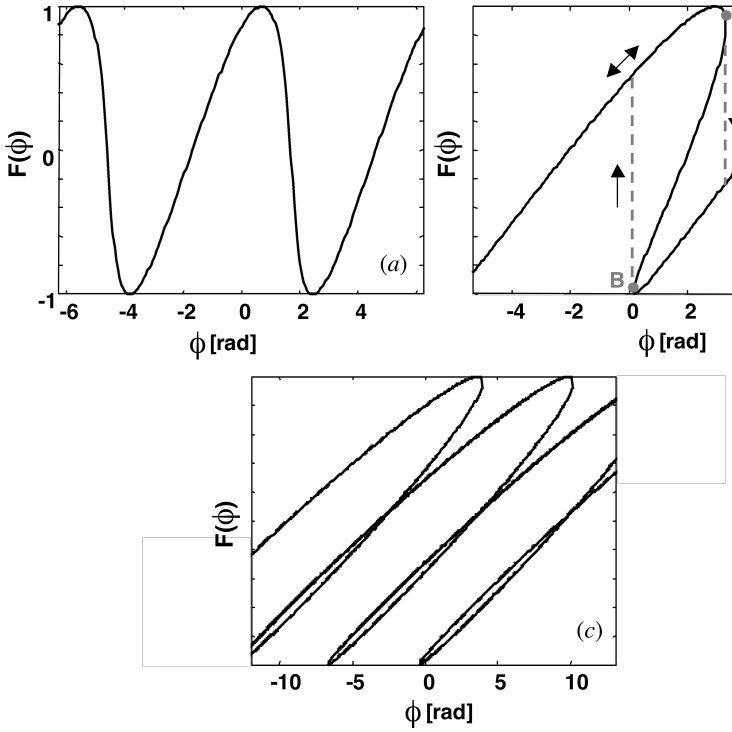

Figure 4.2: Calculated waveforms of V_{SM} for different values of C as a function of ϕ, the phase difference. (a) C = 0.7, (b) C = 3, and (c) C = 10.

With regards to THz QCLs, they operate in the weak feedback regime, ($\mathrm{C} < 1$). The LEF of THz QCLs is typically $\alpha < 1$ [132] as opposed to $\alpha = 2 - 5$ for a regular diode laser [141], owing to transitions being intersubband transitions in the conduction band of the semiconductor. This negligible LEF value coupled with the increased cavity length ($L_{int} \sim 1\,\mathrm{mm}$) than that of a diode laser makes THz QCLs inherently stable under optical feedback. As a result, equation 4.2 can be simplified to,

$$(\nu_0 - \nu)\tau_{ext} = C\sin(\nu\tau_{ext}) \tag{4.5}$$

For the devices used in this project and the setup described in Section 4.2, a value of 9.4×10^{-9} s for τ_{ext} is calculated. Therefore, $\Delta\nu = 17\,\text{MHz}$. Frequency offset is discussed further in Section 4.3.

4.1.1 THz QCL SM applications

Utilising the stable nature of THz QCLs under optical feedback, several potential applications have emerged that make use of the SM effect with a THz QCL.

For example, Green et al. have shown that the LEF of a THz QCL can be measured using SM interferometry [132]. It has also been successfully demonstrated that THz QCLs can be used as SM displacement sensors for round-trip distances up to 21 m in air [142] and at various attenuation levels including through visibly opaque materials up to a distance of 7 m in air [143].

Coherent high resolution imaging has been successfully shown using THz QCL SM interferometry (shown in Figure 4.3). The QCL voltage perturbations are measured across the surface of the sample, from which an image with a depth resolution smaller than the wavelength of the radiation can be acquired. As a result, the surface profile such as contours can be distinguished. Compared to using visible/near-IR radiation, the image is not hindered by sub-micron surface roughness as the longer wavelength of THz radiation makes it less sensitive to defects [133, 144].

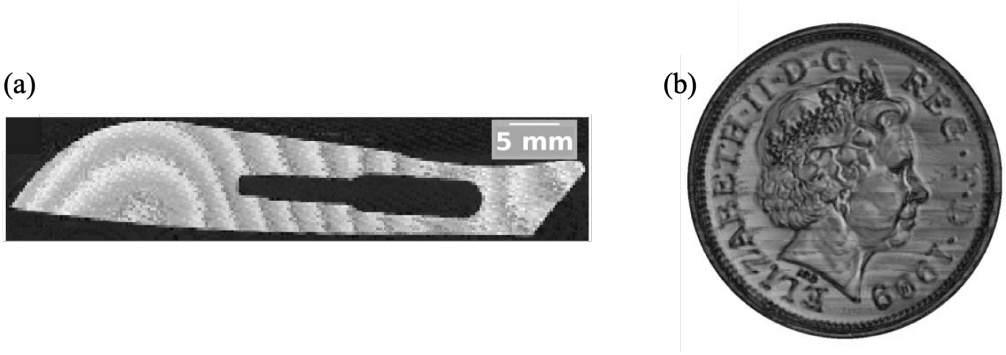

Figure 4.3: Image obtained using SM with a THz QCL of (a) a scalpel blade within a high-density polyethylene FedEx envelope and (b) a British two-pence coin. Figures taken from [133].

THz QCL SM interferometry for gas sensing was first demonstrated by Hagelschuer et al. in 2016 [145], where the absorption spectrum of CH_3OH at 3.3 THz was observed using a single mode SI-SP QCL.

The following work presented in this thesis is a continuation of the work described in [136] and [134]. In the former publication [136], a single mode unmounted QCL was used to measure the spectrum of CH_3OH using SM. In the latter publication,

Han et al. [134] used SM interferometry and 'Device A' (Section 3.2.3), to measure the gas spectrum of CH_3OH at 3.36 THz and 3.42 THz. Some of the results presented in this publication are shown and discussed towards the end of Section 4.3.

4.2 Experimental set-up

The experimental set-up, shown in Figure 4.4, consists of the QCL mounted in a Janis ST-100 He cooled cryostat. The cryostat was first pumped down using a turbo molecular pump to ensuring the low temperature required for the QCL to operate is reached and thermal insulation is maintained. The temperature was monitored using a Lakeshore model 336 temperature controller. An Arroyo 4320 current source was used to drive the QCL. The light emits from the QCL and is collimated using a parabolic mirror before passing through a gas cell of length 965 mm. The light is reflected back along the same optical path using a circular planar mirror and a pair of elliptical planar mirrors in a beam folding arrangement mounted on a Newport ILS-200 mechanically adjustable motion stage with a speed of 100 mm/s, a step size of 1 µm and a maximum distance of 200 mm. This yields a folded round-trip displacement of 800 mm.

Before each measurement, the gas cell was degassed with a mechanical pump and purged with N_2 to ensure there were no gaseous species left in the gas cell that would interfere with the spectroscopic measurement. Attached at each end of the gas cell were a pair of 4 mm thick polymethylpentene (TPX) Brewster's angle windows to prevent etalon effects within the gas cell. The pressure within the gas cell was measured using an AA01A Baratron capacitance manometer. An MKS instruments GM50A mass flow controller was used to control the injection of the gaseous species into the gas cell.

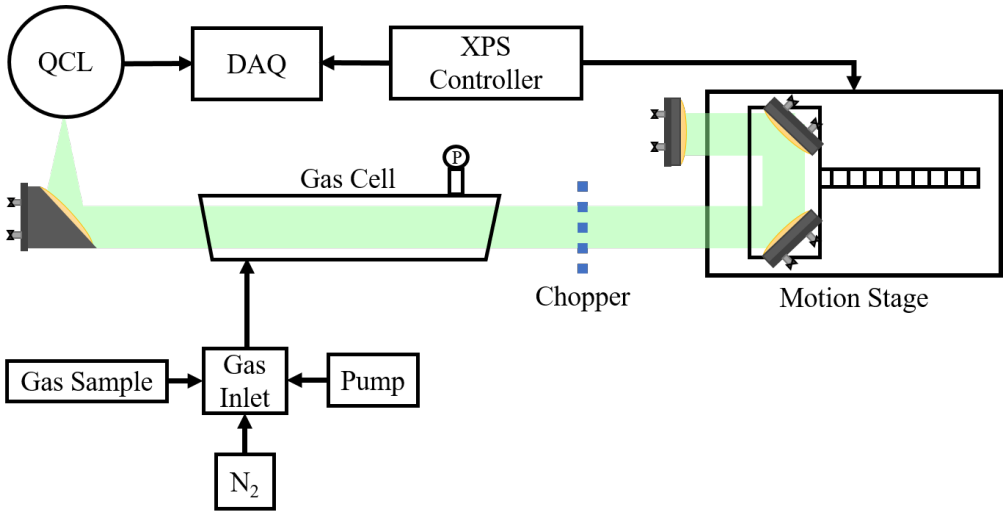

Figure 4.4: Schematic diagram of the SM system used. Light is emitted from the QCL and directed through the gas cell onto a pair of beam folding mirrors before being intentionally reflected back along the path of travel. An XPS controller is used to control the position trigger and the voltage perturbations are recorded using a DAQ board.

A Newport XPS-Q8 motion controller was used to control the position of the beam folding mirrors on the motion stage. The motion controller was configured to generate electronic trigger-output pulses at set intervals, and the voltage perturbations caused by the SM effect were recorded using a National Instruments DAQ board at each point.

Firstly, reference scans were taken. Prior to the measurement, the gas cell was purged with N_2 to reduce absorption by H_2O vapour, down to a base pressure of 4 Pa. During each scan, the driving current was kept constant and the voltage perturbations were recorded as a function of displacement from the motion stage's beam folding mirrors. This produced an interferogram. For each current, a set number of repetitions were taken and averaged to minimise noise. After which, the current was increased by a set increment and scans were taken again. Interferograms were obtained for a defined current range between 110 mA and 240 mA, the currents at which the QCL lases. The whole measurement was repeated again with a gas species present in the gas cell.

An example of the interferograms measured is given in Figure 4.5. The interferograms are more complex than single-mode QCLs owing to the multimode nature of the device. In essence, the interferogram is a superposition of multiple sine waves for each different frequency emitted from the QCL.

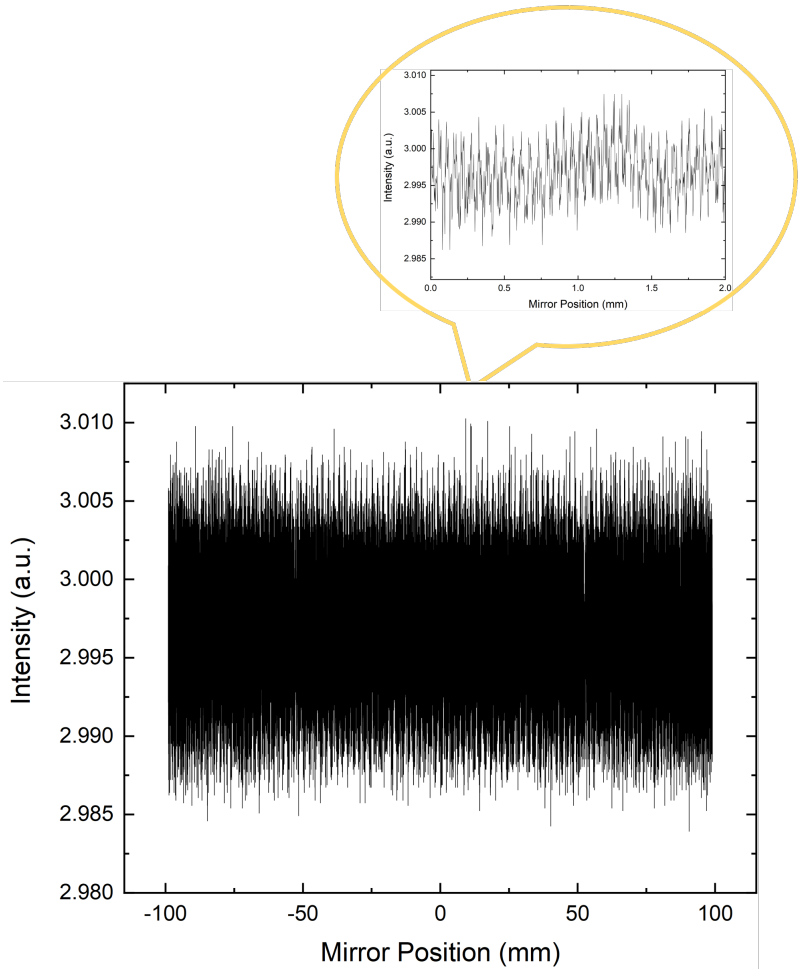

Figure 4.5: Interferogram recorded using the 3.4 THz QCL (Device A).

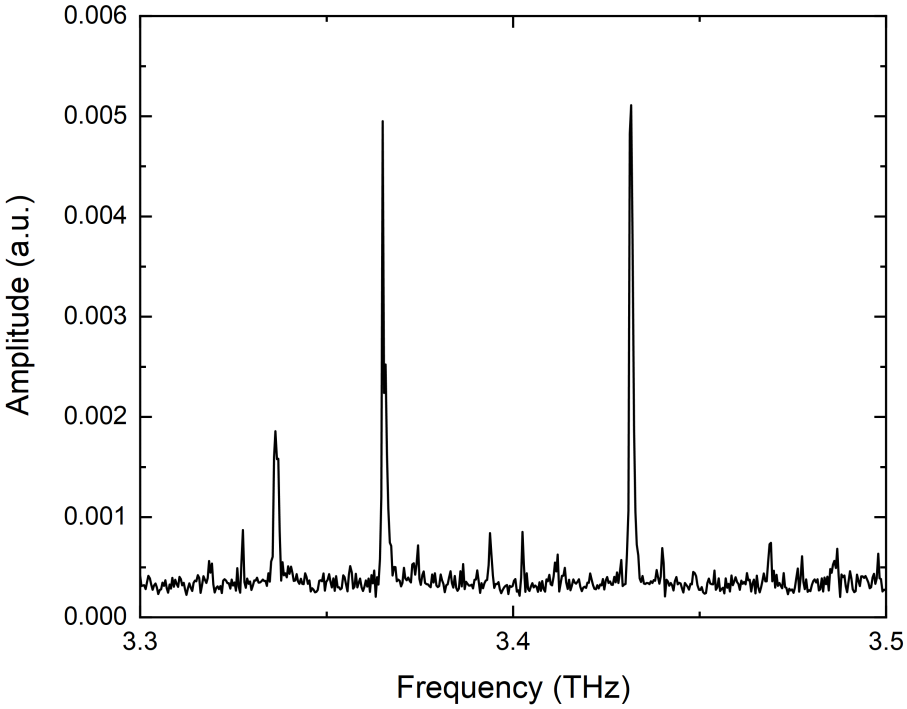

Figure 4.6: Example FFT calculated from the interferogram given in Figure 4.5 using the 3.4 THz QCL (Device A) at 140 mA.

A script developed within the group performed an FFT to each interferogram in order to extract data in the frequency domain. An example FFT is given in Figure 4.6.

After this, a Gaussian fitting algorithm developed within the group was used on each individual FFT in order to extract the Gaussian integral and frequency. Firstly, the user defines approximations for the frequency, height, and width of the specific QCL emission peak of interest. Using the MATLAB function 'MinPeakProminence', the minimum height of a peak is determined to remove potential artificial peaks that arise from noise. Using the 'FindPeaks' function in MATLAB along with the user defined approximations and 'MinPeakProminence' result, the peak height and frequency is found and tabulated. Using 'lsqcurvefit', along with the Gaussian model defined in equation 4.6 and the previous estimations, the centre frequency of the peak and the Gaussian integral (area under the peak) is obtained for both the reference and sample data at each current point.

$$y = a_0 + A \exp\left(-\frac{(f - f_0)}{w}\right)^2 \tag{4.6}$$

where a_0 is the baseline offset, A is the amplitude of the peak, f is the frequency, f_0 is the peak centre, and w is the peak width.

As shown in Figure 4.7, a partial frequency shift was seen between the reference and sample. Typically a change in frequency occurs from a temperature change which can be induced by a change in the current. However, a change in frequency at the same current can arise from the SM effect and the level of optical feedback. As an absorption occurs, the amount of feedback is reduced as the light is absorbed by the gaseous species. Owing to the slight variation in the extracted reference and sample frequency at each current, a 2nd-degree polynomial fit was implemented in order to extract an accurate frequency, given that the lowest polynomial order provided the best fit. For the example given in Figure 4.7, the quadratic polynomial equation is,

$$f = -3.93 \times 10^{-7} I^2 + 1.38 \times 10^{-4} I + 3.35 \tag{4.7}$$

where f is frequency and I is the current.

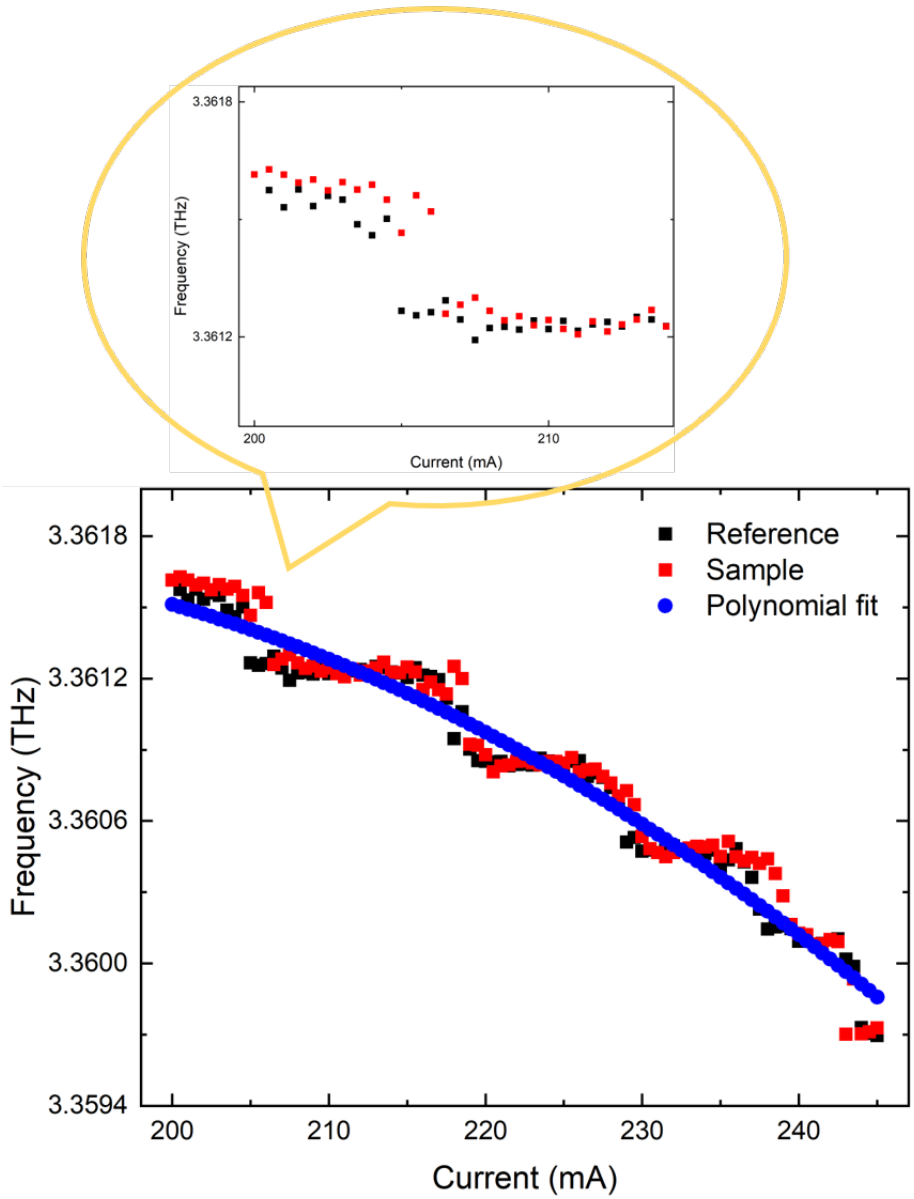

Figure 4.7: Frequency vs current plot for reference (black squares) and sample (red squares). Polynomial fit is shown by the blue circles. Enlarged plot highlighting the step down in frequency as the current is increased, attributed to the FFT sampling resolution.

As the current is increased, the frequency of the laser mode shifts, highlighted in Figure 4.7. The general trend, shown in Figure 4.7 is that as the current is increased, the frequency decreases. The 'steps' that are observed (inset of Figure 4.7), are artefacts of the Fourier transform. The FFT sampling rate was calculated to be 0.375 GHz ($\Delta f = c/D$, c is the speed of light and D is the round-trip delay from the beam-folding optics fixed onto the motion stage, 800 mm).

It must be noted that at certain currents, the sample area under the peak was notably larger than the reference area under the peak at the corresponding current. An example of this is given in Figure 4.8. Here, the area under the peak for the

reference is 5.07×10^{-8}. At the same frequency, the area under the peak for the sample (D_2O) data is 1.32×10^{-7}. As a result, the output is a transmission value greater than 1. This anomaly occurred randomly at different currents on different days and is most likely attributed to power instability issues of the QCL. For the purpose of processing the following data, spectra with and without the anomalies are given. The potential causes of the power fluctuations are discussed in much more detail in chapter 5.

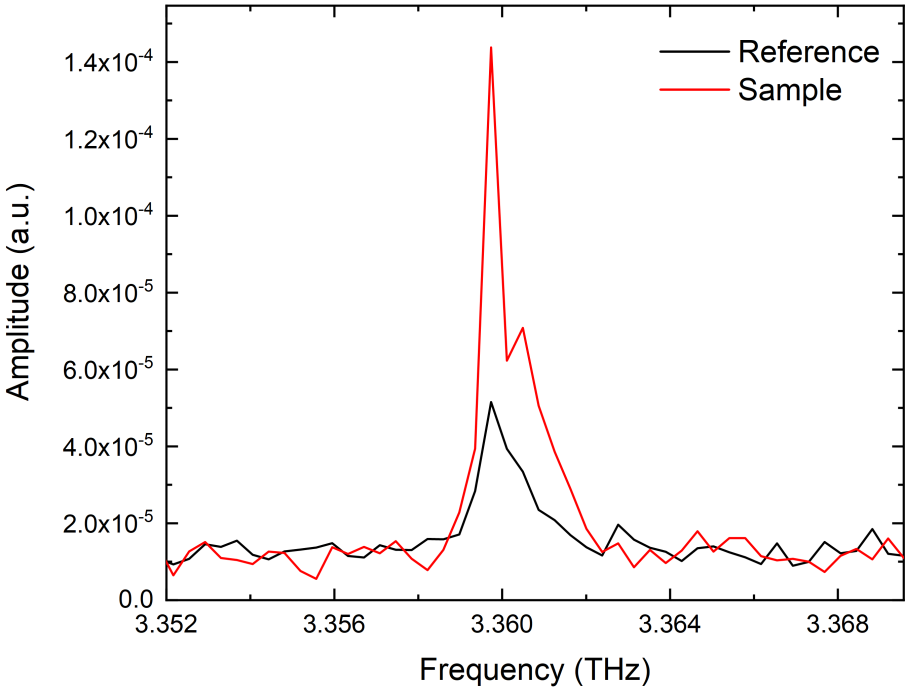

Figure 4.8: FFT spectra of a reference and sample (D_2O), highlighting the uncertain data points recorded during the SM experiments, i.e. the area of the reference peak is smaller than the area of the sample peak at 3.36 THz.

The Gaussian integral is proportional to the power transmission. Thus, by taking a measurement with and without a gas sample present in the gas cell, the difference in transmission can be attributed to an absorption by the gas species in the gas cell. By using the Beer-Lambert law (Equation.1.1), the absorption spectrum can be calculated.

The following numbered list serves as a simplified guide to the data analysis process discussed above that was used to obtain the transmission spectrums given in the following sections.

1. Purge gas cell with N_2.
2. Record interferogram for a given QCL current.
3. Find average interferogram.

4. Take an FFT of each interferogram.
5. Repeat steps 2 –4 with a sample present in the gas cell.
6. Use a Gaussian peak finding algorithm (equation 4.6) to extract the Gaussian integral (area) and centre frequency of the peak of interest at each current for both reference and sample data. Tabulate the approximate frequency vs current.
7. Plot the centre frequency for reference and sample as a function of current (see Figure 4.7 for an example).
8. Apply a polynomial fit to obtain a smooth frequency vs current calibration curve, without Fourier Transform resolution artefacts.
9. Calculate transmission by dividing the reference Gaussian integral by the sample Gaussian integral.
10. Plot transmission vs calibrated frequency to obtain transmission spectrum.

Using the SM gas spectroscopy system and Device A (see Section 3.2.3), a number of gas samples were analysed in order to determine the current sensitivity of the system, as well as to successfully demonstrate the use of SM for gas sensing purposes. CH_3OH (Section 4.3), D_2O (Section 4.4), and D_2O/HDO (Section 4.4.1) were measured at various pressures and compared to simulated data calculated using the NASA Jet Propulsion Laboratory (JPL) spectral line catalogue [40]. The JPL catalogue is a directory compiled by the JPL molecular spectroscopy team at NASA that contains data of submillimetre, millimetre and microwave spectral lines between 0 and 10 000 GHz of a wide variety of atomic and molecular species obtained from literature. In addition, the catalogue provides information on the estimated frequency error, the intensity, the lower state energy and the quantum number assignment.

Using the ideal gas equation, the concentration of the following gases can be calculated from the given pressure,

$$c = \frac{n}{V} = \frac{P}{RT} \tag{4.8}$$

where n is the number of moles, V is the volume, P is the pressure, N_A is Avogadro's constant, R is the gas constant, and T is temperature.

What can be deduced is that as the pressure of the gas species is increased, the concentration, and hence the absorbance, also increases. The specific concentrations can be found in the relevant sections below.

4.3 CH_3OH

The transmission spectrum of CH_3OH was measured at 3 Torr (corresponding to a concentration of 9.9×10^{16} molecules cm^{-3}). Measurements were taken between 110 mA and 140 mA with a step size of 0.2 mA at a QCL temperature of 10 K and a gas temperature of 298 K. The reference data was taken with the gas cell under vacuum. For this QCL, two main emission modes are expected at 3.36 THz and 3.42 THz, as measured and illustrated in Figure 3.9. Referring to the JPL catalogue, absorption by CH_3OH is expected at both of these frequencies and therefore fitting was done to both modes to extract two separate transmission spectra.

Fitting was first done to the 3.36 THz mode. This mode is present from 113 mA (see Figure 3.9) and therefore measurements were taken from 113–140 mA. The output frequency as a function of current is given in Figure 4.9. The mode shifts by 5 GHz, from 3.363 THz to 3.368 THz as the current is increased.

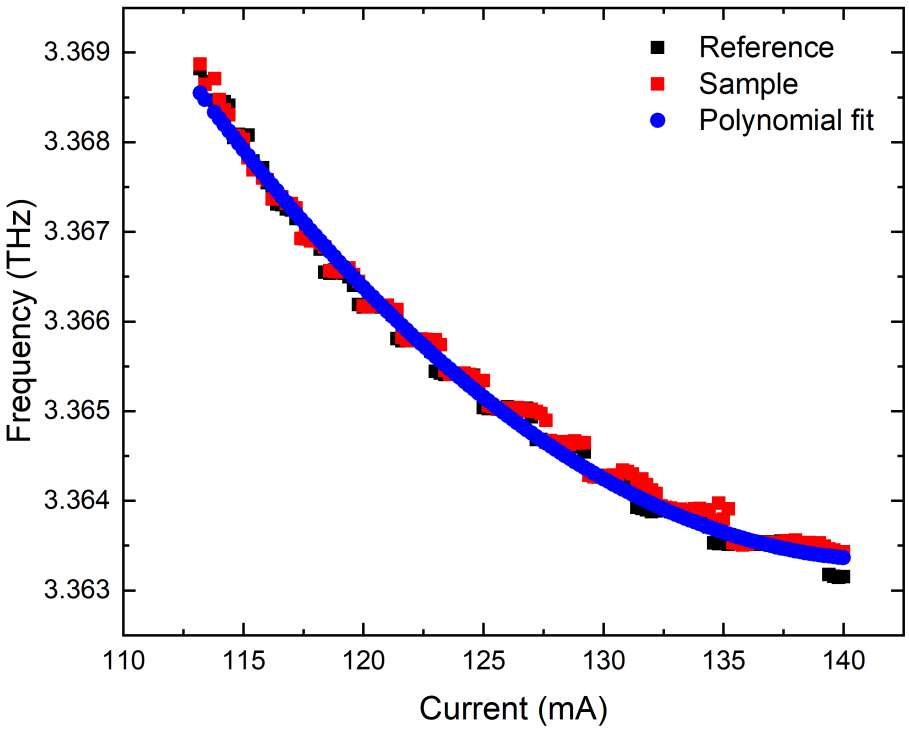

Figure 4.9: Frequency vs current plot for CH_3OH at 3 Torr at a frequency of 3.36 THz. Blue circles highlight the 2nd-degree polynomial fit done in order to extract the frequency.

The measured transmission spectrum is given in Figure 4.10 including all data points.

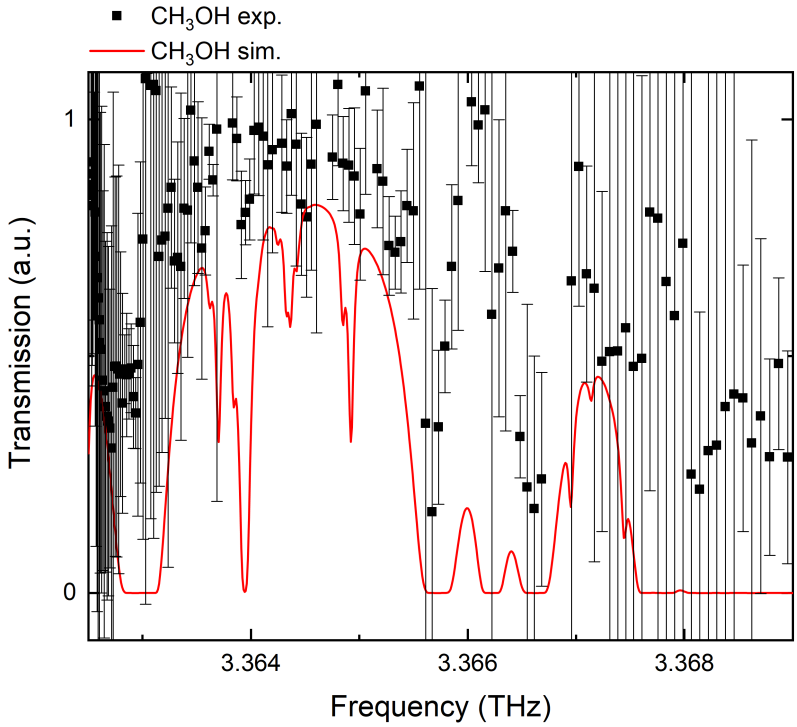

Figure 4.10: Transmission spectrum of CH_3OH at a frequency of 3.36 THz and a QCL temperature of 10 K. Gas pressure was 3 Torr and the gas temperature was 298 K. The spectrum includes all data points. Transmission values > 1 are observed. Simulated data taken from the JPL catalogue are shown by the red line.

A frequency offset between the simulated and experimental data of approximately 0.7 GHz (a 0.02 % offset of the 3.36 THz peak) was observed between the simulated and experimental data. A number of reasons are likely to be the cause of this offset. Firstly, a calibration offset in the motion controller that was noted previously by Han et al. from the same SM system [134]. Additionally, Keeley et al. [146], reported on a frequency offset of ~ 750 MHz, caused by the SM effect for a QCL at 2.25 THz. Note that this value is larger than the value calculated in Section 4.1. This is because the length of the cavity, L_{ext} in this project was longer, and hence τ_{ext} is bigger. Under optical feedback (OF), described by Lang and Kobayashi [137], the change in the intracavity amplitude from OF induces perturbations in the carrier density which in turn causes the frequency to shift (see equations 4.2, 4.3 and 4.4). As mentioned in Section 4.1, the work of Lang and Kobayashi is restricted to single mode operation. However, when C is in the weak feedback regime ($C = 0.1 - 1$, as in this case), the resultant interferogram can be described as a linear combination of signals from individual modes of the laser, i.e. multiple single mode lasers. Lastly, a $\cos\theta$ error caused by the motion stage not being straight along the table can also give rise to a frequency shift. The larger θ is, the smaller $\Delta z \cos\theta$ becomes (where Δz is the step size of the stage). This leads to an underestimation of the true frequency. In this

case, the measured frequency was larger than the expected frequency, and therefore a $\cos\theta$ error cannot be the cause of the frequency offset. A culmination of the frequency offset caused by the SM effect, $\Delta\nu = 17\,\text{MHz}$, as well as the calibration offset is likely to amount to the 0.7 GHz frequency offset seen. For all following gas spectra, please note that a fixed frequency shift of 0.7 GHz has been corrected for.

The error bars were calculated from applying the following equation to both the reference and sample data,

$$\text{Relative error} = \frac{std_{(I)}}{avg_{(I)}} \tag{4.9}$$

where *std* is the standard deviation at each current and *avg* is the average at each current.

The real error at each current was calculated from,

$$\text{Real error}_{(I)} = \sqrt{((\text{Reference relative error}^2_{(I)}) + (\text{Sample relative error}^2_{(I)})} \tag{4.10}$$

Finally the transmission error at each current point is given by,

$$\text{Transmission error}_{(I)} = \text{Transmission}_{(I)} \times \text{Real error}_{(I)} \tag{4.11}$$

What is observed is at certain currents, the transmission value is > 1. This is a result of the area under the sample 3.36 THz mode being larger than that of the corresponding reference mode as mentioned in the previous section, which causes large error bars. This phenomenon is most likely due to the QCL having power instability issues. However, it could also be as a result of the complex form of the SM signals, which are susceptible to scattering in the feedhorn and external vibration. The data points at currents where this phenomenon occurs have been removed. The resulting transmission spectrum is shown in Figure 4.11.

From Figure 4.11, a number of peaks can be identified and align well with the simulated peaks provided by JPL. Specifically, gas lines at 3.3628 THz, 3.3657 THz and 3.3666 THz can be seen. Unlike the simulated data, the experimental data does not reach saturation. In addition, some gas lines do not appear to be present, e.g. at 3.364 THz a sharp gas line that reaches saturation is expected. It is unclear why this has occurred.

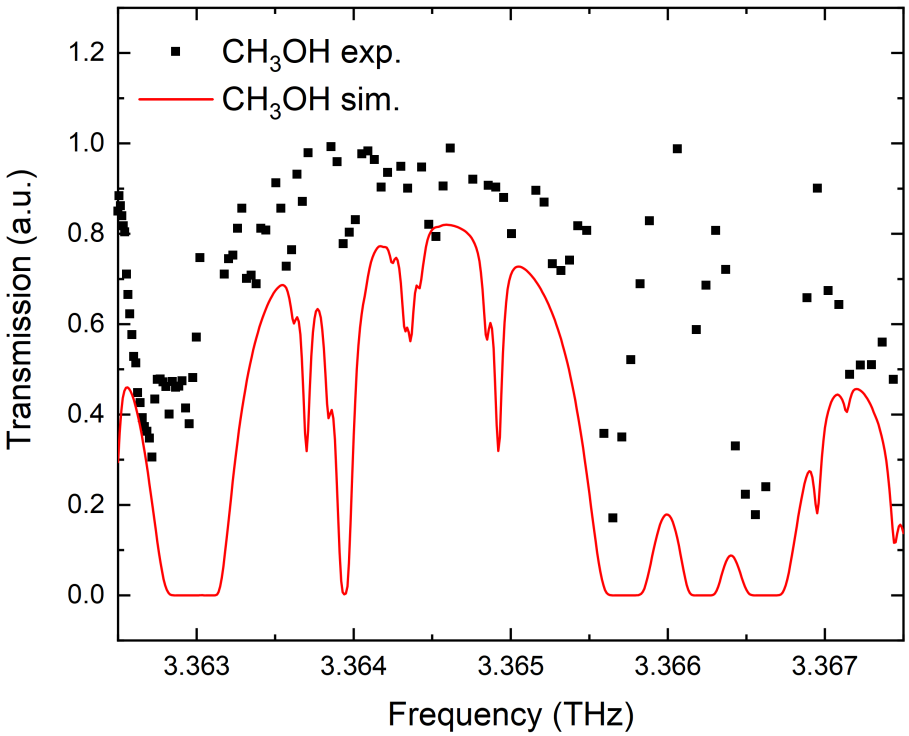

Figure 4.11: Transmission spectrum of CH_3OH at a frequency of 3.36 THz and a QCL temperature of 10 K. Gas pressure was 3 Torr and the gas temperature was 298 K. The spectrum excludes data points where the sample area is larger than that of the reference. Simulated data obtained from JPL catalogue are shown by the red line.

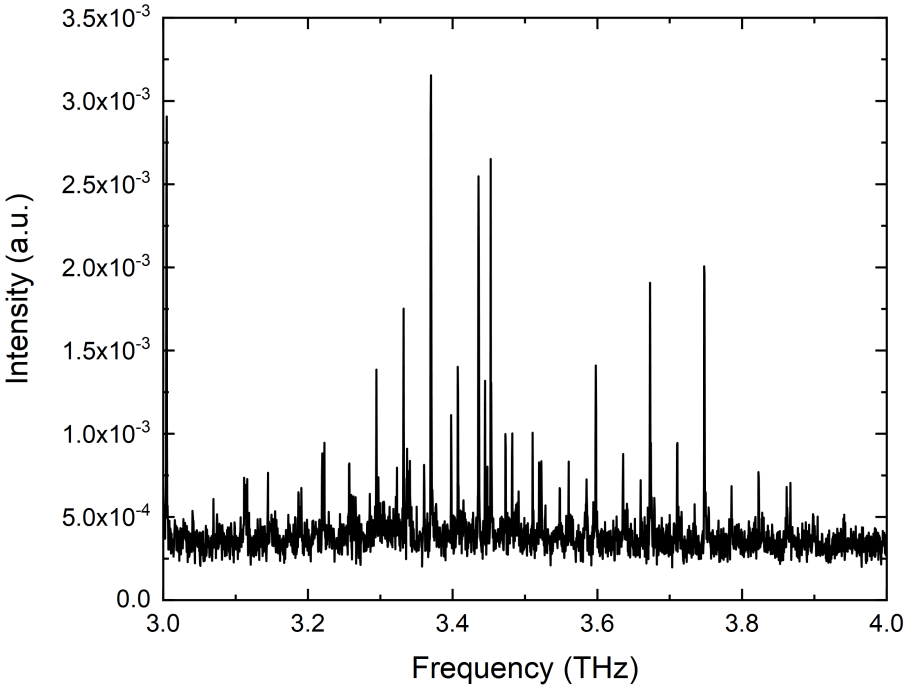

Figure 4.12: Reference FFT spectrum taken at 110 mA at a QCL temperature of 10 K. Multiple peaks are exhibited around 3.4 THz.

Interestingly, between the range of 110 mA and 120 mA, the FFT spectrum exhibited

multiple modes around 3.4 THz (see Figure 4.12 for an example). The noise standard deviation was calculated to be 5.42×10^{-5}, with the minimum peak prominence calculated to be 4.99×10^{-4}, ($M_0 + 3 \times \sigma$, where M_0 is the mean of the baseline and σ is the standard deviation of the baseline). From this value, it is inferred that any of the peaks around 3.4 THz could be the unperturbed laser emission mode. The origin of the additional peaks is unclear. One potential cause could be electrical noise that has been modulated onto the QCL cabling, or the additional peaks could be a result of the QCL not being integrated into a fundamental waveguide (see Section 3.3.1). However, this cannot be confirmed. Therefore, it was decided fitting to the 3.42 THz peak would be implemented only using the data from 120–140 mA. The frequency output of the fit is given in Figure 4.13. As the current is increased, the mode shifts in frequency by 3 GHz between 3.432 THz and 3.429 THz.

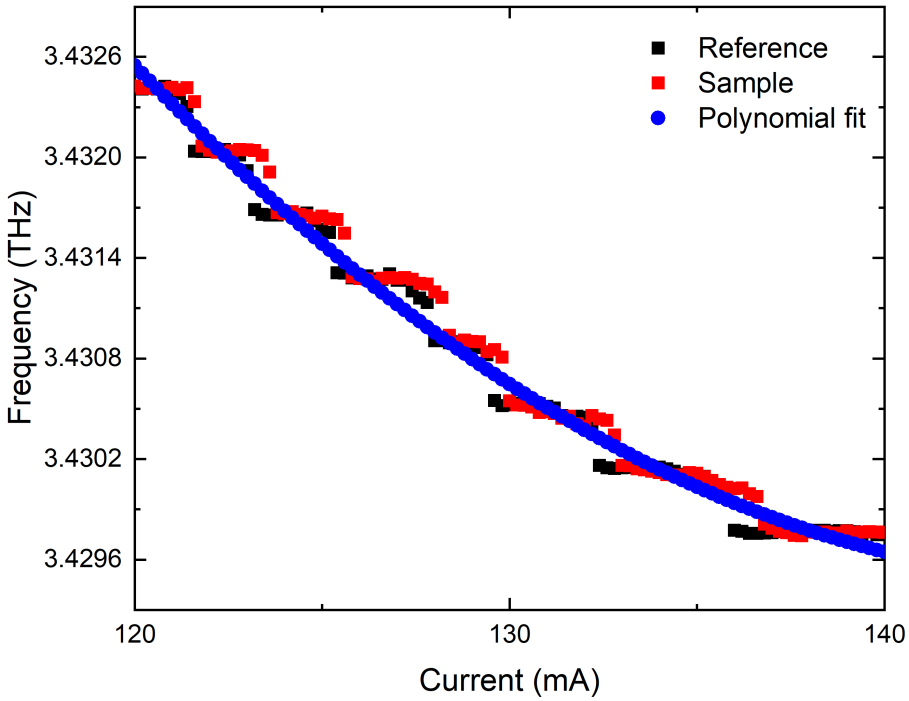

Figure 4.13: Frequency vs current plot for CH_3OH at 3 Torr at a frequency of 3.42 THz. Blue circles highlight the polynomial fit done in order to extract the frequency.

The resulting transmission spectrum including all data points is given in Figure 4.14. In this case, the error bars are particularly large. The experimental data points at the simulated peaks, 3.4305 THz, 3.4310 THz and 3.4312 THz do exhibit smaller than average error bars, indicative of them being associated with an absorption line. However the error is still too large to be certain in the fact since transmission values > 1 are common, and whilst the frequency offset has been compensated for, the experimental data differs greatly from the simulated data in intensity.

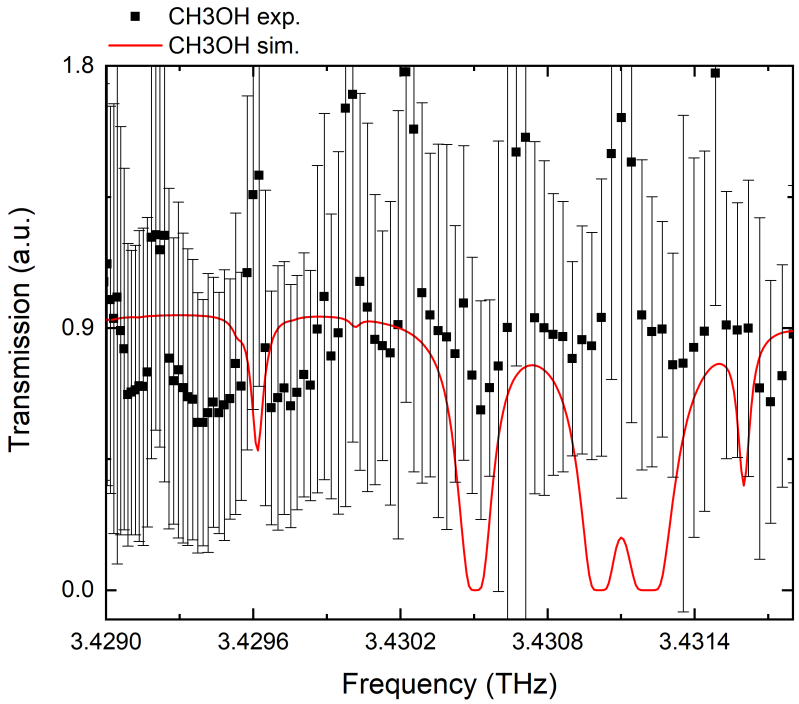

Figure 4.14: Transmission spectrum of CH_3OH taken at a frequency of 3.42 THz and a QCL temperature of 10 K. Gas pressure of 3 Torr and a gas temperature of 298 K. Spectrum includes all data points. Transmission values > 1 is observed. Simulated data taken from the JPL catalogue are shown by the red line.

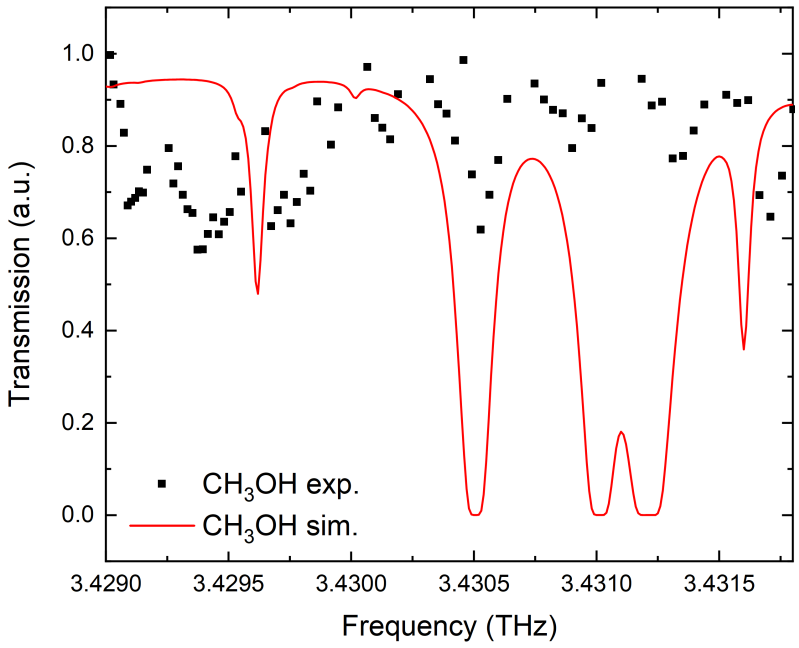

Figure 4.15: Transmission spectrum of CH_3OH taken at a frequency of 3.42 THz and a QCL temperature of 10 K. Gas pressure of 3 Torr and a gas temperature of 298 K. Spectrum excludes data points where the sample peak area is larger than that of the reference peak area. Simulated data taken from the JPL catalogue are shown by the red line.

With the removal of the uncertain data points, the transmission spectrum still does

not exhibit any definable features (see Figure 4.15). The experimental data fails to identify the peaks at 3.4296 THz, 3.4310 THz, 3.4312 THz, and 3.4316 THz. Whilst there is some suggestion of a peak at 3.4305 THz, the maximum transmission value at this frequency is ≈ 0.6 as opposed to the expected transmission $= 0$ from the simulated data.

An alternate data analysis approached was demonstrated by Yingjun Han [134]. Here, CH_3OH was measured at a pressure of 5 Torr (1.64×10^{17} molecules cm^{-3}) from 110–240 mA. Here the initial values for the fitting algorithm were adjusted manually for each current to mitigate the effects of noise, baseline and power fluctuations. This process eliminates many of the poorly fitted data points from the automated algorithm (see Figure 4.16) but is impractical, time-consuming, and is susceptible to human bias.

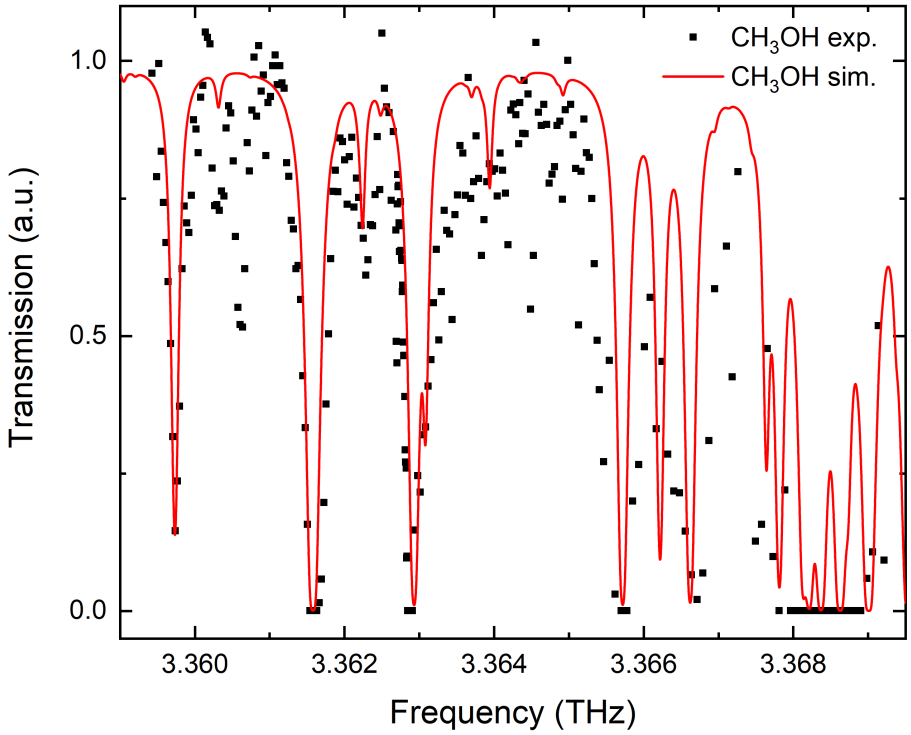

Figure 4.16: Transmission spectrum of CH_3OH taken at a pressure of 5 Torr at a QCL temperature of 10 K at a frequency of 3.36 THz. Simulated data taken from the JPL catalogue are shown by the red line.

4.4 D_2O

In order to conclusively determine if the peaks in the spectrum can be assigned to catalogued gas lines, further measurements were taken of pure D_2O at various pressures. D_2O was chosen as it has one singular strong peak within the frequency bandwidth of this QCL. Results and discussion are in the following section.

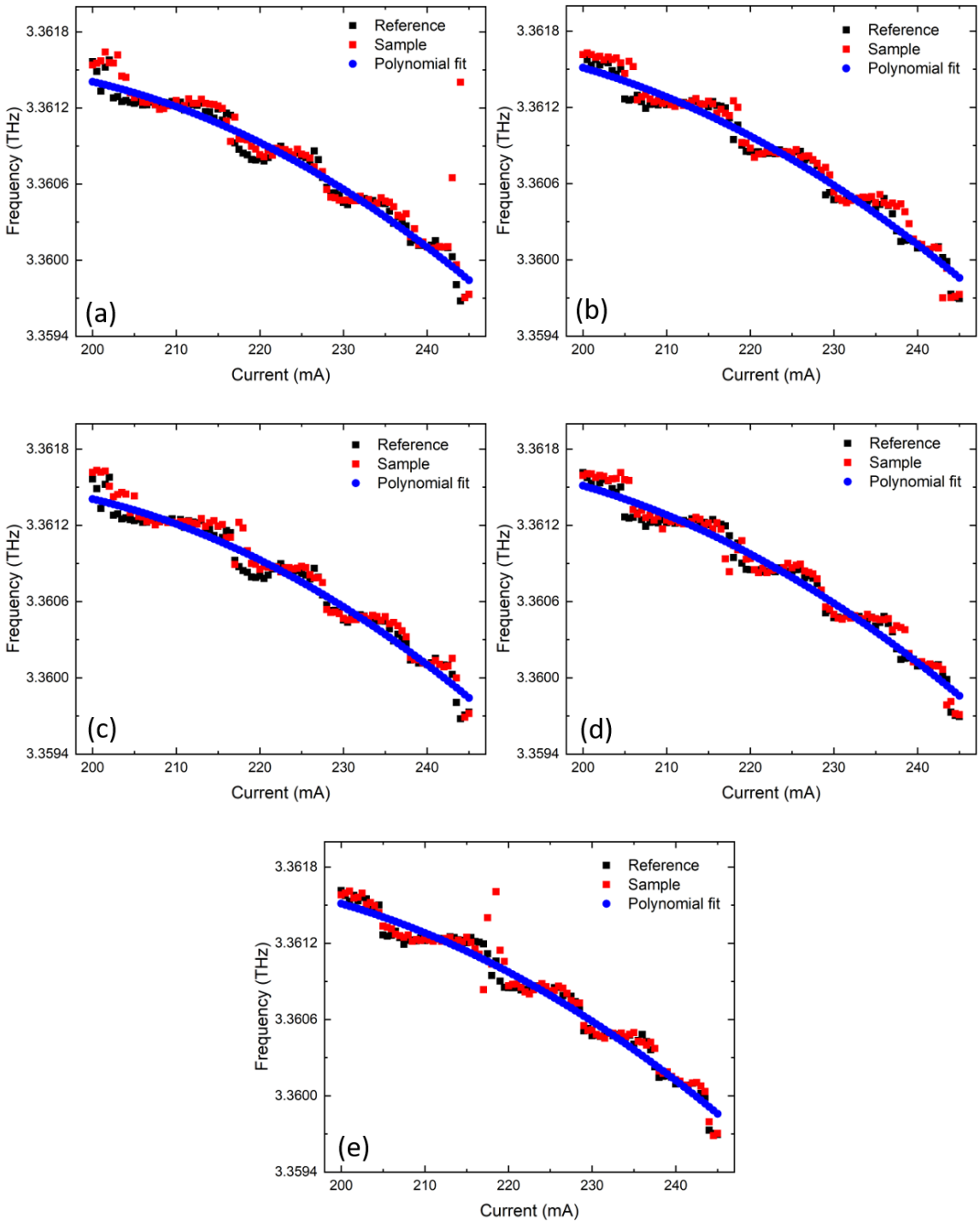

Figure 4.17: Frequency vs current plot of pure D_2O at a pressure of (a) 0.1 Torr (b) 0.2 Torr (c) 0.3 Torr (d) 0.4 Torr and (e) 0.6 Torr. Blue circles are the polynomial fits.

The transmission spectrum of D_2O at 0.1 Torr, 0.2 Torr, 3 Torr, 0.4 Torr, and 0.6 Torr was recorded, with the corresponding concentrations ranging between 3×10^{15}molecules cm^{-3} at the lowest pressure, 0.1 Torr, to approximately 1.97×10^{16} molecules cm^{-3} at 0.6 Torr. Measurements were taken with the QCL

driven between 200 mA and 245 mA with a step size of 0.5 mA at a QCL temperature of 10 K and a gas temperature of 298 K, corresponding to a frequency range of 3.3598–3.3615 THz. At each current there were 8 iterations taken and averaged.

As mentioned previously, the frequency of the emission mode varies at certain currents between the reference and sample FFT. Figure 4.17 exhibits the frequency of the 3.36 THz mode for both the reference and sample FFTs as a function of current for each pressure, and the polynomial fit that is used to extract the frequency.

Referring to Figure 3.9, between this current range, the two main emission modes from this QCL, 3.36 THz and 3.42 THz are both active. However, for this data set only the 3.36 THz mode is present. Figure 4.18, is an example of a reference FFT from this data set in which the 3.42 THz mode is not present. What is seen is the strong 3.36 THz mode alongside the weaker 3.29 THz mode that also appears in Figure 3.9 at this current. The absence of the 3.42 THz mode is likely to be attributed to an alignment issue. Coupling the radiation back into the small diagonal feedhorn of the QCL is difficult. With the modes appearing to be spatially separated, as discussed in Section 3.3.1, there is a high probability that modes will appear absent, as well as the overall signal being generally weaker. Therefore, fitting was only implemented using the 3.36 THz mode. The minimum peak prominence is 9.48×10^{-6}. Therefore, the two main peaks that can be seen at 3.29 THz and 3.36 THz can be confidently attributed as emission modes of the laser.

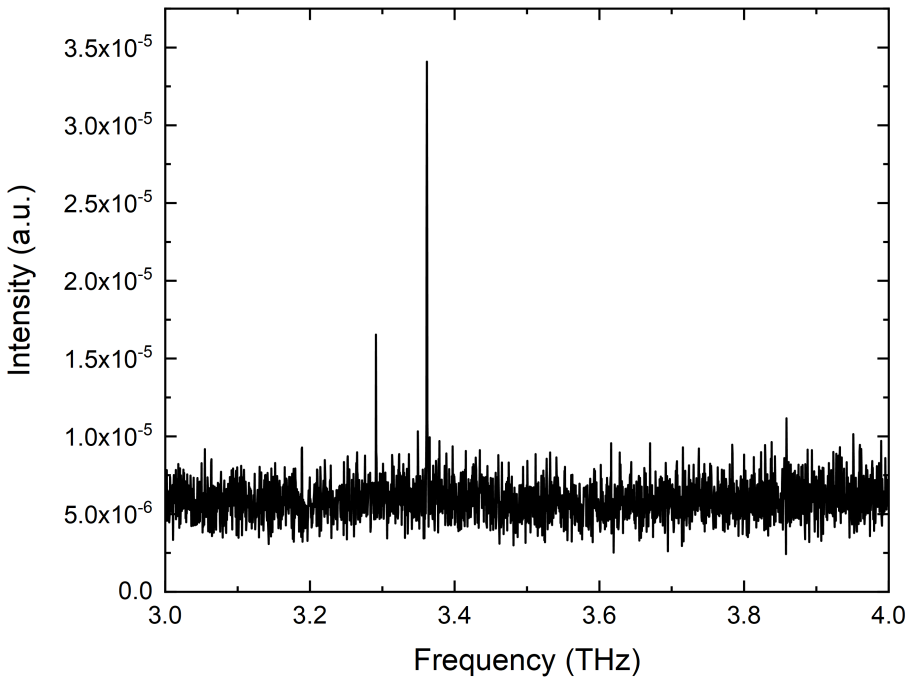

Figure 4.18: Reference FFT spectrum taken at 200 mA at a QCL temperature of 10 K. The 3.42 THz mode is not present.

The transmission spectrum including all data points, i.e. those in which the sample area under the curve is larger than that of the reference, for D_2O between 0.1–0.6 Torr is shown in Figure 4.19. Similar to the CH_3OH spectrum, transmission values > 1 is observed. A peak at 3.3603 THz that appears to increase with pressure is observed.

The error bars over the peak at 3.3603 THz are significantly smaller than the error bars for transmission values that are out of the range of 0-1. This indicates that the line is most likely a D_2O gas line. At smaller pressures, the error bars over the gas line become larger. The reason being that these data points are closer to the noise floor.

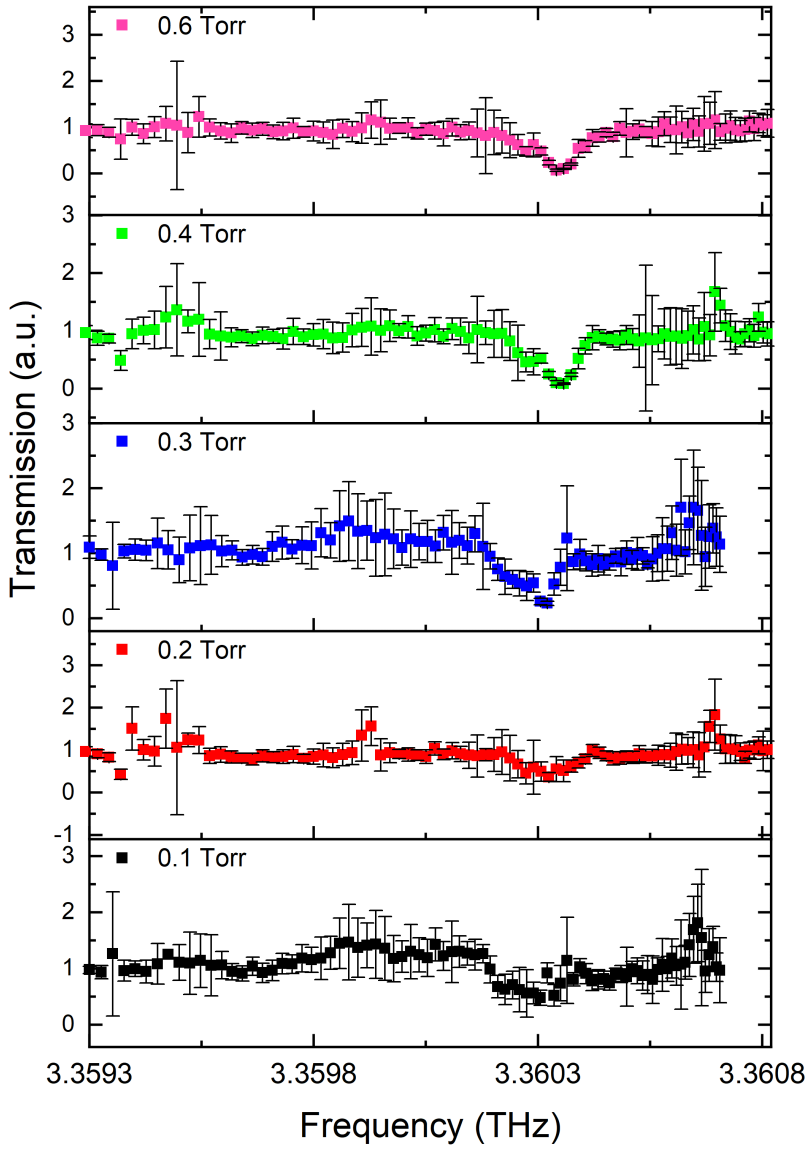

Figure 4.19: Transmission spectra of pure D_2O between 0.1–0.6 Torr at a QCL temperature of 10 K including all data points. Transmission values > 1 is observed. Black lines depict the error in the transmission values.

The data points at which the transmission value is > 1 were removed, and the resulting transmission spectrum is given in Figure 4.20. The error bars were removed for clarity and the possible gas line at 3.3603 THz is more pronounced. The gas line is confirmed from the JPL data entry for D_2O, that lists an absorption at this frequency [40].

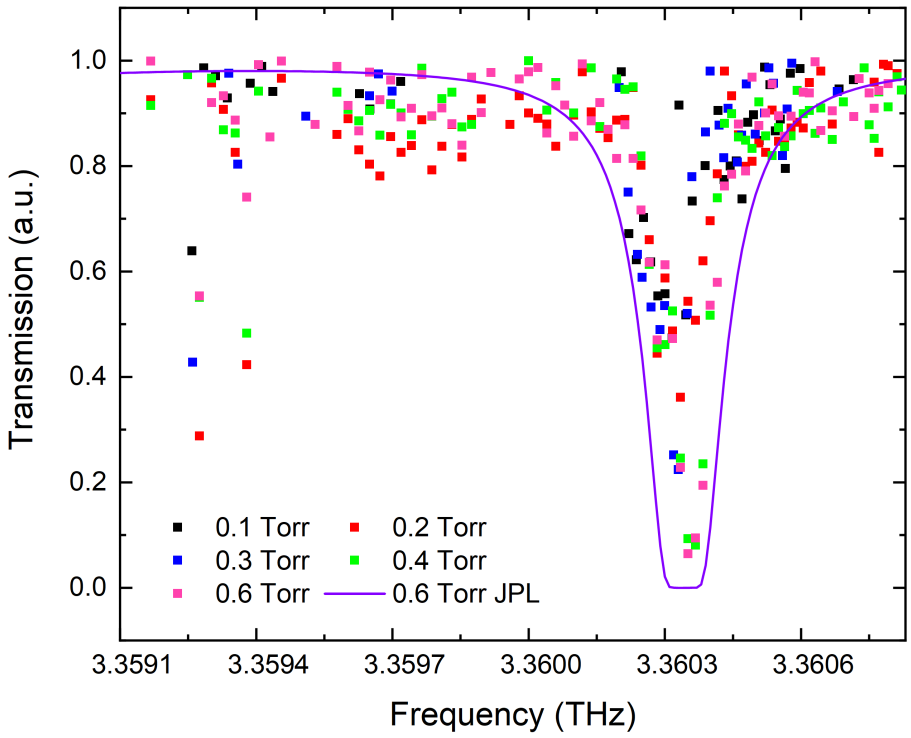

Figure 4.20: Transmission spectrum of pure D_2O at various pressures at a QCL temperature of 10 K excluding data points where the sample area is larger than the reference. Purple line indicates the simulated data of D_2O at 0.6 Torr taken from the JPL catalogue.

The origin of the two peaks that appear between 3.3592 THz and 3.3594 THz, most prominently at 0.2 Torr and 0.4 Torr cannot be determined. The JPL catalogue [40] does not list a D_2O gas line at this frequency and there is no pressure dependence exhibited.

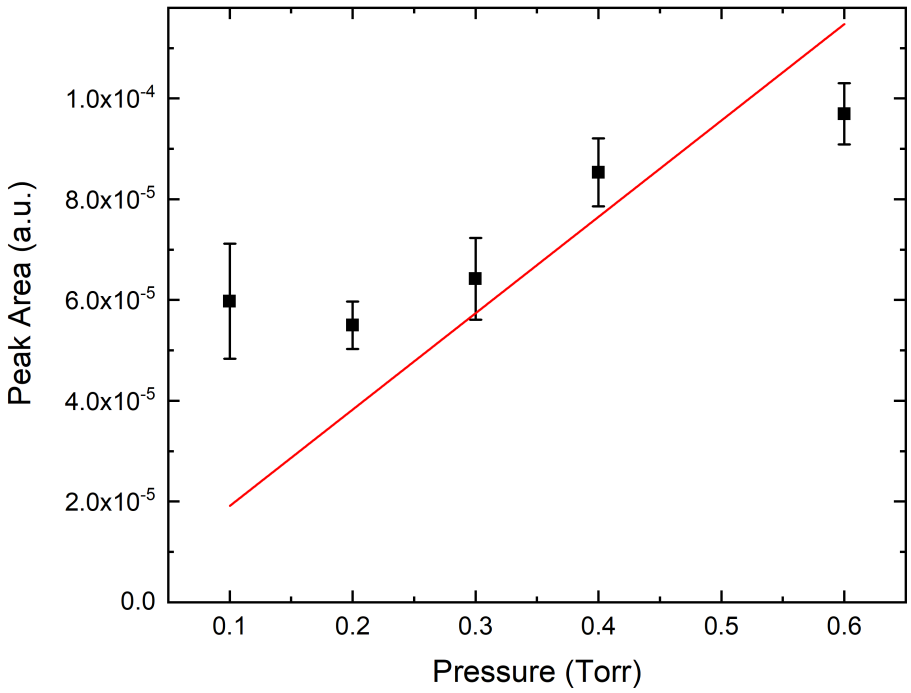

Figure 4.21: Peak area of the 3.3603 THz D_2O gas line as a function of pressure. Red line shows the linear fit that was applied.

Figure 4.21 depicts the peak area as a function of pressure with a linear fit applied. The general trend shows that as the pressure is increased, the peak area and hence absorption increases.

4.4.1 D_2O 1 Torr reaction

The transmission spectrum of D_2O and HDO at 1 Torr were measured between the current range 110–140 mA with a step-size of 0.2 mA at a QCL temperature of 10 K and a gas temperature of 298 K. D_2O at a pressure of 1 Torr reacted with H_2O vapour to form HDO. The equilibrium constant for the reaction at 25° is given as $K_1 = 3.2$ [147]. With the initial concentration of H_2O vapour being residual amounts from previous experiments (i.e. very low), it is assumed that equilibrium is reached.

Whilst H_2O vapour exhibits several spectral lines throughout the THz region, at this particular frequency, no absorption by H_2O vapour is expected. Fitting was performed to the 3.36 THz mode only, as no gas lines for D_2O, H_2O or HDO appear around 3.42 THz.

The frequency extracted from the Gaussian fit for the reference and sample FFTs as a function of current and the corresponding polynomial fit is given in Figure 4.22. What is most notable from this plot is the discrepancies in frequency between the reference and sample data. Unlike other frequency vs current plots like above, the sample frequency is much higher than the corresponding reference frequency.

One likely reason could be a temperature increase or decrease in the room causing mechanical drift between taking the reference and sample measurement.

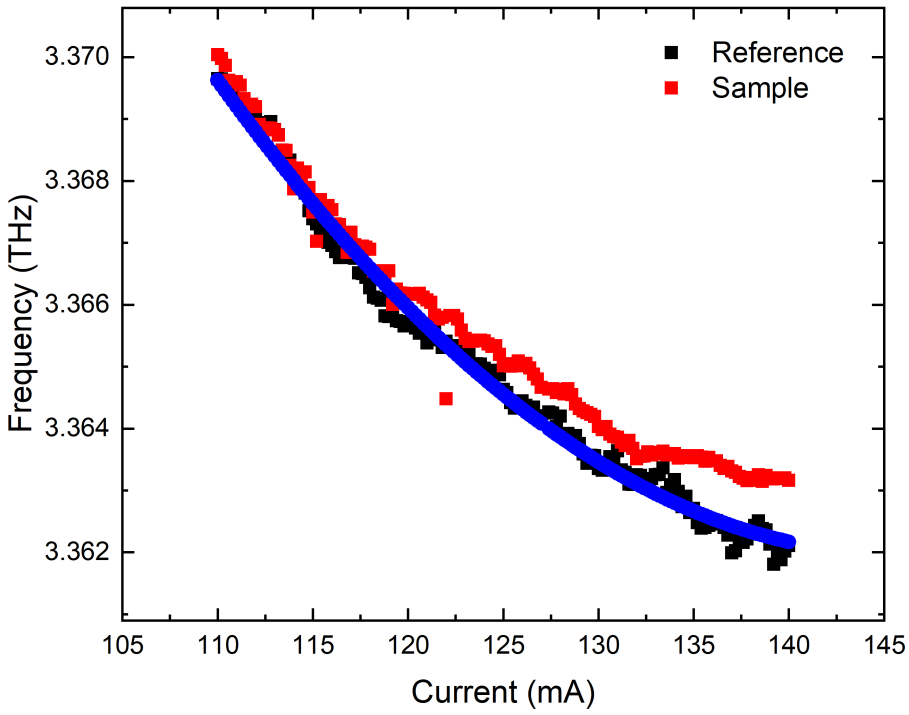

Figure 4.22: Frequency vs current plot of reference and a D_2O/HDO mixture at 1 Torr. Blue circles show the polynomial fit done in order to extract the frequency.

The transmission spectrum including all data points with their corresponding error bars is shown in Figure 4.23. In addition to the frequency offset discussed in Section 4.3, a frequency offset of 0.3 GHz has also been corrected for owing to the frequncy difference between the sample and reference fitting in Figure 4.22. A significant number of data points with a transmission value > 1 is observed between 3.362 THz and 3.363 THz, resulting in large error bars. However, peaks that correspond to D_2O at 3.3652 THz, 3.3659 THz, 3.3673 THz, 3.3678 THz and HDO at 3.3667 THz can be seen, exhibiting relatively small error bars.

With the removal of the uncertain data points, the gas lines are more pronounced (Figure 4.24) and align well with the simulated data. Therefore, it has been demonstrated that with the current SM setup, a mixture at a concentration of 3×10^{16} molecules cm^{-3} of multiple peaks can be resolved.

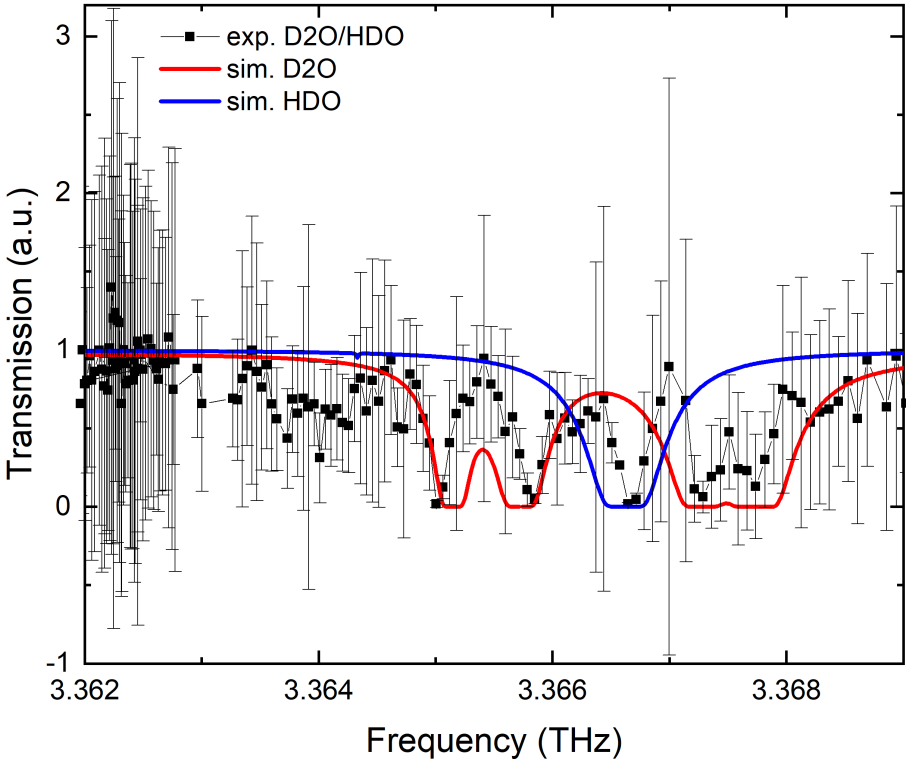

Figure 4.23: Transmission spectrum of a D_2O and HDO mixture at 1 Torr including all data points and corresponding error bars from 110 mA to 140 mA.

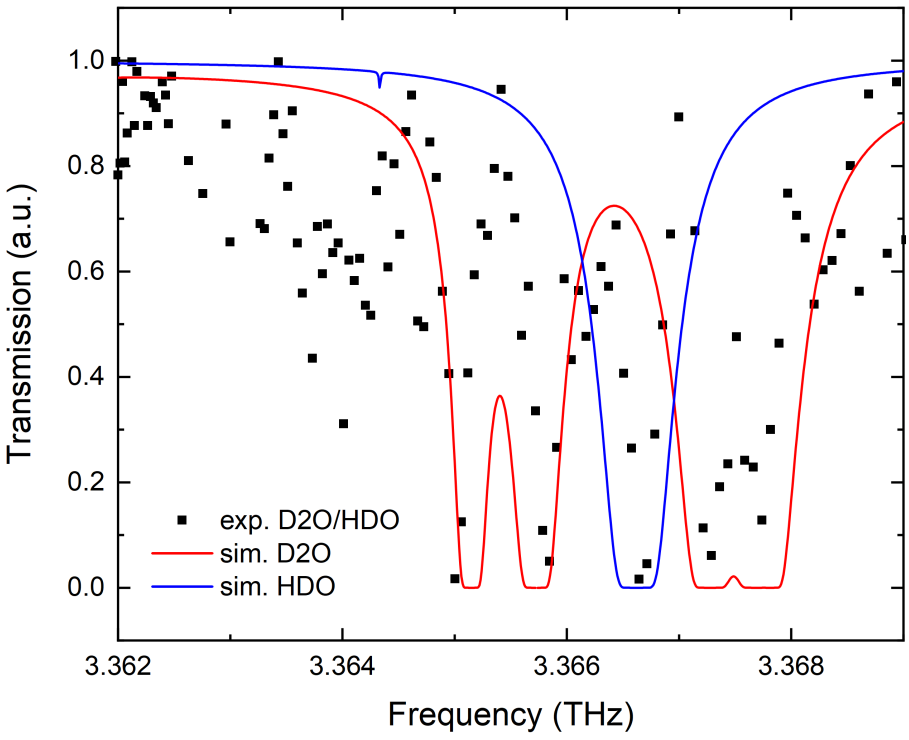

Figure 4.24: Transmission spectrum of a D_2O and HDO mixture at 1 Torr excluding the data points where negative transmission has occurred from 110 mA to 140 mA.

Despite the fact that gas lines may have been identified in the above data set, the power instability issues are still extremely present. On the same day, further data was recorded of the 1 Torr D_2O/HDO mixture between the current range of 141–240 mA with a 1 mA step-size at a QCL temperature of 10 K. Figure 4.25 shows the transmission spectrum. A frequency offset of 0.7 GHz has been corrected for. Out of 99 current data points, only 10 exhibited a transmission value between 0-1. As a result, the error bars are extremely large. One gas line is expected at 3.3604 THz. The corresponding experimental data points at this frequency does show smaller error bars than others in this data set. This suggests that the experimental data does depict the D_2O gas line.

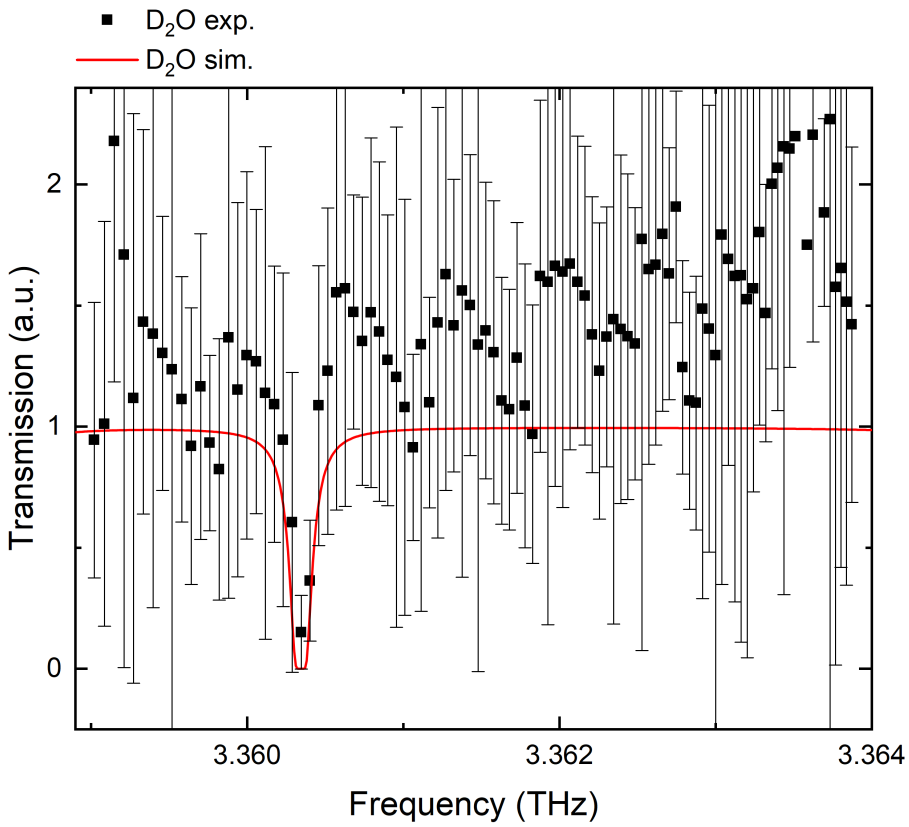

Figure 4.25: Transmission spectrum of a D_2O and HDO mixture at 1 Torr and a QCL temperature of 10 K. Includes all data points from 141 mA to 240 mA.

The resultant transmission spectrum with the removal of the uncertain data points is given in Figure 4.26. The frequency range is reduced down to a 3 GHz bandwidth. With only three points over a peak, it cannot be conclusively determined without the JPL simulated data if the peak is a gas line or noise.

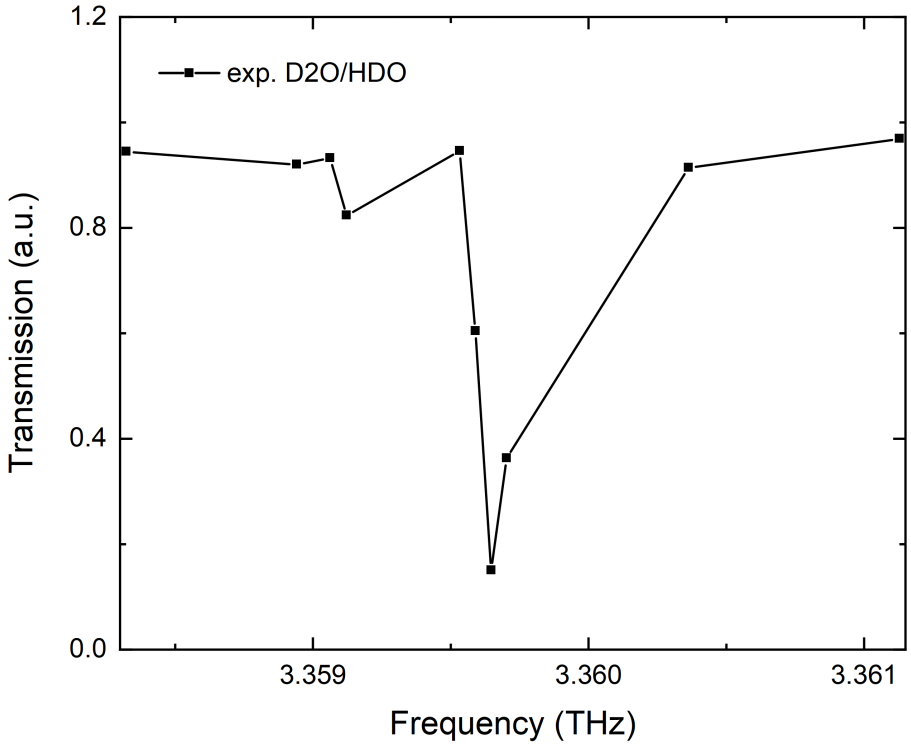

Figure 4.26: Transmission spectrum of a D_2O and HDO mixture at 1 Torr excluding the data points where negative transmission has occurred from 141 mA to 240 mA.

4.5 Conclusion

Following on from the measurements of the D_2O/HDO mixture, the initial plan was to measure more deuterated gaseous species and monitor changes in concentration of reactive mixtures. An initial measurement of a CH_3OH and D_2O mixture and the potential products of the reaction was performed. The output transmission spectrum exhibited a number of discrepancies between the experimental data and the simulated data from JPL. Similar to the above spectra, the spectrum appeared noisy, under-sampled with the removal of uncertain data points, and there were no distinguishable gas lines. It was determined that a number of issues had to first be addressed before further gas spectroscopy measurements were performed. Firstly, the achievable sensitivity of the above system does not meet the requirements to study trace gases that appear in our atmosphere and space. With the current SM system the minimum concentration of gases that was able to be detected was 3×10^{15} molecules cm^{-3} (130 ppm). In order to replicate conditions found in our atmosphere and space, such as O, where the concentration is 1×10^{12} molecules cm^{-3} (50 ppt or 250 ppm for MLT conditions) an increase in sensitivity is required. In addition, the system would need to be an order of magnitude more sensitivity to monitor the change in concentration over time of reactions. To increase the sensitivity of a

system, a multipass gas cell is usually used (see section 1.2.2). Adopting a multipass gas cell with SM is extremely difficult. After multiple passes, the signal, which is already weak owing to coupling back into the feedhorn aperture, is made weaker from reflection losses. The phase contribution from these multiple reflections will also be difficult to analyse. In parallel, the alignment back into the aperture becomes increasingly arduous, especially with radiation that is not visible.

It appears clear that the QCL used exhibits a certain degree of power instability that leads to a noisy and under-sampled frequency spectrum. Measurements have been reported in literature that have successfully produced a clear gas spectrum [136, 145, 148], all of which utilise a single-mode unmounted QCL (the measurements presented in reference [136] were taken in the same laboratory as the one used for this work). As a result, it is implied that owing to the multimode nature of the device, the power fluctuations are larger and cause more uncertainty in the transmission.

Whilst these devices exhibit a non-Gaussian beam profile (Section 3.3), it is concluded that this did not influence the ability to take gas-phase spectroscopy measurements. The beam profiles discussed in Section 3.3 were of the beam propagating into free space. The measurements presented in this chapter collimated the beam through the gas cell before being focused into the detector and so in theory should remove any issues the uneven distribution of frequency modes could cause from the divergent beam.

To address these stability issues, power tests and changes to the experimental setup were made. The next chapter presents these tests and introduces the new design with some preliminary gas spectroscopy measurements.

Chapter 5

THz FTIR spectroscopy

In this chapter, the second method used in this project is introduced, FTIR spectroscopy. The basic principles behind the method are first described, as well as a few examples of the wide range of applications that have adopted this technique. Following on from that, preliminary gas measurements taken are presented and analysed. The end of this Chapter addresses the QCL power instability that has been encountered through the number of gas spectroscopy measurements performed in this project.

5.1 FTIR spectroscopy

The principles behind FTIR spectroscopy make use of interferometry, where interference effects generated by a superposition of waves are measured. Observations of interference are generally attributed to Isaac Newton (see Section 1.1 for more detail on the history of spectroscopy). However, the invention of interferometry as a technique is accredited to Albert Michelson, who in 1881 created the Michelson interferometer [149]. Since, a number of variant interferometer configurations have been developed [150–152], all of which are commonly used in scientific studies such as in the field of astronomy [153–155], oceanography [156, 157], and spectroscopy [158, 159].

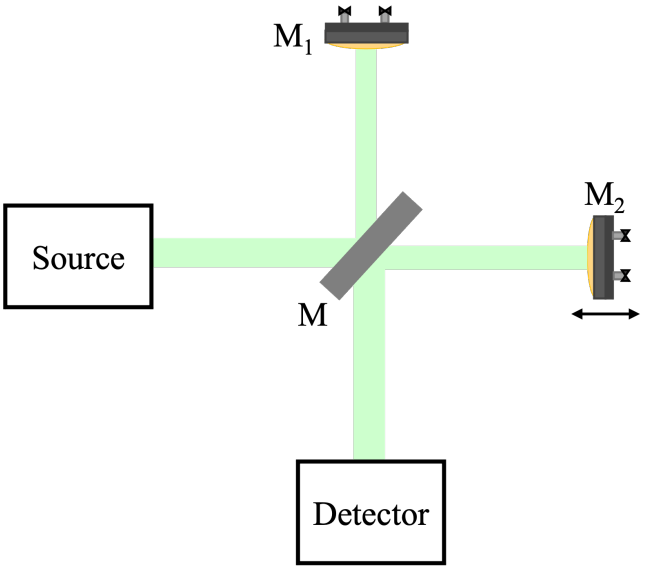

Figure 5.1: Schematic diagram of a Michelson interferometer setup. The beam of light is split into two separate beams by a beam splitter, M. The beams travel to a stationary mirror, M_1 and a moving mirror, M_2. They are reflected back towards the beam splitter where they recombine and the interference is measured by the detector.

An FTIR interferometer (see Figure 5.1), consists of one stationary mirror (M_1) and one moving mirror (M_2). The stationary mirror is typically fixed to the optics table whilst the moving mirror is mounted onto a motorised translation stage. The beam of light passes through the gas cell before it hits a beam splitter that is at 45° to the two mirrors. The beam splitter is partially reflective and the light is split into two. One part of the beam is transmitted through the beam splitter whilst the other is reflected. Each beam of light reaches either mirror before being reflected back towards the beam splitter where the two beams recombine and produce an interference pattern. Depending on the optical path difference (OPD) between the two mirrors (defined as $2M_1 - 2M_2 = \delta$, where δ is the retardation factor), the interference will either be constructive or destructive. Constructive interference occurs when $\delta = n\lambda$ (the two beams of light are in phase), where n is an integer. Destructive interference occurs when the two beams of light are out of phase, $\delta = (n+\frac{1}{2})\lambda$. At maximum constructive interference, the two mirrors are equidistant ($\delta = 0$), and the interferogram exhibits a 'centre-burst'. In order to perform spectroscopy, a sample cell is positioned within the path of the light beam prior to the beam splitter. Subsequently, the interference is measured and an FFT of the interferogram outputs a frequency spectrum.

5.1.1 Experimental set-up

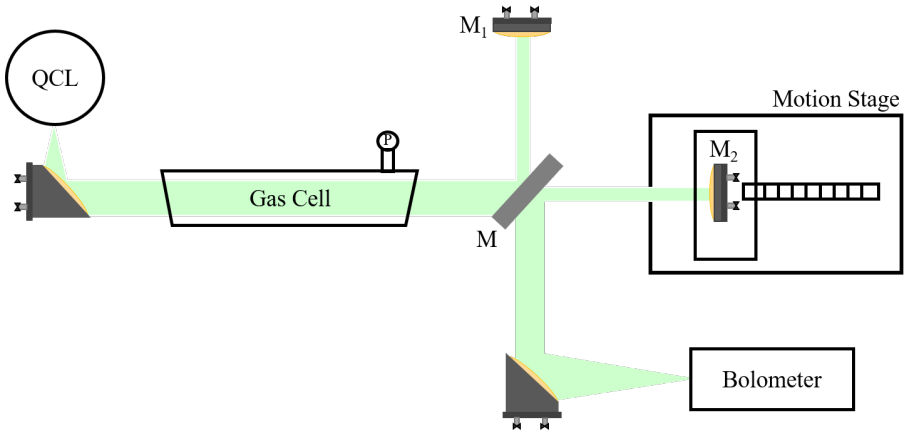

Figure 5.2: Schematic diagram of the FTIR spectrometer used in this project. The beam of light is split into two separate beams by a beam splitter, M. The beams travel to a stationary mirror, M_1 and a moving mirror, M_2. They are reflected back towards the beam splitter where they recombine. The interference is measured by a liquid He cooled Si bolometer.

The experimental set-up, shown in Figure 5.2, has a QCL mounted into a Janis ST-100 He cooled cryostat (the same cryostat used for the SM measurements).

The cryostat is initially pumped down using a turbo molecular pump to ensure the low temperature of the QCL is held and thermal insulation is sustained. In addition, pumping is required so the low operating temperature of the QCL is met. An Arroyo 4320 current source is used to drive the QCL. Light is emitted from the QCL and is collimated using a parabolic mirror. The light passes through a 965 mm long glass gas cell before it is split into two separate beams by a beam splitter. Half of the beam is reflected by the beam splitter onto a stationary mirror (M_1) whilst the other half of the beam passes through the beam splitter and is reflected of a moving mirror (M_2) that is mounted onto a Newport ILS-200 mechanically adjustable motion stage. The two beams recombine at the beam splitter and the interference is measured by a liquid He-cooled Si bolometer.

For the gas spectroscopy measurements, reference scans were taken with the gas cell purged with N_2 and pumped down to a base pressure of 3 Pa. The interference at each current was measured before the sample was injected into the gas cell using an MKS instruments GM50A mass flow controller and the interferogram was measured again.

For the following measurements, 'Device A' and 'Device B' were used.

5.2 Sampling methods

In order to optimise the FTIR spectrometer. A number of tests were performed. Firstly, different sampling schemes were tested. One way to control the sampling intervals is from using the XPS controller, as demonstrated with the SM measurements in the previous chapter.

The emission spectrum of Device A was recorded at 140 mA at a QCL temperature of 10 K with the stage speed set at 10 mm/s and a repetition rate of 10 kHz. The spectrum is shown in Figure 5.3 along with the QCL emission spectrum recorded with the FTIR Bruker system in Figure 3.9 as a comparison (see Section 3.2.3 for Bruker parameters). The spectrum exhibits 2 sharp asymmetric peaks at 3.34 THz and 3.36 THz, as well as weaker peaks at 3.29 THz and 3.43 THz, all of which correspond to the QCL emission peaks recorded with the FTIR Bruker system. The QCL modes recorded with the FTIR spectrometer have a small frequency offset to the Bruker measurement. Similarly to what was discussed in the previous chapter, the frequency offset can be caused by a number of means, most likely being a $\cos\theta$ error from the stage.

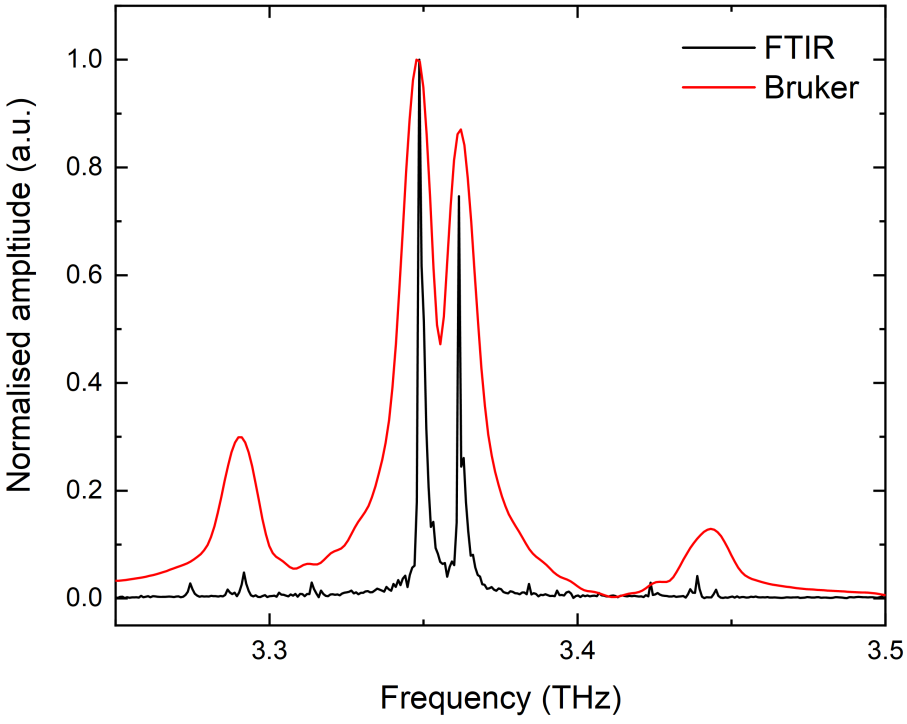

Figure 5.3: QCL emission spectrum recorded at 140 mA at a QCL temperature of 10 K. The position intervals have been triggered using the XPS controller.

The QCL emission spectrum was measured again using the DAQ internal clock. The emission spectrum of Device A was recorded at 240 mA at a temperature of 15 K

with the stage speed set at 10 mm/s and a sampling rate of 10 kHz. The spectrum, shown in Figure 5.4 shows 6 asymmetric peaks, 5 of which match with the emission modes measured using the FTIR Bruker. An extremely weak peak at 3.26 THz is shown, as well as two asymmetric unexplained peaks at much weaker intensity at 3.381 THz and 3.460 THz, equidistant apart from the main QCL mode at 3.42 THz.

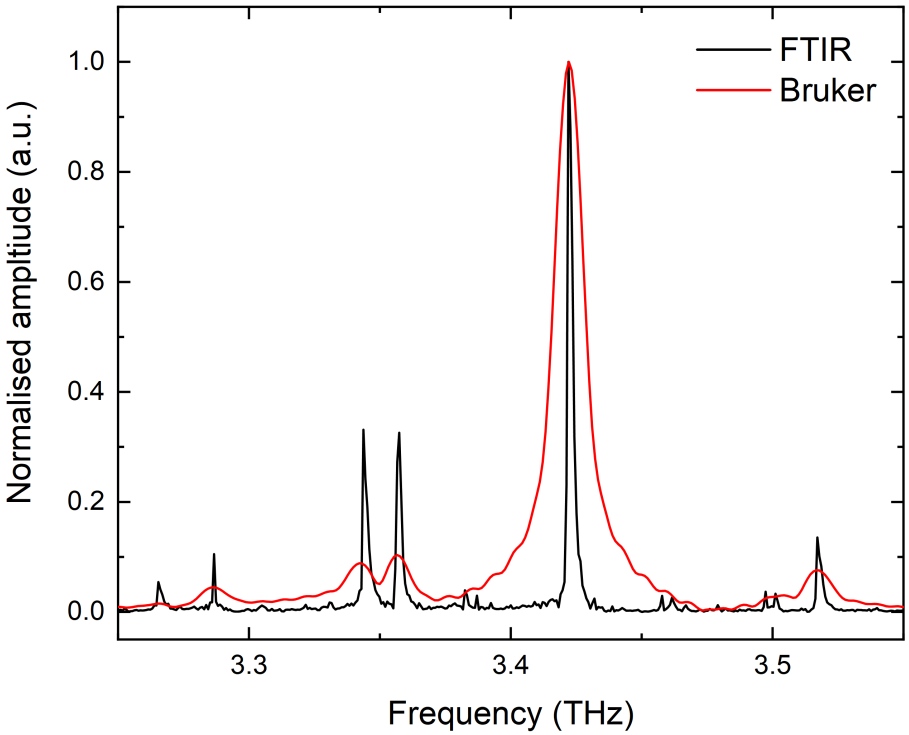

Figure 5.4: QCL emission spectrum recorded at 240 mA at 15 K. The position intervals have been triggered using a DAQ board internal clock.

The data were truncated to remove the influence that acceleration and deceleration would cause, and therefore the peaks cannot be attributed to position error caused by the varying stage velocity. Ghosts and artefacts in FTIR spectroscopy are not unheard of and can be caused by amplitude modulation, frequency mixing from nonlinear detection and/or variations of the spatial sampling intervals [160]. Specifically here, frequency-modulation ghosts (otherwise known as side bands or phase ghosts) appear as asymmetric lines on either side of the spectral peak and arise from periodic errors in the sampling scheme.

Lastly, the QCL emission spectrum was calibrated using a HeNe laser. An interferogram was measured for the HeNe laser of known wavelength 632.8 nm using the same apparatus that is used for the gas spectroscopy measurements. This allowed for the stage position to be calibrated accurately and hence the THz interferogram will have more accurate position data. Figure 5.5 shows the QCL emission spectrum. The spectrum was recorded with the QCL lasing at 200 mA at a temperature

of 20 K. In this instance, a 100 kHz sampling rate was used. What is shown is the QCL emission modes that align well with the data obtained using the FTIR Bruker system. Moreover, the sidebands that were displayed in the spectrum obtained from using the DAQ internal clock are much weaker in intensity. This is most likely due to the periodic sampling intervals being more accurate with the IR laser.

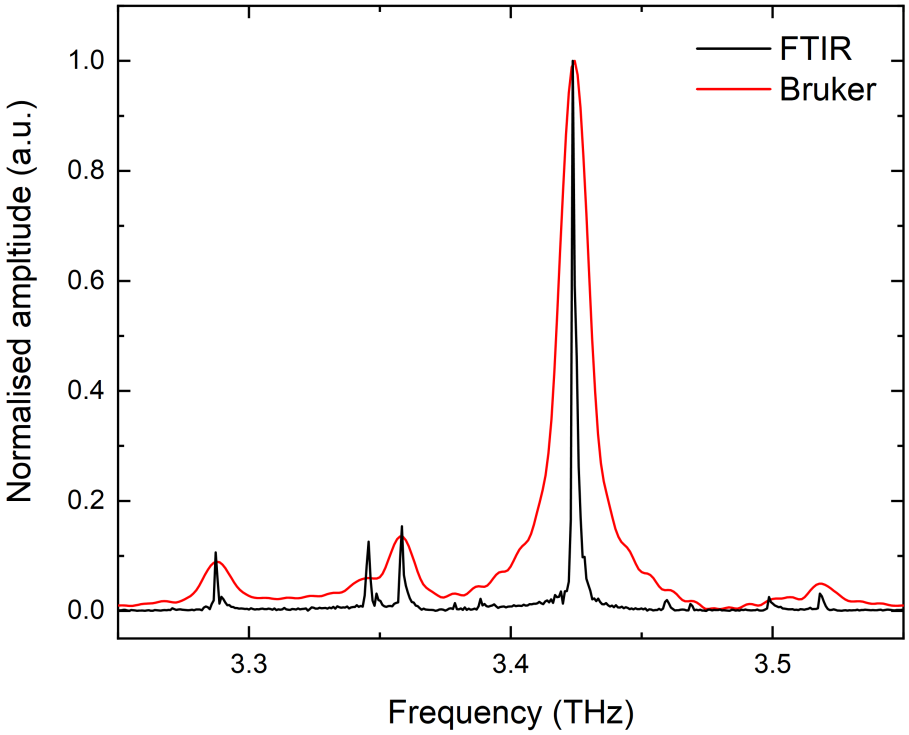

Figure 5.5: QCL emission spectrum recorded at 200 mA at 20 K. The position intervals have been triggered using a HeNe laser of a known wavelength.

5.3 Repeatability scans

Further measurements were done to test the QCL power fluctuations. Here, the QCL emission spectrum at 140 mA at a QCL temperature of 10 K was measured ten times with each scan taken one minute apart (see Figure 5.6). The position triggering was configured using the XPS controller. Over the course of ten minutes, it was shown that the intensity of both modes fluctuates. For the 3.34 THz mode (5.6a, the intensity of the mode increased with time. However, the intensity of the 3.36 THz (5.6b) mode fluctuated with no obvious trend. For example, at 3.34 THz, the tenth scan exhibits the largest intensity, whilst at 3.36 THz, the seventh scan has the largest intensity. There is a calculated 3 % relative noise level in each peak. Further investigation into the fluctuations is given in Sections 5.4 5.5 and 5.5.1. These scans confirm what was discussed in the previous section, it is unlikely that the power instability can be accredited solely to the SM effect, and is more likely to be caused by an environmental factor in the laboratory, and/or the integration of

the QCL.

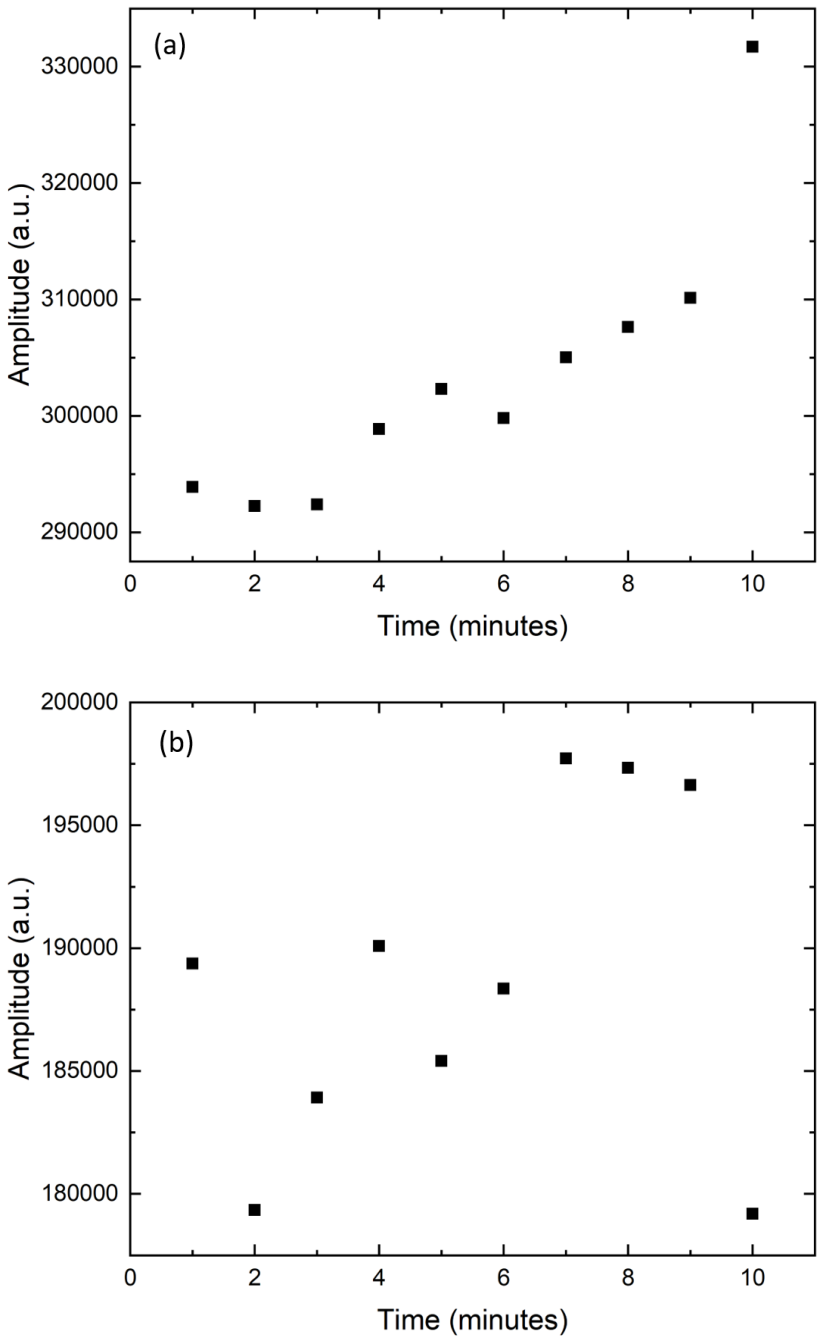

Figure 5.6: The maximum amplitude of the QCLs emission modes at (a) 3.34 THz and (b) 3.36 THz of Device A at 140 mA over the course of ten minutes. The QCL temperature was set to 10 K.

5.4 Preliminary gas measurements

CH_3OH was measured at a pressure of 266 Pa using Device A between 110–140 mA with a current step-size of 0.2 mA. The stage scanning velocity was set to 10 mm/s, with the QCL operating at a QCL temperature of 10 K. At each current, 3 scans

were taken and averaged. The sampling rate was 100 kHz with the sampling intervals triggered from the XPS controller.

Firstly, an FFT spectrum obtained from using the FTIR spectrometer was compared to an FFT spectrum taken using the SM system at the same current and temperature. Both spectra are plotted in Figure 5.7. This was done in order to judge whether the FTIR spectrometer caused any improvements in the signal and noise floor. As well as to determine if there were any discrepancies in the intensity of the active modes. As was seen in Figure 5.6, the intensity of each mode fluctuated with time.

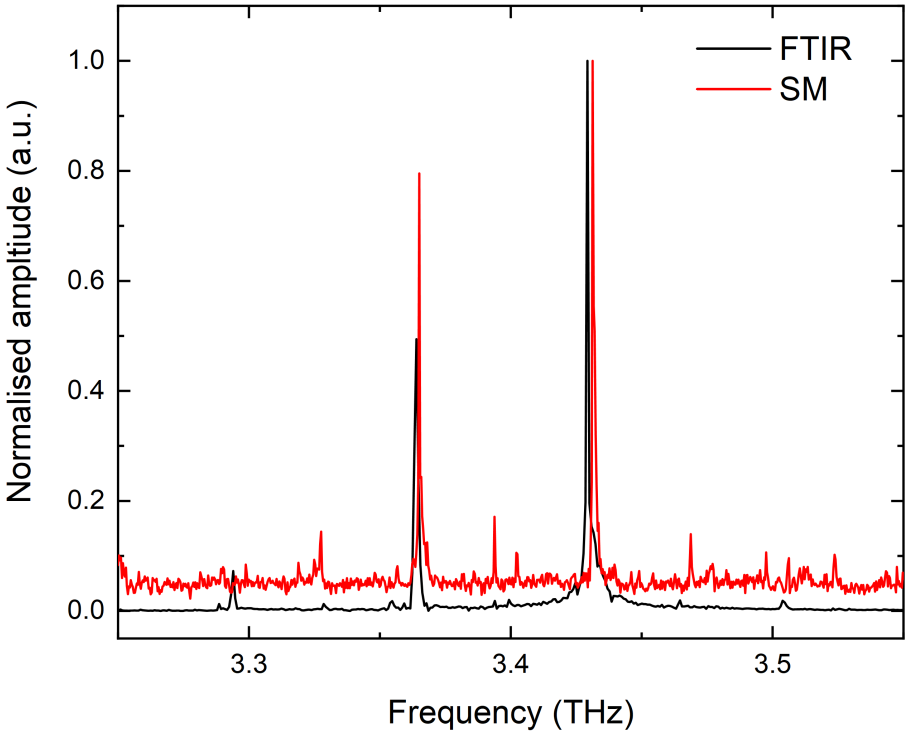

Figure 5.7: QCL emission spectra taken using the FTIR spectrometer (black) and the SM set-up (red) at 125 mA.

The FFT recorded using the FTIR spectrometer depicts a much smoother and less noisy QCL emission spectrum, with a signal-to-noise ratio (SNR) of 253 compared to 19 calculated from the SM spectrum at the 3.42 THz mode. However, asymmetry still appears in the FTIR FFT, particularly at the 3.42 THz mode, although no phase ghosts are present. Both with the SM and FTIR data, the 3.42 THz mode was the dominant mode.

Four reference and sample FFTs measured at 120.0 mA, 125.0 mA, 130.0 mA and 140.0 mA are given in Figure 5.8. At 120.0 mA, the two expected modes are active, 3.36 THz and 3.42 THz. The reference peak area is larger than the sample peak area at 3.36 THz, indicating an absorption has occurred. However, whilst an absorption

is also expected at 3.42 THz, the sample peak area at 3.42 THz is larger than that of the reference. Contrastingly, at 125.0 mA, the reference peak areas at 3.36 THz and at 3.42 THz are both smaller than the sample peak areas at the corresponding frequencies. At 130.0 mA, the reference peak area at 3.36 THz is larger than the sample peak area, whilst at 3.42 THz, the reference peak area is smaller than the sample. In addition to these two modes, at this current, Figure 3.9 shows that the 3.34 THz mode is also active, however this mode does not appear in either the reference or the sample FFT. At 140.0 mA, the expected active modes are 3.34 THz and 3.36 THz. Interestingly, the sample FFT at this current instead depicts two active modes at 3.36 THz and 3.42 THz. This also occurs at the currents 137–140 mA whilst the reference FFT depicts the correct expected active modes. Figure 3.9 shows that the 3.36 THz mode should increase in intensity with current (with the exception of at 130.0 mA where the mode is weaker). This is not the case, and at 120.0 mA the mode is most intense. Similarly, the 3.42 THz mode is expected to be the most intense at 125.0 mA but instead this current exhibits the weakest 3.42 THz mode. The measurements recorded on the FTIR Bruker system act as a guide to the expected modes and intensities across a specific current range. The variations in intensity of the modes between the two systems can be put down to the different optical systems used, as well as fluctuations in temperature between the laboratories, as the bolometer is sensitive to thermal changes. In addition, two different detectors were used for each measurement, the different aperture size and response time would all cause fluctuations in the intensity. However, the above reasons cannot explain why the sample peaks would exhibit a larger area than the reference when an absorption is expected at this frequency. It was therefore concluded that this data set would not produce a reliable transmission spectrum owing to the random variations in intensity and active modes throughout the measurement.

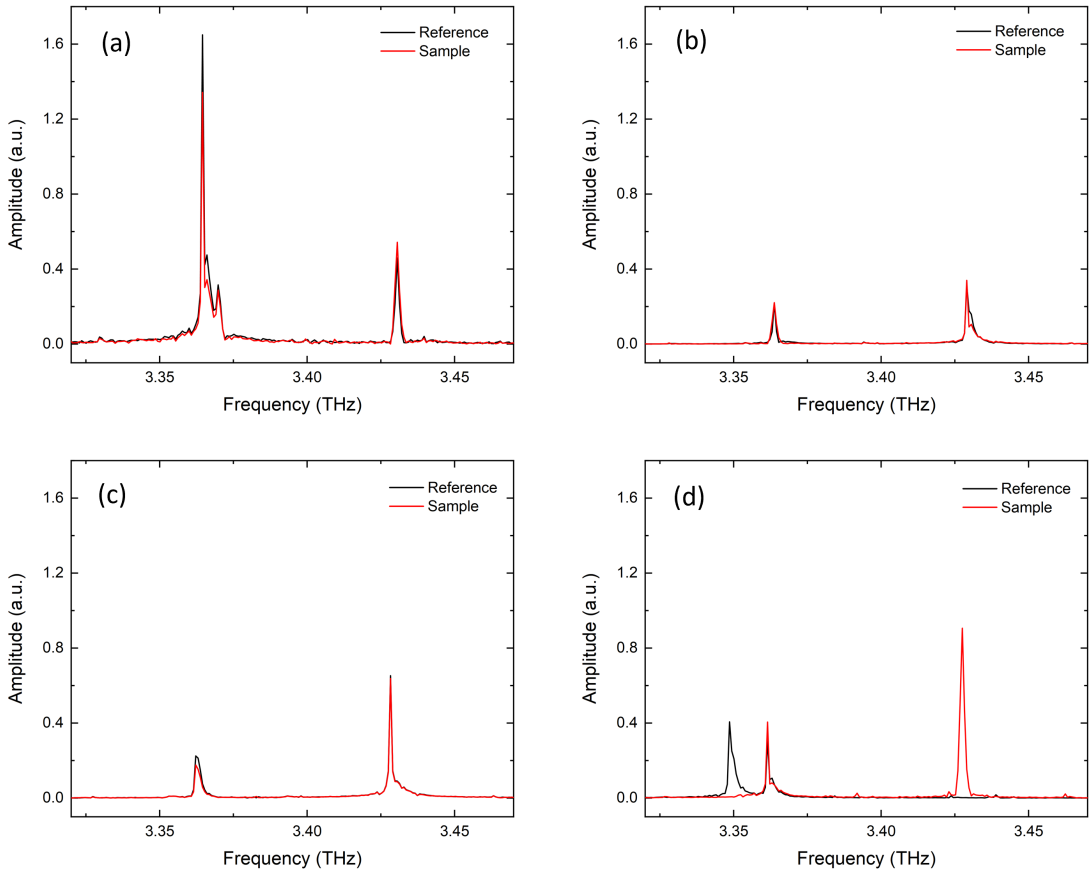

Figure 5.8: Reference and CH_3OH sample FFTs taken at (a) 120.0 mA, (b) 125.0 mA, (c) 130.0 mA and (d) 140.0 mA, at a QCL temperature of 10 K.

The measurements were repeated. The parameters were kept the same although the system was re-aligned. Interferograms were recorded with the QCL temperature at 10 K between 110–132 mA with a 0.2 mA step-size. The reference and sample FFTs at 120.0 mA, 125.0 mA and 130.0 mA are depicted in Figure 5.9. At 120.0 mA, absorption has occurred at both frequencies. This is unlike what was seen at 120.0 mA in the previous set of measurements (Figure 5.8a). At 125.0 mA, no absorption has taken place at 3.36 THz but an absorption has occurred at 3.42 THz. Again, this is different to previous measurements (Figure 5.8b). Similar to the FFTs measured at 130.0 mA in the first set of measurements, absorption has occurred at 3.36 THz, whilst at 3.42 THz the sample peak is larger than the reference peak area (Figure 5.9c).

Since inconsistencies between data sets still appeared, an accurate transmission spectrum could not be produced. Before any more gas spectroscopy measurements can be done, these discrepancies must first be addressed.

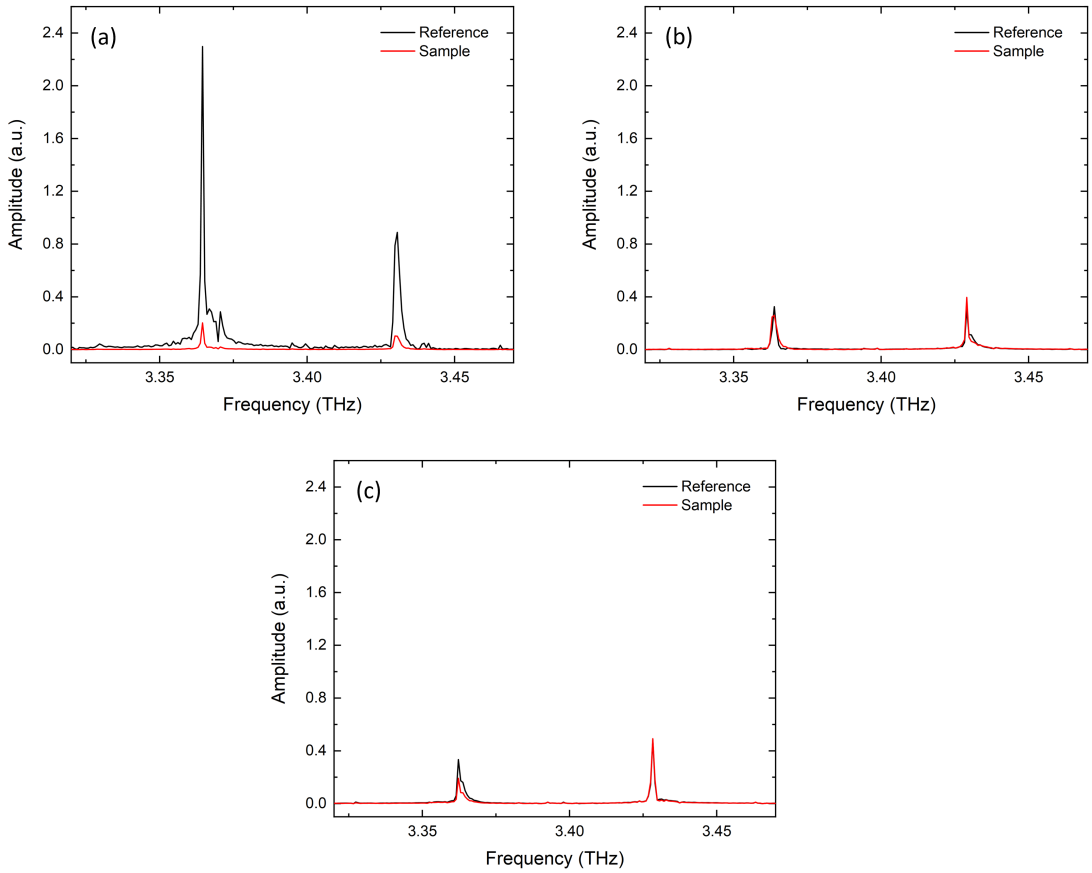

Figure 5.9: Repeat measurement of reference and CH_3OH sample FFTs taken at (a) 120.0 mA, (b) 125.0 mA, (c) 130.0 mA at a QCL temperature of 10 K.

5.5 Device A Power measurements

The output power of the QCL was measured directly using a liquid He cooled Si bolometer. The QCL was driven at a current of 140 mA at a temperature of 10 K. The absolute power was 2 mW. The output power as a function of time is given in Figure 5.10. The power of the QCL appears to fluctuate over time, with a drop in power at 58 minutes.

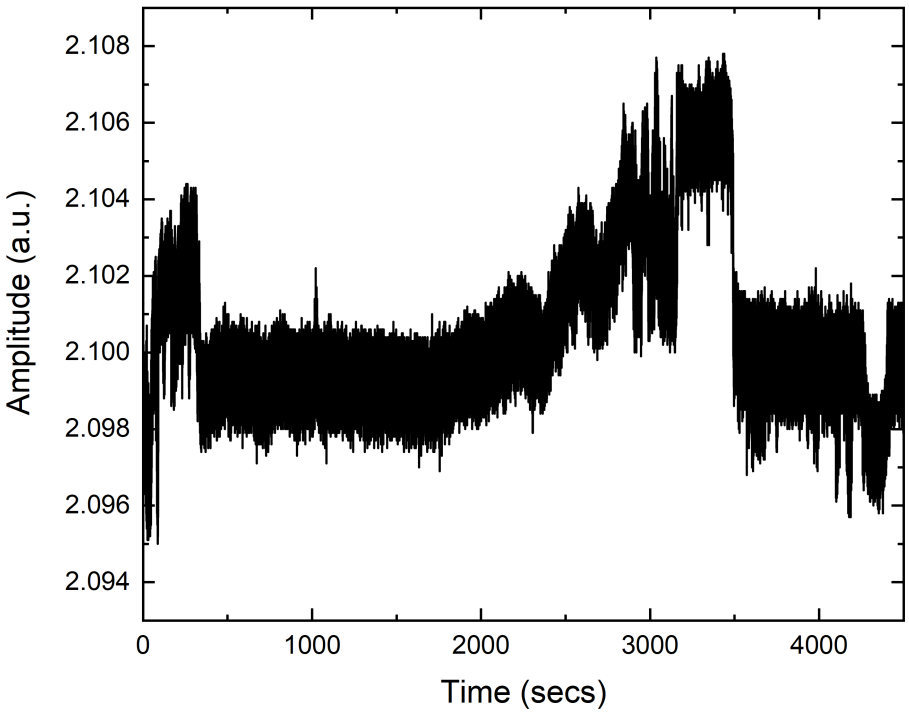

Figure 5.10: Output power of the QCL recorded over 75 minutes at a drive current of 140 mA and a QCL temperature of 10 K.

At 140 mA, the 3.34 THz and 3.36 THz modes are both active. The fluctuation in power of the modes as a function of time is given in Figure 5.11 and is considerably larger than the overall output of the QCL given in Figure 5.10. There is a calculated 10.80 % relative noise level over the 3.34 THz peak and a 9.03 % relative noise level over the 3.36 THz peak. At 3.34 THz, the power appears to drop in intensity before it slowly increases and then drop sharply again a total of four times over the course of the measurement. As each scan took 20 seconds, the time between each drop varies between 20–23 minutes. Similarly, whilst not as obvious as at 3.34 THz, the intensity of the 3.36 THz mode also fluctuates over time. As seen before, the power increases before dropping suddenly multiple times throughout the measurement. As with the 3.34 THz mode, these drops occur 20–22 minutes apart.

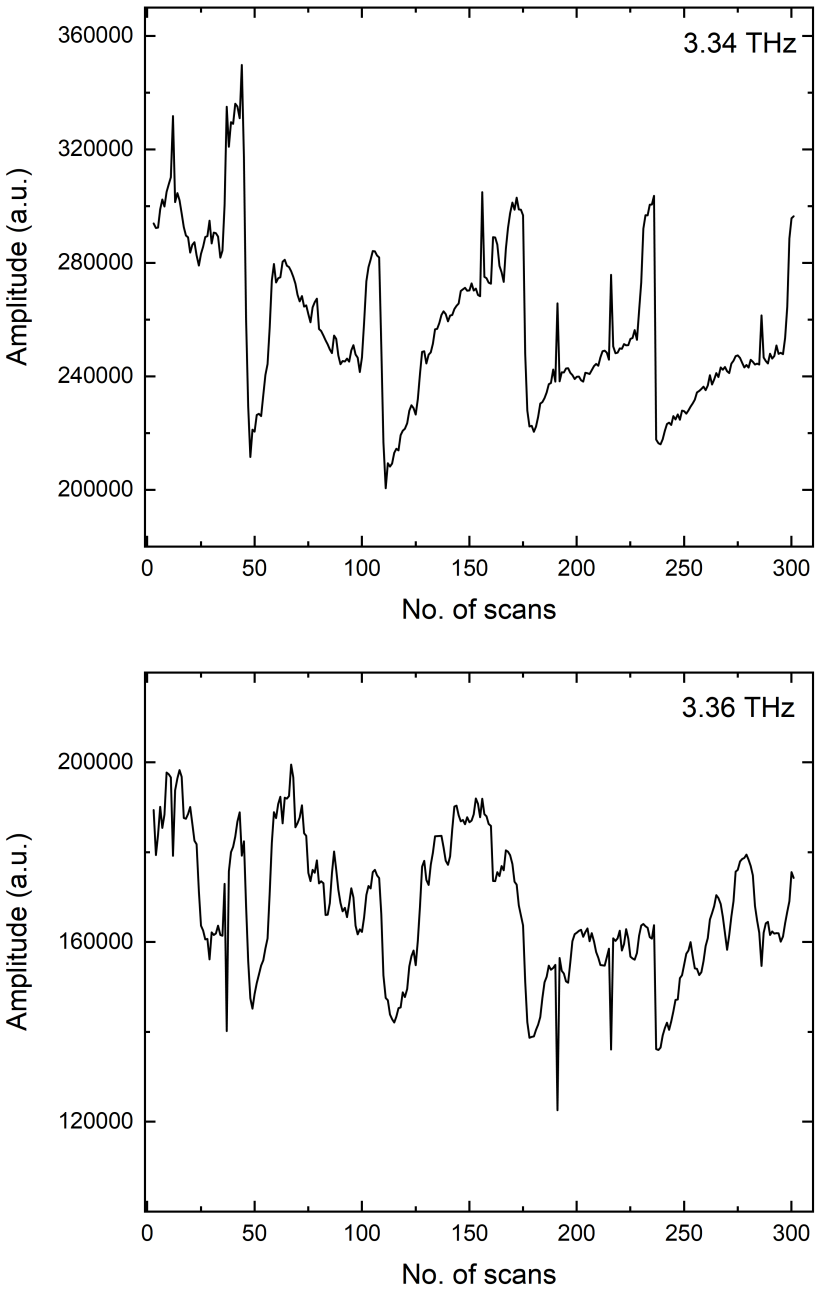

Figure 5.11: Power fluctuations of the 3.34 THz and 3.36 THz mode of Device A over 100 minutes.

5.5.1 Device B Power measurements

Device B was mounted into the cryostat of the FTIR set-up and multiple interferograms were recorded one minute apart. The QCL was driven at a current of 170 mA at a temperature of 10 K. The resulting contour plot is shown in Figure 5.12. What can be seen is that after 6 scans (6 minutes), a spontaneous mode hop occurs, whereby the initial active modes at 3.373 THz and 3.406 THz disappear and new modes at 3.374 THz and 3.407 THz appear. Similar to Device A, intensity fluc-

tuations occur. Pre-mode hope, the intensity of the modes is consistent. However, upon a mode hop the intensity of the 3.374 THz is weaker than the 3.407 THz mode.

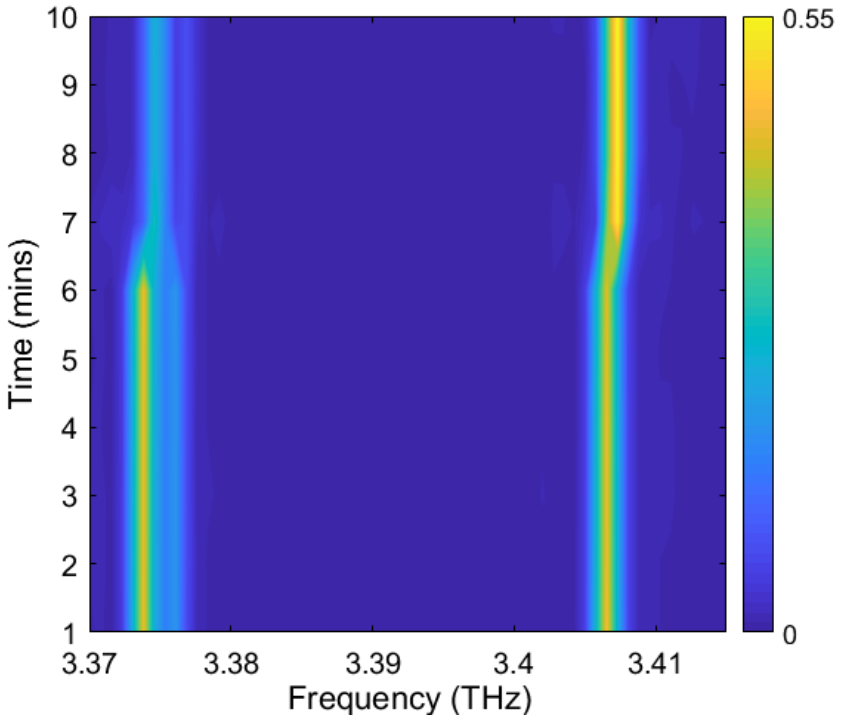

Figure 5.12: QCL emission spectra recorded at 170 mA at a QCL temperature of 10 K. Each spectrum was measured within a minute of each other. After scan 7, a mode hop occurs.

Figure 5.13 gives the output power of the 4 main modes of Device B over time. As with Device A, fluctuations in the output power are seen over time. Specifically, the power appears to increase before a sharp drop occurs. In this case, Device B exhibits less variations in the power compared with Device A. For the 3.373 THz and 3.406 THz modes prior to the mode hopping, a relative noise level of 1.53 % and 6.74 % respectively occurred. Post mode hopping, the power varies less, with a 2.00 % relative noise level over the 3.374 THz mode and 2.79 % for the 3.407 THz mode.

Whilst there doesn't seem to be as notable a pattern in the power fluctuations as was depicted in Figure 5.11a, it can be roughly estimated the time between sharp drops in power. For example, in Figure 5.13a, the time taken between scan 95 and scan 189 (where the next increase in power occurs) equates to a time of 31 minutes, a small increase to what was calculated for Device A. Again, for the 3.406 THz mode pre mode-hopping, the time between scan 169 and scan 253 is 28 minutes.

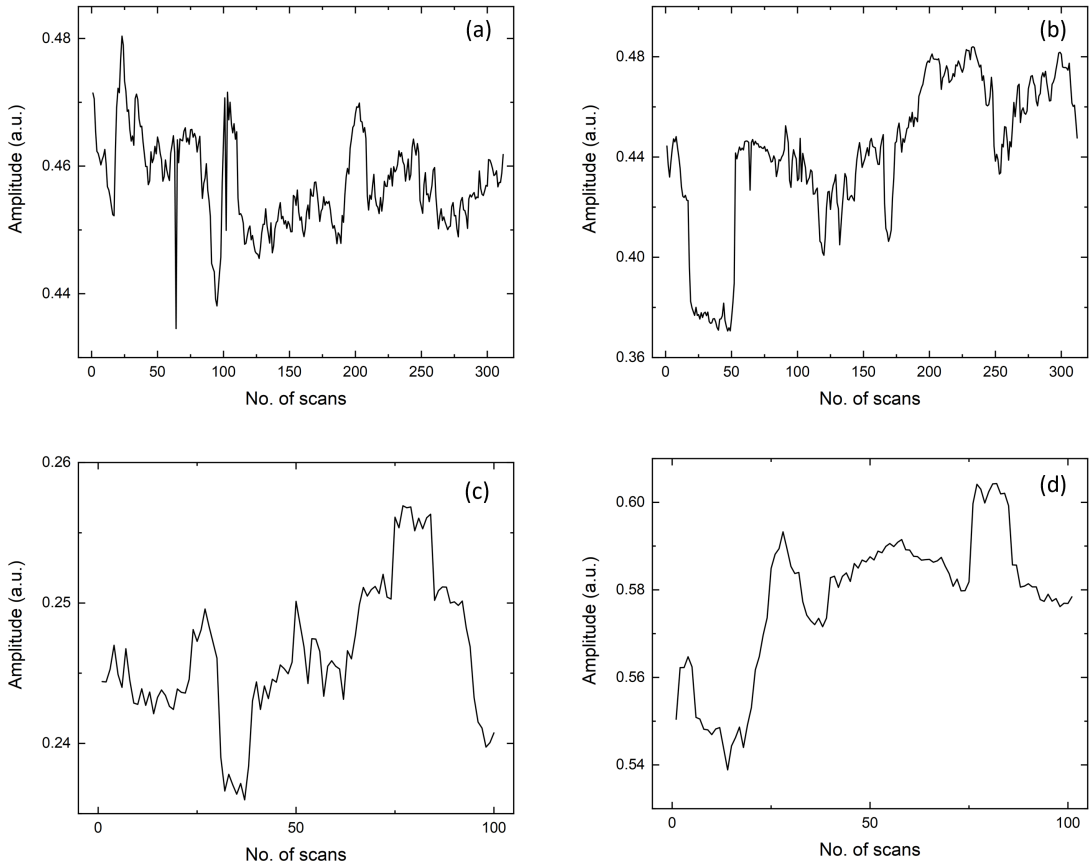

Figure 5.13: Output power of the active modes of the QCL pre mode hop (a) 3.37 THz, (b) 3.40 THz and post mode hop (c) 3.37 THz and (d) 3.40 THz.

A further investigation to what could cause the drop in power over a 20-30 minute time span led to measurements on the thermal environment in the laboratory. A test was conducted with the air-conditioning unit that supplies the laboratory. The unit was turned on and the liquid He cooled Si bolometer recorded the ambient noise in the room. This measurement was then repeated with the air-conditioning unit turned off. The results are shown in Figure 5.14. When the air-conditioning unit is turned on, the intensity of the ambient noise increases, with the noise standard deviation rising from 1.79×10^{-3} to 2.15×10^{-3}. As a result, it is highly likely that the air-conditioning being on it the laboratory can, to some extent, contribute to the power fluctuations seen from the QCL.

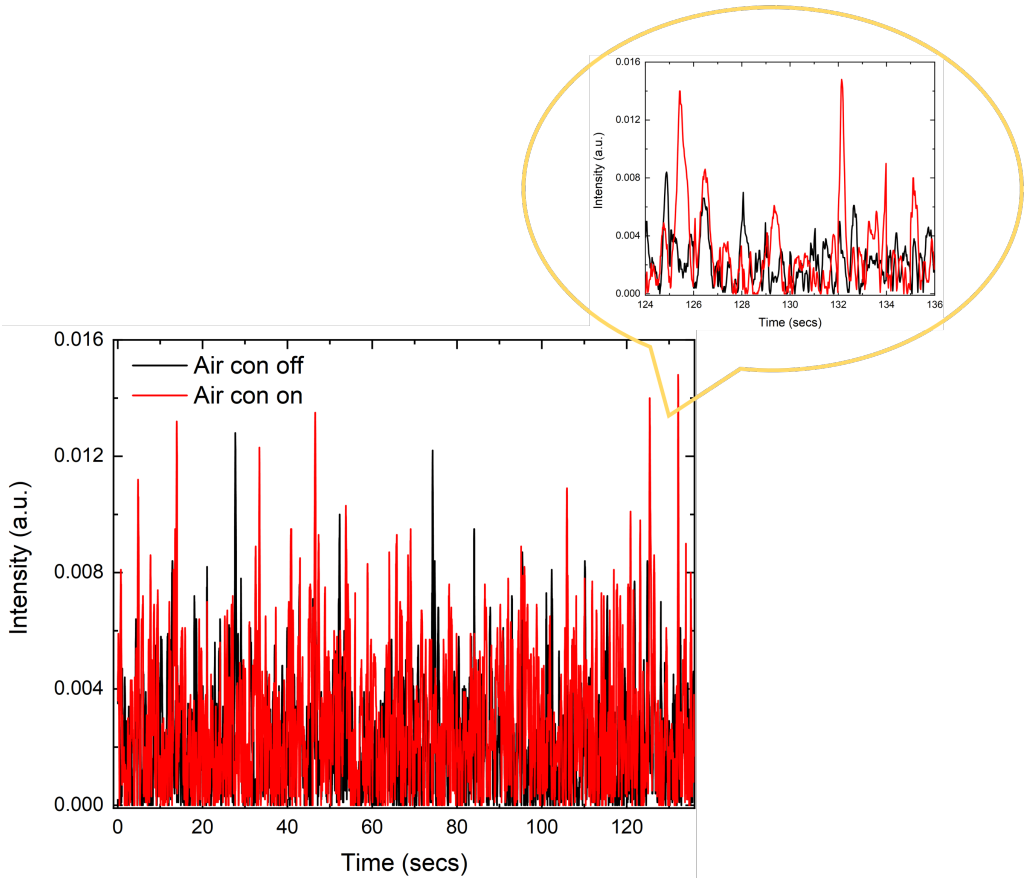

Figure 5.14: Measurement of the ambient noise in the laboratory with the air-conditioning unit turned on (red) and off (black).

5.6 Conclusion

In this chapter a working THz FTIR spectrometer has been demonstrated using various sampling methods. A cleaner spectrum has been obtained in comparison to that measured with the SM system. However, the results show that even with a different spectroscopic system that is likely to suffer from less optical feedback, the measurements still exhibits poor power stability. The QCL power appears to be more susceptible to thermal changes, e.g. with the air-conditioning turned on which the thermal detector will be more sensitive to. These measurements could, potentially, be improved significantly through the use of an electronic (as opposed to thermal) detector system. Whilst an alternate block integrated QCL was tested, power fluctuations still occurred, and a gas transmission spectrum could not be produced with a good enough certainty that the peaks were gas lines and not noise.

Chapter 6

Conclusion and further work

The motivation behind this work was to develop a THz QCL gas spectrometer, in order to contribute to the THz atmospheric and space field. Specifically, to provide instrumentation for the cataloguing of spectral lines and to lay the foundation for future work, including the incorporation of a multipass gas cell to reach a sensitivity that allows for trace gas detection. Additionally, this work gave more insight into the THz QCL itself and its suitability for spectral measurements, particularly as a LO in heterodyne spectroscopy for remote sensing.

The first experimental chapter is chapter 3. This chapter presents the various integration techniques that are available, before a discussion into the technique employed in this work, integrating the QCL into a metallic waveguide block with micromachined diagonal feedhorns, is given. This technique had a number of advantages over previous techniques. Including being mechanically robust and reproducible, this technique is also compact and minimal. Two devices were used in this work, both of which were grown from the same wafer and emit between 3 THz and 4 THz. A thorough study of these devices were done and they were shown to work in both pulsed and CW mode. A further device was characterised that emitted at >4.7 THz. This device exhibited a higher than expected thermal resistance, resulting in it being unable to operate in CW. This is most likely caused by imperfections in the thermal mounting. The near and far-field beam profiles of each device were characterised, and all three showed to display, to various extents, dual-lobe behaviour in the horizontal plane, meaning the active modes are spatially separated. The reason behind the beam pattern cannot be determined conclusively. However, a number of causes are likely to contribute, such as influence from the metallic waveguide, i.e. modes propagating through the waveguide channel and/or destructive interference occurring off the back facet of the QCL.

In chapter 4, SM spectroscopy was used with a THz QCL to measure D_2O, HDO, CH_3OH, and mixtures. Using this method, observations of gaseous species were demonstrated at various pressures. SM spectroscopy with a THz QCL has good potential for lab-based gas spectroscopy measurements, where its compact size, wide tunability and detector-free set-up is advantageous. The results however did highlight the need for further investigation into the QCL used. Fluctuations in the power, coupled with the complex feedback of multiple modes into the feedhorn led to the spectra exhibiting random peaks, data points with transmission values > 1, and some spectra did not show fully resolved absorption peaks at their expected frequencies.

Chapter 5 presented a different technique, FTIR spectroscopy. Preliminary results of the QCL emission was given. The results show that whilst the QCL emission spectrum produced was clearer than what was obtained through SM, that power fluctuations still occurred, and as such, the instability can not be attributed to the optical feedback that is required in the SM method. The likelihood of the instability arising from a thermal influence was investigated. It was found that the change in temperature of the room, along with the use of a thermal detector does partially contribute to the power instability.

Overall, the work in this project has laid the foundations for further research into utilising THz QCLs as a source for gas-phase spectroscopy. It has provided a gas spectroscopy system that, with the right QCL, has access to an unexploited region of the EM spectrum, meaning new gaseous lines can be measured and discovered. It has been concluded that the power instability arising from the multimode nature of the devices used, as well as thermal influence from the environment plays too significant a role to be ignored. Further research into the fabrication of the block integrated devices and the detector used must be done first before further gas spectroscopy measurements can be taken.

6.1 Further Work

Since the invention of the THz QCL, major advancements have been made which have firmly established it as an ideal choice when requiring a laser that is high-powered, narrowband, and compact for a wide scope of applications. Over the years, the improvements made to the operating temperature, frequency range, and current threshold have improved their usability and with further work on developing different active region designs and waveguides, room temperature operation may be achievable, increasing the number of applications THz QCLs can be used in.

For THz QCLs to be considered as a laser source for gas-phase spectroscopy or as a LO in heterodyne spectroscopy, further investigations on the power fluctuations must be done. Preliminary results of power-locking a THz QCL via integrating the device with a racetrack resonator within a waveguide cavity has already been published [161], and would provide a solution to the issues mentioned in this work.

Recently, a custom ColdEdge closed cycle cryocooler CH204N with a low vibration interface has been installed into the laboratory to replace the Janis ST-100 cryostat used in the measurements presented in chapters 4 and 5. Here, the cryocooler recycles the He required to cool down the QCL. This will hopefully compensate for some of the QCL power issues. A closed cycle cryocooler would remove the possibility of a change in He flow rate, which may result in a variation in the pressure. The change in pressure could cause the temperature of the QCL to fluctuate and in turn, cause the output power to vary. In addition to the installation of a closed cycle cryocooler, the gas spectroscopy laboratory has also employed a TERAFET electrical detector to replace the bolometer (thermal detector) that was used for the experiments in this project [162]. The electrical detector ignores fluctuations in the room temperature e.g. from air-conditioning. Furthermore, frequency-locking the QCL can also aid in stabilising the laser. This can be done through various methods, including locking to a known atomic/molecular line [163].

Additionally, improvements to the QCL block design can be made. With an improvement in machine tolerance, a smaller channel with a conical feedhorn could be fabricated. This would improve the beam quality as well as make progression towards the first THz fundamental waveguide. With these refinements, along with single mode operation (as opposed to the multimode devices used in this project),THz QCL could potentially be used as LO in combination with a mixer to create a fully remote sensing system capable of heterodyne spectroscopy [46, 47].

Although spectral lines from reactants and products are distinguishable in the measured data, with a more suitable THz QCL, significant improvements in sensitivity can be expected by introducing a multi-pass gas cell or employing a cavity-enhanced technique. This will increase the sensitivity of the system, and allow for conditions that are found in our atmosphere and space to be replicated. Another avenue of THz gas-phase spectroscopy that is yet to be investigated is photolysis reactions [164]. Many atmospheric and space reactions are initiated via photolysis and it will be interesting to see the resulting THz gas spectra. For example, atomic O (Section 1.4). Addressing the power and operating temperature of a THz QCL will also allow for field measurements to be considered.

Bibliography

[1] M. Hauser, R. Arendt, T. Kelsall, E. Dwek, N. Odegard, J. Weiland, H. Freudenreich, W. Reach, R. Silverberg, S. Moseley, Y. Pei, P. Lubin, J. Mather, R. Shafer, G. Smoot, R. Weiss, D. Wilkinson, and E. Wright, " The COBE Diffuse Infrared Background Experiment Search for the Cosmic Infrared Background. I. Limits and Detections," *The Astrophysical Journal*, vol. 508, no. 1, pp. 25–43, Nov. 1998.

[2] N. Trentham, J. Kormendy, and D. B. Sanders, "Hubble Space Telescope Ultraviolet Spectral Energy Distributions for Three Ultraluminous Infrared Galaxies," *The Astronomical Journal*, vol. 117, no. 5, pp. 2152–2167, May 1999.

[3] D. T. Leisawitz, W. C. Danchi, M. J. DiPirro, L. D. Feinberg, D. Y. Gezari, M. Hagopian, W. D. Langer, J. C. Mather, S. H. Moseley Jr., M. Shao, R. F. Silverberg, J. G. Staguhn, M. R. Swain, H. W. Yorke, and X. Zhang, "Scientific motivation and technology requirements for the SPIRIT and SPECS far-infrared/submillimeter space interferometers," in *Astronomical Telescopes and Instrumentation*, J. B. Breckinridge and P. Jakobsen, Eds., vol. 4013, Munich: UV, Optical, IR Space Telescopes, and Instruments, Jul. 2000, pp. 36–46.

[4] W. M. O. (WMO), "WMO Greenhouse Gas Bulletin (GHG Bulletin) - No. 15," Geneva, Tech. Rep., 2019.

[5] Core Writing Team, R. Pachauri, and L. Meyer, "Climate Change 2014: Synthesis Report. Contribution of Working Groups I,II,III to the Fifth Assesment Report of the Intergovernmental Panel on Climate Change," IPCC, Geneva, Tech. Rep., 2014, p. 151.

[6] I. Newton, "A Letter of Mr. Isaac Newton ... containing his New Theory about Light and Colors," *Philosophical Transactions of the Royal Society*, vol. 80, pp. 3075–3087, 1672.

[7] W. Wollaston, "XII. A method of examining refractive and dispersive powers, by prismatic reflection," *Philosophical Transactions of the Royal Society of London*, vol. 92, pp. 365–380, Dec. 1802.

[8] J. Fraunhofer, "Determination of the refractive and color-dispersing power of different types of glass, in relation to the improvement of achromatic telescopes," *Annalen der Physik*, vol. 56, pp. 264–313, 1817.

[9] J. F. W. Herschel, "XXXI. On the Absorption of Light by Coloured Media, and on the Colours of the Prismatic Spectrum exhibited by certain Flames; with an Account of a ready Mode of determining the absolute dispersive Power of any Medium, by direct experiment," *Earth and Environmental Science Transactions of The Royal Society of Edinburgh*, vol. 9, no. 2, pp. 445–460, 1823.

[10] G. Kirchhoff, "Ueber die Fraunhoferschen Linien," *Monatsberichte der Königliche Preussische Akademie der Wissenschaften zu Berlin*, pp. 662–665, 1860.

[11] N. Bohr, "On the Constitution of Atoms and Molecules," *Philosophical Magazine*, vol. 26, no. 1, 1913.

[12] J. Hamilton and A. C. Lewis, "Chromatographic Methods," in *Analytical Techniques for Atmospheric Measurement*, D. E. Heard, Ed., 1st Editio, Oxford: Blackwell Publishing Inc., 2006, ch. 8, pp. 361–402.

[13] T. H. Maiman, "Stimulated Optical Radiation in Ruby," *Nature*, vol. 187, no. 4736, pp. 493–494, 1960.

[14] E. C. Wood and R. C. Cohen, "Fluorescence Methods," in *Analytical Techniques for Atmospheric Measurement*, D. Heard, Ed., 1st Editio, Oxford: Springer, Oct. 2006, ch. 4, pp. 189–224.

[15] P. Atkins, J. De Paula, and J. Keeler, *Atkin's Physical Chemistry*, Eleventh. Oxford University Press, 2017, p. 578.

[16] B. S. Williams, "Terahertz quantum cascade lasers," PhD thesis, Massachusetts Institute of Technology, Massachusetts, Aug. 2003.

[17] K. Liu, L. Wang, T. Tan, G. Wang, W. Zhang, W. Chen, and X. Gao, "Highly sensitive detection of methane by near-infrared laser absorption spectroscopy using a compact dense-pattern multipass cell," *Sensors and Actuators B: Chemical*, vol. 220, pp. 1000–1005, Dec. 2015.

[18] D. Nelson, J. Shorter, J. McManus, and M. Zahniser, "Sub-part-per-billion detection of nitric oxide in air using a thermoelectrically cooled mid-infrared quantum cascade laser spectrometer," *Applied Physics B: Lasers and Optics*, vol. 75, no. 2-3, pp. 343–350, Sep. 2002.

[19] I. Mappé, L. Joly, G. Durry, X. Thomas, T. Decarpenterie, J. Cousin, N. Dumelie, E. Roth, A. Chakir, and P. G. Grillon, "A quantum cascade laser absorption spectrometer devoted to the in situ measurement of atmospheric N2O and CH4 emission fluxes," *Review of Scientific Instruments*, vol. 84, no. 2, p. 023 103, Feb. 2013.

[20] J. U. White, "Long Optical Paths of Large Aperture," *Journal of the Optical Society of America*, vol. 32, no. 5, p. 285, May 1942.

[21] D. Herriott, H. Kogelnik, and R. Kompfner, "Off-Axis Paths in Spherical Mirror Interferometers," *Applied Optics*, vol. 3, no. 4, p. 523, Apr. 1964.

[22] D. R. Herriott and H. J. Schulte, "Folded Optical Delay Lines," *Applied Optics*, vol. 4, no. 8, pp. 883–889, Aug. 1965.

[23] R. Liu, M. He, R. Su, Y. Yu, W. Qi, and Z. He, "Insulin amyloid fibrillation studied by terahertz spectroscopy and other biophysical methods," *Biochemical and Biophysical Research Communications*, vol. 391, no. 1, pp. 862–867, Jan. 2010.

[24] W. Zhang, E. R. Brown, M. Rahman, and M. L. Norton, "Observation of terahertz absorption signatures in microliter DNA solutions," *Applied Physics Letters*, vol. 102, no. 023701, pp. 1–4, Jan. 2013.

[25] A. G. Davies, A. D. Burnett, W. Fan, E. H. Linfield, and J. E. Cunningham, "Terahertz spectroscopy of explosives and drugs," *Materials Today*, vol. 11, no. 3, pp. 18–26, Mar. 2008.

[26] G. Tzydynzhapov, P. Gusikhin, V. Muravev, A. Dremin, Y. Nefyodov, and I. Kukushkin, "New Real-Time Sub-Terahertz Security Body Scanner," *Journal of Infrared, Millimeter, and Terahertz Waves*, vol. 41, no. 6, pp. 632–641, Jun. 2020.

[27] J. A. Zeitler, Y. Shen, C. Baker, P. F. Taday, M. Pepper, and T. Rades, "Analysis of coating structures and interfaces in solid oral dosage forms by three dimensional terahertz pulsed imaging," *Journal of Pharmaceutical Sciences*, vol. 96, no. 2, pp. 330–340, Feb. 2007.

[28] K. Su, Y.-C. Shen, and J. A. Zeitler, "Terahertz Sensor for Non-Contact Thickness and Quality Measurement of Automobile Paints of Varying Complexity," *IEEE Transactions on Terahertz Science and Technology*, vol. 4, no. 4, pp. 432–439, Jul. 2014.

[29] X. Yang, X. Zhao, K. Yang, Y. Liu, Y. Liu, W. Fu, and Y. Luo, "Biomedical Applications of Terahertz Spectroscopy and Imaging," *Trends in Biotechnology*, vol. 34, no. 10, pp. 810–824, Oct. 2016.

[30] P. C. Ashworth, E. Pickwell-MacPherson, E. Provenzano, S. E. Pinder, A. D. Purushotham, M. Pepper, and V. P. Wallace, "Terahertz pulsed spectroscopy of freshly excised human breast cancer," *Optics Express*, vol. 17, no. 15, p. 12 444, Jul. 2009.

[31] E. B. Moon, T. I. Jeon, and D. R. Grischkowsky, "Long-Path THz-TDS Atmospheric Measurements between Buildings," *IEEE Transactions on Terahertz Science and Technology*, vol. 5, no. 5, pp. 742–750, Sep. 2015.

[32] T. Nagatsuma, G. Ducournau, and C. C. Renaud, "Advances in terahertz communications accelerated by photonics," *Nature Photonics*, vol. 10, no. 6, pp. 371–379, May 2016.

[33] P. Arias, N. Bellouin, E. Coppola, R. Jones, G. Krinner, J. Marotzke, V. Naik, M. Palmer, G.-K. Plattner, J. Rogelj, M. Rojas, J. Sillmann, T. Storelvmo, P. Thorne, B. Trewin, K. A. Rao, B. Adhikary, R. Allan, K. Armour, G. Bala, R. Barimalala, S. Berger, J. Canadell, C. Cassou, A. Cherchi, W. Collins, W. Collins, S. Connors, S. Corti, F. Cruz, F. Dentener, C. Dereczynski, A. D. Luca, A. D. Niang, F. Doblas-Reyes, A. Dosio, H. Douville, F. Engelbrecht, V. Eyring, E. Fischer, P. Forster, B. Fox-Kemper, J. Fuglestvedt, J. Fyfe, N. Gillett, L. Goldfarb, I. Gorodetskaya, J. Gutierrez, R. Hamdi, E. Hawkins, H. Hewitt, P. Hope, A. Islam, C. Jones, D. Kaufman, R. Kopp, Y. Kosaka, J. Kossin, S. Krakovska, J.-Y. Lee, J. Li, T. Mauritsen, T. Maycock, M. Meinshausen, S.-K. Min, P. Monteiro, T. Ngo-Duc, F. Otto, I. Pinto, A. Pirani, K. Raghavan, R. Ranasinghe, A. Ruane, L. Ruiz, J.-B. Sallée, B. Samset, S. Sathyendranath, S. Seneviratne, A. Sörensson, S. Szopa, I. Takayabu, A.-M. Tréguier, B. v. d. Hurk, R. Vautard, K. v. Schuckmann, S. Zaehle, X. Zhang, and K. Zickfeld, "Climate Change 2021: The Physical Science Basis. Contribution of Working Group I to the Sixth Assessment Report of the Intergovernmental Panel on Climate Change," Cambridge, Tech. Rep., 2021, pp. 33–144.

[34] N. Anderson, R. Strader, and C. Davidson, "Airborne reduced nitrogen: ammonia emissions from agriculture and other sources," *Environment International*, vol. 29, no. 2-3, pp. 277–286, Jun. 2003.

[35] I. E. Gordon, L. S. Rothman, C. Hill, R. V. Kochanov, Y. Tan, P. F. Bernath, M. Birk, V. Boudon, A. Campargue, K. V. Chance, B. J. Drouin, J. M. Flaud, R. R. Gamache, J. T. Hodges, D. Jacquemart, V. I. Perevalov, A. Perrin, K. P. Shine, M. A. Smith, J. Tennyson, G. C. Toon, H. Tran, V. G. Tyuterev, A. Barbe, A. G. Császár, V. M. Devi, T. Furtenbacher, J. J. Harrison, J. M. Hartmann, A. Jolly, T. J. Johnson, T. Karman, I. Kleiner, A. A. Kyuberis, J. Loos, O. M. Lyulin, S. T. Massie, S. N. Mikhailenko, N. Moazzen-Ahmadi, H. S. Müller, O. V. Naumenko, A. V. Nikitin, O. L. Polyansky, M. Rey, M. Rotger, S. W. Sharpe, K. Sung, E. Starikova, S. A. Tashkun, J. V. Auwera, G. Wagner, J. Wilzewski, P. Wcisło, S. Yu, and E. J. Zak, "The HITRAN2016 molecular spectroscopic database," *Journal of Quantitative Spectroscopy and Radiative Transfer*, vol. 203, pp. 3–69, Dec. 2017.

[36] C. Kulesa, "Terahertz spectroscopy for astronomy: From comets to cosmology," *IEEE Transactions on Terahertz Science and Technology*, vol. 1, no. 1, pp. 232–240, Sep. 2011.

[37] C. K. Walker, "The Interstellar Medium (ISM) at Terahertz (THz) Frequencies," in *Terahertz Astronomy*, First Edit, Boca Raton: CRC Press, Oct. 2015, ch. 1, pp. 1–35.

[38] F. P. Keenan, D. J. Lennon, C. T. Johnson, and A. E. Kingston, "Fine-structure population ratios for the 2P ground state of C II," *Monthly Notices of the Royal Astronomical Society*, vol. 220, no. 3, pp. 571–576, Jun. 1986.

[39] L. R. Zink, K. M. Evenson, F. Matsushima, T. Nelis, and R. L. Robinson, "Atomic oxygen fine-structure splittings with tunable far-infrared spectroscopy," *The Astrophysical Journal*, vol. 371, p. L85, Apr. 1991.

[40] H. Pickett, B. Drouin, E. Cohen, and J. Pearson, "Submillimeter, Millimeter, and Microwave Spectral Line Catalog," *J. Quant. Spectrosc. & Rad. Transfer*, vol. 60, pp. 883–890, 1998.

[41] H. Hirashita, P. M. Koch, S. Matsushita, S. Takakuwa, M. Nakamura, K. Asada, H. B. Liu, Y. Urata, M.-J. Wang, W.-H. Wang, S. Takahashi, Y.-W. Tang, H.-H. Chang, K. Huang, O. Morata, M. Otsuka, K.-Y. Lin, A.-L. Tsai, Y.-T. Lin, S. Srinivasan, P. Martin-Cocher, H.-Y. Pu, F. Kemper, N. Patel, P. Grimes, Y.-D. Huang, C.-C. Han, Y.-R. Huang, H. Nishioka, L. C.-C. Lin, Q. Zhang, E. Keto, R. Burgos, M.-T. Chen, M. Inoue, and P. T. P. Ho, "First-generation science cases for ground-based terahertz telescopes," *Publications of the Astronomical Society of Japan*, vol. 68, no. 1, pp. 1–41, Feb. 2016.

[42] P. Tremblin, V. Minier, N. Schneider, G. A. Durand, M. C. B. Ashley, J. S. Lawrence, D. M. Luong-Van, J. W. V. Storey, G. A. Durand, Y. Reinert, C. Veyssiere, C. Walter, P. Ade, P. G. Calisse, Z. Challita, E. Fossat, L. Sabbatini, A. Pellegrini, P. Ricaud, and J. Urban, "Site testing for submillimetre astronomy at Dome C, Antarctica," *Astronomy & Astrophysics*, vol. 535, p. 112, Nov. 2011.

[43] J. R. Silva, B. Mirzaei, W. Laauwen, Q. Hu, C. E. Groppi, C. Walker, J.-R. Gao, N. More, A. Young, A. Khalatpour, and C. Kulesa, "42 HEB receiver at 4.7 THz for GUSTO," in *Millimeter, Submillimeter, and Far-Infrared Detectors and Instrumentation for Astronomy IX*, J. Zmuidzinas and J.-R. Gao, Eds., SPIE, Jul. 2018, p. 33.

[44] L Rezac, P Hartogh, R Güsten, H Wiesemeyer, H.-W Hübers, C Jarchow, H Richter, B Klein, and N Honingh, "First detection of the 63 $$m atomic oxygen line in the thermosphere of Mars with GREAT/SOFIA," *Astronomy & Astrophysics*, vol. 580, p. 10, 2015.

[45] J. Waters, L. Froidevaux, R. Harwood, R. Jarnot, H. Pickett, W. Read, P. Siegel, R. Cofield, M. Filipiak, D. Flower, J. Holden, G. Lau, N. Livesey, G. Manney, H. Pumphrey, M. Santee, D. Wu, D. Cuddy, R. Lay, M. Loo, V. Perun, M. Schwartz, P. Stek, R. Thurstans, M. Boyles, K. Chandra, M.

Chavez, Gun-Shing Chen, B. Chudasama, R. Dodge, R. Fuller, M. Girard, J. Jiang, Yibo Jiang, B. Knosp, R. LaBelle, J. Lam, K. Lee, D. Miller, J. Oswald, N. Patel, D. Pukala, O. Quintero, D. Scaff, W. Van Snyder, M. Tope, P. Wagner, and M. Walch, "The Earth observing system microwave limb sounder (EOS MLS) on the aura Satellite," *IEEE Transactions on Geoscience and Remote Sensing*, vol. 44, no. 5, pp. 1075–1092, May 2006.

[46] G. Savini, D. Brooks, L. Zhu, B. Ellison, O. Auriacombe, T. Bradshaw, M. Crook, D. Gerber, M. Henry, T. Rawlings, H. Wang, J. Charlton, S. M. Tun, M. Emes, T. Hunt, B. Winter, E. Linfield, G. Davies, A. Valavanis, S. Parkes, D. Walker, and G. Yu, "Recent progress in the Elegant Breadboard supra-THz activities for LOCUS and a view to an astronomy application," in *Proceedings of IEEE 9th UK-Europe-China Workshop on Millimetre Waves and Terahertz Technologies, UCMMT 2016*, Institute of Electrical and Electronics Engineers Inc., Mar. 2017, pp. 1–5.

[47] S. P. Rea, B. N. Ellison, B Swinyard, A Valavanis, Y Han, E. H. Linfield, A. G. Davies, C Saunders, S Parkes, D Gerber, M Henry, H Wang, B Alderman, O Auriacombe, T Rawlings, M Crooke, and T Bradshaw, "The Low-Cost Upper-Atmosphere Sounder (LOCUS)," in *26th International Symposium on Space Terahertz Technology (ISSTT 2015)*, Cambridge, 2015, pp. 16–18.

[48] R. M. Smith and M. A. Arnold, "Selectivity of Terahertz Gas-Phase Spectroscopy," *Analytical Chemistry*, vol. 87, no. 21, pp. 10 679–10 683, Nov. 2015.

[49] S. Kasap, *Optoelectronics and Photonics: Principles and Practices*, 2nd. Pearson, 2013, p. 550.

[50] D. H. Auston, K. P. Cheung, and P. R. Smith, "Picosecond photoconducting Hertzian dipoles," *Applied Physics Letters*, vol. 45, no. 3, p. 284, Jun. 1984.

[51] B. B. Hu, X. Zhang, D. H. Auston, and P. R. Smith, "Free-space radiation from electro-optic crystals," *Applied Physics Letters*, vol. 56, no. 6, p. 506, Jun. 1989.

[52] F. Lewen, E. Michael, R. Gendriesch, J. Stutzki, and G. Winnewisser, "Terahertz Laser Sideband Spectroscopy with Backward Wave Oscillators," *Journal of Molecular Spectroscopy*, vol. 183, no. 1, pp. 207–209, 1997.

[53] V. L. Bratman, Y. K. Kalynov, and V. N. Manuilov, "Large-orbit gyrotron operation in the terahertz frequency range," *Physical Review Letters*, vol. 102, no. 24, p. 245 101, Jun. 2009.

[54] T. Y. Chang, T. J. Bridges, and E. G. Burkhardt, "CW submillimeter laser action in optically pumped methyl fluoride, methyl alcohol, and vinyl chloride gases," *Applied Physics Letters*, vol. 17, no. 6, p. 249, Oct. 1970.

[55] H. Hirose and S. Kon, "Compact, High-Power FIR NH3 Laser Pumped in a CO2 Laser Cavity," *IEEE Journal of Quantum Electronics*, vol. 22, no. 9, pp. 1600–1603, 1986.

[56] C. T. Gross, J. Kiess, A. Mayer, and F. Keilmann, "Regular Papers Pulsed High-Power Far-Infrared Gas Lasers: Performance and Spectral Survey," *IEEE Journal of Quantum Electronics*, vol. 23, no. 4, pp. 377–384, 1987.

[57] A. Pagies, G. Ducournau, and J.-F. Lampin, "Low-threshold terahertz molecular laser optically pumped by a quantum cascade laser," *APL Photonics*, vol. 1, no. 3, p. 031 302, Jun. 2016.

[58] A. Maestrini, J. Ward, J. Gill, H. Javadi, E. Schlecht, G. Chattopadhyay, F. Maiwald, N. R. Erickson, and I. Mehdi, "A 1.7-1.9 THz local oscillator source," *IEEE Microwave and Wireless Components Letters*, vol. 14, no. 6, pp. 253–255, Jun. 2004.

[59] N. Orihashi, S. Suzuki, and M. Asada, "One THz harmonic oscillation of resonant tunneling diodes," *Applied Physics Letters*, vol. 87, no. 23, p. 233 501, Nov. 2005.

[60] J. V. Siles and J. Grajal, "Physics-based design and optimization of Schottky diode frequency multipliers for terahertz applications," *IEEE Transactions on Microwave Theory and Techniques*, vol. 58, no. 7, pp. 1933–1942, Jul. 2010.

[61] R. A. Lewis, "A review of terahertz detectors," *Journal of Physics D: Applied Physics*, vol. 52, no. 43, p. 433 001, Aug. 2019.

[62] Y. C. Shen, P. C. Upadhya, H. E. Beere, E. H. Linfield, A. G. Davies, I. S. Gregory, C. Baker, W. R. Tribe, and M. J. Evans, "Generation and detection of ultrabroadband terahertz radiation using photoconductive emitters and receivers," *Applied Physics Letters*, vol. 85, no. 2, pp. 164–166, Jul. 2004.

[63] D. H. Auston and M. C. Nuss, "Electrooptic Generation and Detection of Femtosecond Electrical Transients," *IEEE Journal of Quantum Electronics*, vol. 24, no. 2, pp. 184–197, 1988.

[64] L. O. Fernandes, P. Kaufmann, R. Marcon, A. S. Kudaka, A. Marun, R. Godoy, E. C. Bortolucci, M. B. Zakia, and J. A. Diniz, "Photometry of THz radiation using Golay cell detector," in *30th URSI General Assembly and Scientific Symposium*, Rome, 2011.

[65] S. A. Kuznetsov, A. G. Paulish, M. Navarro-Ciá, and A. V. Arzhannikov, "Selective Pyroelectric Detection of Millimetre Waves Using Ultra-Thin Metasurface Absorbers," *Scientific Reports*, vol. 6, no. 1, pp. 1–11, Feb. 2016.

[66] P. L. Richards, "Bolometers for infrared and millimeter waves," *Journal of Applied Physics*, vol. 76, no. 1, pp. 1–24, Jul. 1994.

[67] A. M. Cowley and H. O. Sorensen, "Quantitative Comparison of Solid-State Microwave Detectors," *IEEE Transactions on Microwave Theory and Techniques*, vol. 14, no. 12, pp. 588–602, 1966.

[68] R. F. Kazarinov and R. A. Suris, "Possible amplification of electromagnetic waves in a semiconductor with a superlattice," *Soviet Physycs. Semiconductors*, vol. 5, pp. 707–709, 1971.

[69] J. Faist, F. Capasso, D. L. Sivco, C. Sirtori, A. L. Hutchinson, and A. Y. Cho, "Quantum Cascade Laser," *Science*, vol. 235, no. 4785, pp. 172–176, Apr. 1994.

[70] B. S. Williams, "Terahertz quantum-cascade lasers," *Nature Photonics*, vol. 1, no. 9, pp. 517–525, Sep. 2007.

[71] R. Köhler, A. Tredicucci, F. Beltram, H. E. Beere, E. H. Linfield, A. G. Davies, D. A. Ritchie, R. C. Iotti, and F. Rossi, "Terahertz semiconductor-heterostructure laser," *Nature*, vol. 417, no. 6885, pp. 156–159, May 2002.

[72] A. Y. Cho and J. R. Arthur, "Molecular beam epitaxy," *Progress in Solid State Chemistry*, vol. 10, no. 3, pp. 157–191, Jan. 1975.

[73] D. G. Revin, L. R. Wilson, E. A. Zibik, R. P. Green, J. W. Cockburn, M. J. Steer, R. J. Airey, and M. Hopkinson, "InGaAs/AIAsSb quantum cascade lasers," *Applied Physics Letters*, vol. 85, no. 18, pp. 3992–3994, Nov. 2004.

[74] P. Dean, A. Valavanis, J. Keeley, K. Bertling, Y. L. Lim, R. Alhathlool, A. D. Burnett, L. H. Li, S. P. Khanna, D. Indjin, T. Taimre, A. D. Rakić, E. H. Linfield, and A. G. Davies, "Terahertz imaging using quantum cascade lasers - A review of systems and applications," *Journal of Physics D: Applied Physics*, vol. 47, no. 37, p. 374 008, Sep. 2014.

[75] Z Chen, Z. Y. Tan, Y. J. Han, R Zhang, X. G. Guo, H Li, J. C. Cao, and H. C. Liu, "Wireless communication demonstration at 4.1 THz using quantum cascade laser and quantum well photodetector," *Electronics Letters*, vol. 47, no. 17, pp. 1002–1004, Aug. 2011.

[76] H.-W. Hübers, H. Richter, and M. Wienold, "High-resolution terahertz spectroscopy with quantum-cascade lasers," *Journal of Applied Physics*, vol. 125, no. 15, p. 151 401, Apr. 2019.

[77] J. Faist, M. Beck, T. Aellen, and E. Gini, "Quantum-cascade lasers based on a bound-to-continuum transition," *Applied Physics Letters*, vol. 78, no. 2, p. 147, Jan. 2001.

[78] G. Scalari, L. Ajili, J. Faist, H. Beere, E. Linfield, D. Ritchie, and G. Davies, "Far-infrared (λ=87 μm) bound-to-continuum quantum-cascade lasers operating up to 90 K," *Applied Physics Letters*, vol. 82, no. 19, p. 3165, May 2003.

[79] B. S. Williams, H. Callebaut, S. Kumar, Q. Hu, and J. L. Reno, "3.4-THz quantum cascade laser based on longitudinal-optical-phonon scattering for depopulation," *Applied Physics Letters*, vol. 82, no. 7, p. 1015, Feb. 2003.

[80] A. Y. Cho, J. Faist, D. L. Sivco, F. Capasso, C. Gmachl, C. Sirtori, and A. L. Hutchinson, "Long-wavelength (λ = 8–11.5 m) semiconductor lasers with waveguides based on surface plasmons," *Optics Letters, Vol. 23, Issue 17, pp. 1366-1368*, vol. 23, no. 17, pp. 1366–1368, Sep. 1998.

[81] B. S. Williams, S. Kumar, H. Callebaut, Q. Hu, and J. L. Reno, "Terahertz quantum-cascade laser at λ =100μm using metal waveguide for mode confinement," *Applied Physics Letters*, vol. 83, no. 11, pp. 2124–2126, Sep. 2003.

[82] A. J. Adam, I. Kašalynas, J. N. Hovenier, T. O. Klaassen, J. R. Gao, E. E. Orlova, B. S. Williams, S. Kumar, Q. Hu, and J. L. Reno, "Beam patterns of terahertz quantum cascade lasers with subwavelength cavity dimensions," *Applied Physics Letters*, vol. 88, no. 15, p. 151 105, Apr. 2006.

[83] J. Faist, C. Gmachl, and F. Capasso, "Distributed feedback quantum cascade lasers," *Applied Physics Letters*, vol. 70, no. 20, p. 2672, 1997.

[84] C. Gmachl, F. Capasso, J. Faist, A. L. Hutchinson, A. Tredicucci, D. L. Sivco, J. N. Baillargeon, S. N. G. Chu, A. Y. Cho, C. Gmachl, F. Capasso, J. Faist, A. L. Hutchinson, A. Tredicucci, D. L. Sivco, J. N. Baillargeon, S. N. G. Chu, and A. Y. Cho, "Continuous-wave and high-power pulsed operation of index-coupled distributed feedback quantum cascade laser at λ=8.5 μm," *Applied Physics Letters*, vol. 72, no. 12, p. 1430, 1998.

[85] D. Hofstetter, J. Faist, M. Beck, and U. Oesterle, "Surface-emitting 10.1 μm quantum-cascade distributed feedback lasers," *Applied Physics Letters*, vol. 75, no. 24, p. 3769, Dec. 1999.

[86] C. Walther, G. Scalari, J. Faist, H. Beere, and D. Ritchie, "Low frequency terahertz quantum cascade laser operating from 1.6 to 1.8THz," *Applied Physics Letters*, vol. 89, no. 23, p. 231 121, 2006.

[87] H. C. Liu, M. Wächter, D. Ban, Z. R. Wasilewski, M. Buchanan, G. C. Aers, J. C. Cao, S. L. Feng, B. S. Williams, and Q. Hu, "Effect of doping concentration on the performance of terahertz quantum-cascade lasers," *Applied Physics Letters*, vol. 87, no. 14, p. 141 102, Sep. 2005.

[88] B. S. Williams, H. Callebaut, S. Kumar, Q. Hu, and J. L. Reno, "3.4-THz quantum cascade laser based on longitudinal-optical-phonon scattering for depopulation," *Applied Physics Letters*, vol. 82, no. 7, pp. 1015–1017, 2003.

[89] A. Khalatpour, M. C. Tam, S. J. Addamane, J. Reno, Z. Wasilewski, and Q. Hu, "Terahertz semiconductor laser source at -12 C," *Applied Physics*, Nov. 2022.

[90] M. Wienold, B. Röben, L. Schrottke, R. Sharma, A. Tahraoui, K. Biermann, and H. T. Grahn, "High-temperature, continuous-wave operation of terahertz quantum-cascade lasers with metal-metal waveguides and third-order distributed feedback," *Optics Express*, vol. 22, no. 3, p. 3334, Feb. 2014.

[91] L. Li, L Chen, J. Freeman, M Salih, P Dean, A. Davies, and E. Linfield, "Multi-Watt high-power THz frequency quantum cascade lasers," *Electronics Letters*, vol. 53, no. 12, pp. 799–800, 2017.

[92] X. Wang, C. Shen, T. Jiang, Z. Zhan, Q. Deng, W. Li, W. Wu, N. Yang, W. Chu, and S. Duan, "High-power terahertz quantum cascade lasers with 0.23 W in continuous wave mode," *AIP Advances*, vol. 6, no. 7, p. 075 210, Jul. 2016.

[93] C. K. Walker, "THz Coherent Detection Systems," in *Terahertz Astronomy*, First Edit, 2015, ch. 6, pp. 159–227.

[94] M. I. Amanti, M. Fischer, G. Scalari, M. Beck, and J. Faist, "Low-divergence single-mode terahertz quantum cascade laser," *Nature Photonics*, vol. 3, no. 10, pp. 586–590, Sep. 2009.

[95] N. Yu, Q. J. Wang, M. A. Kats, J. A. Fan, S. P. Khanna, L. Li, A. G. Davies, E. H. Linfield, and F. Capasso, "Designer spoof surface plasmon structures collimate terahertz laser beams," *Nature Materials*, vol. 9, no. 9, pp. 730–735, Aug. 2010.

[96] J. A. Fan, M. A. Belkin, F. Capasso, S. Khanna, M. Lachab, A Giles Davies, E. H. Linfield, R Köhler, A Tredicucci, F Beltram, H. E. Beere, E. H. Linfield, A. G. Davies, D. A. Ritchie, R. C. Iotti, F Rossi, K Unterrainer, R Colombelli, C Gmachl, F Capasso, H. Y. Hwang, D. L. Sivco, and A. Y. Cho, "Surface emitting terahertz quantum cascade laser with a double-metal waveguide," *Optics Express*, vol. 14, no. 24, pp. 11 672–11 680, Nov. 2006.

[97] M. I. Amanti, M. Fischer, C. Walther, G. Scalari, and J. Faist, "Horn antennas for terahertz quantum cascade lasers," *Electronics Letters*, vol. 43, no. 10, pp. 573–574, 2007.

[98] A. W. M. Lee, B. S. Williams, J. L. Reno, Q. Qin, Q. Hu, and S. Kumar, "High-power and high-temperature THz quantum-cascade lasers based on lens-coupled metal-metal waveguides," *Optics Letters*, vol. 32, no. 19, pp. 2840–2842, Oct. 2007.

[99] M. C. Wanke, E. W. Young, C. D. Nordquist, M. J. Cich, A. D. Grine, C. T. Fuller, J. L. Reno, and M. Lee, "Monolithically integrated solid-state terahertz transceivers," *Nature Photonics*, vol. 4, no. 8, pp. 565–569, Jun. 2010.

[100] W. Miao, Z. Lou, G.-Y. Xu, J. Hu, S.-L. Li, W. Zhang, K.-M. Zhou, Q.-J. Yao, K. Zhang, W.-Y. Duan, S.-C. Shi, R. Colombelli, H. E. Beere, D. A. Ritchie,

G Gogidze, Y. P. Gusev, A. I. Elant, B. S. Karasik, A. D. Semenov, W Zhang, P Khosropanah, J. R. Gao, E. L. Kollberg, K. S. Yngvesson, T Bansal, and R Barends, "Demonstration of a fully integrated superconducting receiver with a 2.7 THz quantum cascade laser," *Optics Express*, vol. 23, no. 4, pp. 4453–4458, Feb. 2015.

[101] Constantine A. Balanis, "Horn Antennas," in *Antenna Theory: Analysis and Design*, 4th Edition, Hoboken, New Jersey: Wiley, Mar. 2016, ch. 13, pp. 719–778.

[102] A. Valavanis, Y. J. Han, N. Brewster, P. Dean, R. Dong, L. Bushnell, M. Oldfield, J. X. Zhu, L. H. Li, A. G. Davies, B. Ellison, and E. H. Linfield, "Mechanically robust waveguide-integration and beam shaping of terahertz quantum cascade lasers," *Electronics Letters*, vol. 51, no. 12, pp. 919–921, Jun. 2015.

[103] J. F. Johansson and N. D. Whyborn, "Diagonal horn as a sub-millimeter wave antenna," *Doktorsavhandlingar vid Chalmers Tekniska Hogskola*, vol. 40, no. 5, pp. 795–800, 2000.

[104] B. N. Ellison, A. Valavanis, O. Auriacombe, D. Gerber, T. Rawlings, N. Brewster, M. L. Oldfield, Y. Han, L. H. Li, E. Zafar, E. H. Linfield, A. G. Davies, G. Savini, M. Emes, B. Winter, D. Walker, and E. Saenz, "3.5 THz quantum-cascade laser emission from dual diagonal feedhorns," *International Journal of Microwave and Wireless Technologies*, vol. 11, no. 9, pp. 909–917, Nov. 2019.

[105] M. Wienold, L. Schrottke, M. Giehler, R. Hey, W. Anders, and H. T. Grahn, "Low-voltage terahertz quantum-cascade lasers based on LO-phonon-assisted interminiband transitions," *Electronics Letters*, vol. 45, no. 20, pp. 1030–1031, 2009.

[106] Y. J. Han, L. H. Li, A. Valavanis, N. Brewster, J. X. Zhu, R. Dong, P. Dean, L. Bushnell, M. Oldfield, A. G. Davies, B. Ellison, and E. H. Linfield, "Development of terahertz frequency quantum cascade lasers for the applications as local oscillators," in *THz for CBRN and Explosives Detection and Diagnosis*, M. Pereira and O Shulika, Eds., Springer Netherlands, 2017, pp. 123–134.

[107] A. Albo and Y. V. Flores, "Carrier Leakage Dynamics in Terahertz Quantum Cascade Lasers," *IEEE Journal of Quantum Electronics*, vol. 53, no. 5, pp. 1–8, 2017.

[108] L. Schrottke, M. Wienold, R. Sharma, X. Lü, K. Biermann, R. Hey, A. Tahraoui, H. Richter, H. W. Hübers, and H. T. Grahn, "Quantum-cascade lasers as local oscillators for heterodyne spectrometers in the spectral range around 4.745 THz," *Semiconductor Science and Technology*, vol. 28, no. 3, p. 035 011, Feb. 2013.

[109] "IEEE Standard for Rectangular Metallic Waveguides and Their Interfaces for Frequencies of 110 GHz and Above—Part 2: Waveguide Interfaces," *IEEE*, pp. 1–22, 2016.

[110] P. Harrison and A. Valavanis, *Quantum Wells, Wires and Dots*. John Wiley & Sons, Ltd, 2016, pp. 1–624.

[111] A. Valavanis, P. Dean, A. Scheuring, M. Salih, A. Stockhausen, S. Wuensch, K. Il'in, S. Chowdhury, S. P. Khanna, M. Siegel, A. G. Davies, and E. H. Linfield, "Transient analysis of substrate heating effects in a terahertz quantum cascade laser using an ultrafast NbN superconducting detector," *International Conference on Infrared, Millimeter, and Terahertz Waves, IRMMW-THz*, 2013.

[112] M. S. Vitiello, G. Scamarcio, and V. Spagnolo, "Time-resolved measurement of the local lattice temperature in terahertz quantum cascade lasers," *Applied Physics Letters*, vol. 92, no. 10, p. 101 116, Mar. 2008.

[113] I. Microtech instruments, *Free Standing Wire Grid Polarizers*, 2021.

[114] F. T. Ulaby, E Michielssen, and U Ravaioli, *Fundamentals of Applied Electromagnetics*, Seventh. Pearson Education Limited, 2015, p. 528.

[115] T. Taimre, M. Nikolic, K. Bertling, Y. Leng Lim, T. Bosch, and A. Rakic. D, "Laser feedback interferometry: a tutotial on the self-mixing effect for coherent sensing," *Advances in Optics and Phtonics*, vol. 7, no. 3, pp. 570–631, 2015.

[116] S. Donati, "Laser interferometry by induced modulation of cavity field," *Journal of Applied Physics*, vol. 49, no. 2, pp. 495–497, Feb. 1978.

[117] G. H. M. v. Tartwijk and D Lenstra, "Semiconductor lasers with optical injection and feedback," *Quantum and Semiclassical Optics: Journal of the European Optical Society Part B*, vol. 7, no. 2, pp. 87–143, Apr. 1995.

[118] J. H. Churnside, "Signal-to-noise in a backscatter-modulated Doppler velocimeter," *Applied Optics*, vol. 23, no. 13, p. 2097, Jul. 1984.

[119] N. Schunk and K. Petermann, "Numerical analysis of the feedback regimes for a single-mode semiconductor laser with external feedback," *IEEE Journal of Quantum Electronics*, vol. 24, no. 7, pp. 1242–1247, Jul. 1988.

[120] G. A. Acket, D. Lenstra, A. J. Boef, and B. H. Verbeek, "The Influence of Feedback Intensity on Longitudinal Mode Properties and Optical Noise in Index-Guided Semiconductor Lasers," *IEEE Journal of Quantum Electronics*, vol. 20, no. 10, pp. 1163–1169, 1984.

[121] D. Lenstra, B. H. Verbeek, and A. J. den Boef, "Coherence Collapse in Single-Mode Semiconductor Lasers Due to Optical Feedback," *IEEE Journal of Quantum Electronics*, vol. 21, no. 6, pp. 674–679, 1985.

[122] K. Petermann, "External Optical Feedback Phenomena in Semiconductor Lasers," *IEEE Journal on Selected Topics in Quantum Electronics*, vol. 1, no. 2, pp. 480–489, 1995.

[123] J. Helms, C. Kurtzke, and K. Petermann, "External feedback requirements for coherent optical communication systems," *Journal of Lightwave Technology*, vol. 10, no. 8, pp. 1137–1141, Aug. 1992.

[124] D. A. Kleinman and P. P. Kisliuk, "Discrimination Against Unwanted Orders in the Fabry-Perot Resonator," *Bell System Technical Journal*, vol. 41, no. 2, pp. 453–462, 1962.

[125] P. King and G. Steward, "Metrology with an optical maser," *New Science*, vol. 17, no. 180, 1963.

[126] C. B. Wheeler and S. J. Fielding, "Interferometry using a laser as radiation source, amplifier and detector," *Journal of Physics E: Scientific Instruments*, vol. 5, no. 1, pp. 101–103, Jan. 1972.

[127] J. W. Crowe and R. M. Craig, "GaAs laser linewdith measurements by heterodyne detection," *Applied Physics Letters*, vol. 5, no. 4, p. 72, Nov. 1964.

[128] A. Seko, Y. Mitsuhashi, T. Morikawa, J. Shimada, and K. Sakurai, "Self-quenching in semiconductor lasers and its applications in optical memory readout," *Applied Physics Letters*, vol. 27, no. 3, p. 140, Sep. 1975.

[129] K. Bertling, Y. L. Lim, T. Taimre, D. Indjin, P. Dean, R. Weih, S. Höfling, M. Kamp, M. Von Edlinger, J. Koeth, and A. D. Rakić, "Demonstration of the self-mixing effect in interband cascade lasers," *Applied Physics Letters*, vol. 103, no. 23, p. 231 107, Dec. 2013.

[130] A. Bruyant, B. Bérenguier, E. Lacot, G. Lérondel, I. Stéfanon, O. Hugon, O. Jacquin, P. Royer, and S. Blaize, "Phase sensitive optical near-field mapping using frequency-shifted laser optical feedback interferometry," *Optics Express*, vol. 16, no. 16, pp. 11 718–11 726, Aug. 2008.

[131] P. Nerin, P. Puget, P. Besesty, and G. Chattier, "Self-mixing using a dual-polarisation Nd:YAG microchip laser," *Electronics Letters*, vol. 33, no. 6, pp. 491–492, Mar. 1997.

[132] R. P. Green, J. H. Xu, L. Mahler, A. Tredicucci, F. Beltram, G. Giuliani, H. E. Beere, and D. A. Ritchie, "Linewidth enhancement factor of terahertz quantum cascade lasers," *Applied Physics Letters*, vol. 92, no. 7, p. 071 106, Feb. 2008.

[133] P. Dean, Y. Leng Lim, A. Valavanis, R. Kliese, M. Nikolić, S. P. Khanna, M. Lachab, D. Indjin, Z. Ikonić, P. Harrison, A. D. Rakić, E. H. Linfield, and A. G. Davies, "Terahertz imaging through self-mixing in a quantum cascade laser," *Optics Letters*, vol. 36, no. 13, p. 2587, Jul. 2011.

[134] Y. J. Han, J. Partington, R. Chhantyal-Pun, M. Henry, O. Auriacombe, T. Rawlings, L. H. Li, J. Keeley, M. Oldfield, N. Brewster, R. Dong, P. Dean, A. G. Davies, B. N. Ellison, E. H. Linfield, and A. Valavanis, "Gas spectroscopy through multimode self-mixing in a double-metal terahertz quantum cascade laser," *Optics Letters*, vol. 43, no. 24, p. 5933, Dec. 2018.

[135] M. J. Rudd, "A laser Doppler velocimeter employing the laser as a mixer-oscillator," *Journal of Physics E: Scientific Instruments*, vol. 1, no. 7, pp. 723–726, Jul. 1968.

[136] R. Chhantyal-Pun, A. Valavanis, J. T. Keeley, P. Rubino, I. Kundu, Y. Han, P. Dean, L. Li, A. G. Davies, and E. H. Linfield, "Gas spectroscopy with integrated frequency monitoring through self-mixing in a terahertz quantum-cascade laser," *Optics Letters*, vol. 43, no. 10, pp. 2225–2228, 2018.

[137] R. Lang and K. Kobayashi, "External Optical Feedback Effects on Semiconductor Injection Laser Properties," *IEEE Journal of Quantum Electronics*, vol. 16, no. 3, pp. 347–355, 1980.

[138] C. H. Henry, "Theory of the Linewidth of Semiconductor Lasers," *IEEE Journal of Quantum Electronics*, vol. 18, no. 2, pp. 259–264, 1982.

[139] K. Petermann, *Laser Diode Modulation and Noise*, First. Springer Netherlands, 1988, p. 315.

[140] G. Giuliani, M. Norgia, S. Donati, and T. Bosch, "Laser diode self-mixing technique for sensing applications," *Journal of Optics A: Pure and Applied Optics*, vol. 4, no. 6, Nov. 2002.

[141] Y. Yu, G. Giuliani, and S. Donati, "Measurement of the linewidth enhancement factor of semiconductor lasers based on the optical feedback self-mixing effect," *IEEE Photonics Technology Letters*, vol. 16, no. 4, pp. 990–992, Apr. 2004.

[142] A. Valavanis, P. Dean, Y. L. Lim, R. Alhathlool, M. Nikolic, R. Kliese, S. P. Khanna, D. Indjin, S. J. Wilson, A. D. Rakic, E. H. Linfield, and G. Davies, "Self-Mixing Interferometry With Terahertz Quantum Cascade Lasers," *IEEE Sensors Journal*, vol. 13, no. 1, pp. 37–43, Jan. 2013.

[143] Y. Leng Lim, P. Dean, M. Nikoli, R. Kliese, S. P. Khanna, M. Lachab, A. Valavanis, D. Indjin, Z. Ikoni, P. Harrison, E. H. Linfield, A. Giles Davies, S. J. Wilson, and A. D. Raki, "Demonstration of a self-mixing displacement sensor based on terahertz quantum cascade lasers," *Applied Physics Letters*, vol. 99, no. 8, p. 081 108, Aug. 2011.

[144] P. Dean, A. Valavanis, J. Keeley, K. Bertling, Y. Leng Lim, R. Alhathlool, S. Chowdhury, T. Taimre, L. H. Li, D. Indjin, S. J. Wilson, A. D. Rakić, E. H. Linfield, and A. Giles Davies, "Coherent three-dimensional terahertz

imaging through self-mixing in a quantum cascade laser," *Applied Physics Letters*, vol. 103, no. 18, p. 181 112, Oct. 2013.

[145] T. Hagelschuer, M. Wienold, H. Richter, L. Schrottke, K. Biermann, H. T. Grahn, and H. W. Hübers, "Terahertz gas spectroscopy through self-mixing in a quantum-cascade laser," *Applied Physics Letters*, vol. 109, no. 19, p. 191 101, Nov. 2016.

[146] J. Keeley, J. Freeman, K. Bertling, Y. Leng Lim, R. A. Mohandas, T. Taimre, L. H. Li, D. Indjin, A. D. Rakic, E. H. Linfield, A. G. Davies, and P. Dean, "Measurement of the emission spectrum of a semiconductor laser using laser-feedback interferometry," *Scientific Reports*, vol. 7, no. 1, pp. 1–9, 2017.

[147] L. Friedman and V. J. Shiner, "Experimental Determination of the Disproportionation of Hydrogen Isotopes in Water," *The Journal of Chemical Physics*, vol. 44, no. 12, pp. 4639–4640, Jun. 1966.

[148] T. Hagelschuer, M. Wienold, H. Richter, L. Schrottke, H. T. Grahn, H.-w. Hübers, P. C. Ashworth, E Pickwell-MacPherson, E Provenzano, S. E. Pinder, A. D. Purushotham, M Pepper, V. P. Wallace, A. G. Davies, A. D. Burnett, W Fan, E. H. Linfield, J. E. Cunningham, T. spectroscopy, R Güsten, H Wiesemeyer, H.-w. Hübers, C Jarchow, H Richter, B Klein, G Pavlov, A. D. Semenov, L Mahler, A Tredicucci, H. E. Beere, P Khanna, M Lachab, A Valavanis, D Indjin, Z Ikonić, P Harrison, S. J. Wilson, and A. D. Rakić, "Real-time gas sensing based on optical feedback in a terahertz quantum-cascade laser," *Optics Express*, vol. 25, no. 24, pp. 30 203–30 213, 2017.

[149] A. A. Michelson, "ART. XXI. The relative motion of the Earth and the Luminiferous ether," *American Journal of Science*, vol. 22, no. 128, p. 120, 1881.

[150] D. Malacara, "Twyman–Green Interferometer," in *Optical Shop Testing*, D. Malacara, Ed., Third Edit, John Wiley & Sons, Ltd, Nov. 2006, ch. 2, pp. 46–96.

[151] L. Mach, "Ueber einen interferenzrefraktor," *Zeitschrift fur Instrumentenkunde*, vol. 12, no. 3, p. 89, 1892.

[152] C Fabry and A Perot, "Theorie et applications d'une nouvelle methode de spectroscopie interferentielle," *Annales de chimie et de physique*, vol. 16, no. 7, 1899.

[153] A. A. Michelson and E. W. Morley, "On the relative motion of the Earth and the luminiferous ether," *American Journal of Science*, vol. s3-34, no. 203, pp. 333–345, Nov. 1887.

[154] A. A. Michelson and F. G. Pease, "Measurement of the Diameter of Alpha-Orionis by the Interferometer," *Proceedings of the National Academy of Sciences*, vol. 7, no. 5, pp. 143–146, May 1921.

[155] A. Labeyrie, "Interference fringes obtained on Vega with two optical telescopes.," *Astrophysical Journal*, vol. 196, pp. L71–L75, Mar. 1975.

[156] P. Minnett, R. Knuteson, F. Best, B. Osborne, J. Hanafin, and O. Brown, "The Marine-Atmospheric Emitted Radiance Interferometer: A High-Accuracy, Seagoing Infrared Spectroradiometer," *Journal of Atmospheric and Oceanic Technology*, vol. 18, no. 6, pp. 994–1013, 2001.

[157] L. Fu, D. Alsdorf, E. Rodriguez, R. Morrow, N. Mognard, J. Lambin, P. Vaze, and T. Lafon, "The SWOT (Surface Water and Ocean Topography) mission: Spaceborne radar interferometry for oceanographic and hydrological applications," in *OCEANOBS 9*, 2009, pp. 21–25.

[158] K. Pandey, "A study of chemical structure of soft and hardwood and wood polymers by FTIR spectroscopy," *Journal of Applied Polymer Science*, vol. 71, no. 12, pp. 1969–1975, 1999.

[159] Z. Movasaghi, S. Rehman, and I. U. Rehman, "Fourier Transform Infrared (FTIR) Spectroscopy of Biological Tissues," *Applied Spectroscopy Reviews*, vol. 43, no. 2, pp. 134–179, 2008.

[160] A. P. Thorne, J. W. Brault, and R. C. M. Learner, "Ghosts and artifacts in Fourier-transform spectrometry," *Applied Optics*, vol. 35, no. 16, pp. 2947–2954, Jun. 1996.

[161] E. Nuttall, Y. J. Han, D. Pardo, M. D. Horbury, S. S. Kondawar, N. K. North, I. Kundu, O. Auriacombe, T. Rawlings, N. Brewster, M. Oldfield, M. Salih, L. H. Li, E. Zafar, A. G. Davies, E. H. Linfield, E. Saenz, H. Wang, B. N. Ellison, and A. Valavanis, "Waveguide integrated terahertz quantum-cascade laser systems," *International Conference on Infrared, Millimeter, and Terahertz Waves, IRMMW-THz*, vol. 2021, 2021.

[162] M. Kocybik, A. Krysl, N. Vieweg, A. Lisauskas, H. G. Roskos, M. Bauer, and F. Friederich, "Resonant Terahertz Field-effect Transistors for Spectroscopic Sensing Applications," *International Conference on Infrared, Millimeter, and Terahertz Waves, IRMMW-THz*, vol. 2022, 2022.

[163] W. Jitschin, "Locking the laser frequency to an atomic transition," *Applied Physics B Photophysics and Laser Chemistry*, vol. 33, no. 1, pp. 7–8, Jan. 1984.

[164] K. M. Yocum, S. N. Milam, P. A. Gerakines, and S. L. Widicus Weaver, "Sublimation of Laboratory Ices Millimeter/Submillimeter Experiment (SubLIME): Structure-specific Identifications of Products from UV-photolyzed Methanol Ice," *The Astrophysical Journal*, vol. 913, no. 1, p. 61, May 2021.